

DISSERTATION ZUR ERLANGUNG DES DOKTORGRADES
DER FAKULTÄT FÜR CHEMIE UND PHARMAZIE
DER LUDWIG-MAXIMILIANS-UNIVERSITÄT MÜNCHEN

The modulation of actin dynamics by the stress-induced protein DRR1 and antidepressants

Anja Kretzschmar

aus Heidenheim an der Brenz



2015

DISSERTATION ZUR ERLANGUNG DES DOKTORGRADES
DER FAKULTÄT FÜR CHEMIE UND PHARMAZIE
DER LUDWIG-MAXIMILIANS-UNIVERSITÄT MÜNCHEN

The modulation of actin dynamics by the stress-induced protein DRR1 and antidepressants

Anja Kretzschmar

aus Heidenheim an der Brenz



2015

Erklärung

Diese Dissertation wurde im Sinne von §7 der Promotionsordnung vom 28. November 2011 von Herrn Prof. Dr. Haralabos Zorbas betreut.

Eidesstattliche Versicherung

Diese Dissertation wurde eigenständig und ohne unerlaubte Hilfe erarbeitet.

München, den 19.02.2015

Anja Kretzschmar

Dissertation eingereicht am: 23.02.2015

Erstgutachter: Prof. Dr. rer. nat. Haralabos Zorbas

Zweitgutachter: Prof. Dr. med. Dr. rer. nat. Dr. h.c. Florian Holsboer

Tag der mündlichen Prüfung: 18.06.2015

Para mi abuelo y mis padres

For my grandfather and my parents

Summary

Actin dynamics are involved in a plethora of vital cellular processes, including cell division and motility, regulation of cell shape or endocytic trafficking, among others. At the synapse, actin is the most prominent cytoskeletal component, and hence a major player impacting on synaptic transmission by regulating synaptic shape, neurotransmitter vesicle release and post-synaptic receptor trafficking.

Growing evidence suggests that the pathogenesis of depression involves structural neuronal changes and that the therapeutic benefit of antidepressants might be mediated by affecting neuronal plasticity. Moreover, the “disturbed cytoskeletal theory” of mood disorders has been proposed, and chronic stress is known to affect neuronal structure and synaptic transmission efficiency. While it is clear that these processes of adaptation and maladaptation to stress are brought about by alterations of actin structures, up to now, a profound mechanistic understanding of the pathway from stress to neuronal reorganization and cognitive performance remains elusive.

As a contribution to elucidating the relevance of actin dynamics for synaptic function during the stress response, a two-sided approach was taken in this study by analyzing the actin-related effects of the stress-induced protein DRR1 (Down-regulated in renal cell carcinoma 1) and of antidepressants, respectively.

The three antidepressants clomipramine, doxepin, and citalopram were tested in several *in vitro* assays of actin dynamics. Only clomipramine moderately slowed down overall actin polymerization; this was attributed to a potential reduction of the nucleation process required for the formation of actin filaments. High excess of clomipramine over actin was necessary in these experiments to produce the effect. In cells, the overall F-actin structure and two-dimensional migration remained unaffected by treatment with clomipramine, while spreading appeared to be reduced at high concentrations of clomipramine. However, unspecific cytotoxic effects of clomipramine at this concentration might be involved, as observed in cellular stainings with high concentrations.

Being previously known as potential tumor suppressor, DRR1 was recently characterized as a direct link between chronic stress, actin dynamics and improved cognition (Schmidt et al., 2011). In addition to the previously described actin bundling activity of DRR1, here, it was found to cap actin filaments, thereby inhibiting their elongation with a concomitant increase in nucleation of new filaments. This tripartite effect of DRR1 is accomplished by two actin binding regions separated by a central domain, which is presumably mediating homodimerization. Altogether, DRR1 shifts the actin filament structure towards more, shorter, and thicker actin bundles.

DRR1 was furthermore found to increase the overall F-actin content in HeLa cells, resulting in the activation of the transcription factor serum response factor, which is dependent on the G-/F-actin equilibrium in the cell. Spreading of HeLa cells was inhibited by DRR1's bundling and capping activities, and bundling appeared to reduce actin turnover in cells. In primary hippocampal neurons, ectopic DRR1 was located along dendrites with a strong accumulation in dendritic spines and particularly in enlarged spine heads.

The findings in this work support the notion of DRR1 as an intriguingly multifunctional player in organizing the actin cytoskeleton at the synapse during stress response. Previous behavioral analysis of DRR1 proposed a function in promoting stress resilience, due to the improved cognition and sociability upon virus-mediated upregulation of DRR1 in the hippocampus and lateral septum, respectively (Masana et al., 2014; Schmidt et al., 2011). The results obtained in this study further reinforce this role in stress coping, as the molecular effect of DRR1 on actin dynamics is in line with a function in stabilizing mature dendritic spines, which are characterized by a branched, crosslinked and capped actin meshwork.

Assuming that the effect of DRR1 on actin dynamics is not only significant for coping with chronic stress but also during tumor development and progression, the model of DRR1's molecular mechanism presented in this work could contribute to several physiologically relevant processes. Altogether, this study adds to a more comprehensive understanding of actin dynamics in response to chronic stress and upon treatment with antidepressants. Eventually, this knowledge has the potential to open up novel therapeutic targets for psychiatric disorders.

Contents

Summary	IV
1. Introduction	1
1.1. Physiological and pathological mechanisms of stress	1
1.1.1. The HPA axis	1
1.1.2. Effects of stress on neurons and the brain	2
1.1.3. Stress as a risk factor for psychiatric disorders	3
1.2. Actin dynamics and actin binding proteins	4
1.2.1. Actin polymerization	4
1.2.2. Regulation of actin structures and dynamics	4
1.3. Actin-dependent processes in cells	7
1.3.1. Basic cellular functions of actin dynamics	7
1.3.2. Effects of nuclear actin	8
1.3.3. Signal transduction of actin dynamics	9
1.3.4. Synaptic plasticity, learning and memory	11
1.4. Effects of antidepressants on cytoskeletal dynamics	12
1.5. The stress-induced protein DRR1	13
1.5.1. Identification of a novel, stress-induced protein	13
1.5.2. Interaction partners of DRR1	15
1.5.3. Cellular effects of DRR1	16
1.5.4. Effects of DRR1 on neuronal cells	16
1.5.5. DRR1 shapes cognition and social behavior	17
1.6. Objective	17
2. Material	18
2.1. Consumable supplies	18
2.2. Chemicals	19
2.3. Solutions and media	21
2.4. Kits and ready-to-use materials	21

2.5.	Enzymes	22
2.5.1.	Restriction endonucleases	22
2.5.2.	DNA polymerases and ligases	22
2.6.	Antibodies	22
2.6.1.	Primary antibodies	22
2.6.2.	Secondary antibodies	23
2.7.	Bacterial clades	23
2.8.	Cell lines	23
2.9.	Oligonucleotides	24
2.10.	Plasmids	25
2.11.	Instruments	27
2.12.	Software	29
3.	Methods	30
3.1.	Bacterial culture	30
3.1.1.	Culturing bacteria	30
3.1.2.	Preparation of competent cells	30
3.1.3.	Transformation	31
3.1.4.	Isolation of DNA from bacteria (Mini/Midi/Maxi)	31
3.2.	Cloning	32
3.2.1.	Polymerase chain reaction (PCR)	32
3.2.2.	Site-directed mutagenesis	34
3.2.3.	Agarose gel electrophoresis	34
3.2.4.	Purification of DNA from agarose gels	35
3.2.5.	Restriction of DNA	35
3.2.6.	Ligation of DNA	35
3.2.7.	Subcloning	35
3.2.8.	Measurement of DNA concentration	35
3.2.9.	Sequencing	36
3.3.	Cell culture	36
3.3.1.	Culturing of eukaryotic cell lines	36
3.3.2.	Storage of cell lines	36
3.3.3.	Coating of glass coverslips/dishes and cell seeding	37
3.3.4.	Transfection by electroporation	37
3.3.5.	Transfection with TurboFect	38
3.3.6.	Transfection with Lipofectamine 2000	38
3.4.	Primary hippocampal culture	38
3.4.1.	Preparation of primary mice hippocampal neurons	38
3.4.2.	Culturing of hippocampal neurons	39
3.4.3.	Transfection with the calciumphosphate method	39

3.5.	Proteinbiochemical methods.....	40
3.5.1.	SDS-Polyacrylamide gel electrophoresis	40
3.5.2.	Colloidal Coomassie staining of PAA gels.....	41
3.5.3.	Western Blot	41
3.5.4.	Measurement of protein concentration	42
3.5.5.	Recombinant protein expression and purification	43
3.5.6.	Determination of protein concentration	44
3.6.	Cellular assays.....	44
3.6.1.	Dual-luciferase reporter gene assay	44
3.6.2.	Co-immunoprecipitation with GFP-Trap.....	45
3.6.3.	Chemical crosslinking	46
3.6.4.	Cell spreading.....	47
3.6.5.	Cellular fractionation.....	47
3.6.6.	2D-Migration assay.....	48
3.6.7.	Fluorescence recovery after photobleaching (FRAP)	48
3.7.	Cellular stainings.....	49
3.7.1.	Fixation, Permeabilization and blocking of cells	49
3.7.2.	Immunostaining.....	49
3.7.3.	F-actin staining with phalloidin	49
3.7.4.	DAPI staining of nuclei	50
3.7.5.	Storage of stained cells	50
3.7.6.	Colocalization analysis.....	50
3.7.7.	Quantification of mean cellular F-actin content.....	50
3.8.	<i>In vitro</i> actin assays	51
3.8.1.	Preparation of purified G-actin from tissue	51
3.8.2.	Pyrene-actin polymerization.....	51
3.8.3.	Actin-filament elongation and nucleation assay	52
3.8.4.	Actin networks	53
3.8.5.	Rheology	53
3.8.6.	F-Actin co-sedimentation	54
3.9.	Statistical analysis.....	54
4.	Results	55
4.1.	Clomipramine impacts on actin dynamics	55
4.1.1.	Clomipramine slows down actin polymerization	55
4.1.2.	Actin networks are not affected by antidepressants.....	61
4.1.3.	Actin-dependent effects of antidepressants in cells	62
4.2.	The stress-induced protein DRR1	66
4.2.1.	DRR1 has a tripartite effect on <i>in vitro</i> actin-dynamics.....	66
4.2.2.	The functions of DRR1 are executed by two actin-binding regions and a dimerization domain.....	73
4.2.3.	DRR1 localizes to both the cytosol and the nucleus	83
4.2.4.	DRR1 binds and increases F-actin in cells	84
4.2.5.	DRR1 modulates actin-dependent processes in cells	94
4.2.6.	DRR1 is located at post-synaptic spines	97

5. Discussion	98
5.1. Antidepressants effect on actin dynamics	98
5.2. Molecular effect of DRR1 on actin dynamics.....	99
5.3. Cellular effects of DRR1	103
5.4. Effects of DRR1 on synaptic plasticity	106
5.5. The function of DRR1 during stress response.....	108
5.6. Outlook.....	109
References	110
Appendix.....	126
Supplementary Movies	126
Supplementary Figure	127
Abbreviations	128
List of Figures	130
List of Tables.....	131
Biographical Sketch.....	132
Publications.....	133
Acknowledgements	134

1. Introduction

1.1. Physiological and pathological mechanisms of stress

All organisms face a constant exposure to changing environmental stimuli, while thriving towards stable physiological conditions. Therefore, in response to a challenging stressor, an adaptive response is initiated in order to return to a physiological equilibrium. The impact of stressors depends on their intensity and duration as well as on the vulnerability of individuals. In spite of these variations, a common response pattern with characteristic alterations in the behavioral, autonomic and neuroendocrine systems exists (Pacák and Palkovits, 2001). While the physiological stress response is an important process to maintain homeostasis, long-term exposure or trauma can lead to maladaptation and pathological consequences like anxiety, depression, schizophrenia or post-traumatic stress disorder (de Kloet et al., 2005).

1.1.1. The HPA axis

The hypothalamic-pituitary-adrenal (HPA) axis was described for the first time by the Canadian endocrinologist Hans Selye as the key effector of the stress response (Selye, 1936, 1950). In addition to the immediate “fight-or-flight” response to a stressor via the autonomic nervous system, the HPA axis provides a slower neuroendocrine system facilitating adaptation, while also evoking rapid effects similar to the autonomic system (Ulrich-Lai and Herman, 2009).

The synthesis and secretion of glucocorticoids as the effector hormone of the HPA axis involves a complex neuroendocrine cascade. Sensory information induced by an external or internal stressor is processed in the limbic structures of the brain, including the amygdala, hippocampus and prefrontal cortex. The secretion of corticotropin-releasing hormone (CRH) and vasopressin (AVP) from the hypothalamus governs HPA axis activity

stimulating production and secretion of adreno-corticotrophic hormone (ACTH) from the anterior pituitary gland. ACTH in turn activates secretion of glucocorticoids from the adrenal glands (Engelmann et al., 2004). In order to reinstate a homeostatic equilibrium, glucocorticoids inhibit the synthesis and release of CRH and ACTH, thus forming a negative-feedback loop balancing HPA axis activity (De Kloet and Reul, 1987).

The effects of glucocorticoids – mainly cortisol in humans and corticosterone in rodents – are executed by two intracellular receptors, the glucocorticoid receptor (GR) and the mineralocorticoid receptor (MR). While the GR is restricted to neurons of the limbic system, the MR is widely expressed throughout neurons and glia in the whole brain and exhibits an about 10fold higher affinity to glucocorticoids than the GR (Reul and de Kloet, 1985). The MR is thus activated at low levels of stress mediating basal HPA activity. In contrast, the GR shows activity during high and prolonged glucocorticoid levels and is progressively activated during stress- and circadian-induced boosts (de Kloet et al., 1993). Being transcriptional regulators, the MR and the GR impact on numerous genes, and only roughly one third of the target genes respond to both receptors (Datson et al., 2001). Immediate effects of glucocorticoids implicate energy mobilization by affecting cell metabolism and increased arousal and excitability, while slower, gene-mediated effects involve suppression of immune function, and changes in synaptic transmission (de Kloet et al., 2005).

1.1.2. Effects of stress on neurons and the brain

The pathological effects of stress on brain structure and function have been acknowledged for more than 30 years, after chronic exposure to high levels of glucocorticoids was shown to reduce hippocampal volume and impair cognitive function (Landfield et al., 1981).

Acute and chronic stress have been shown to evoke dramatic changes in the amygdala, prefrontal cortex and the hippocampus (Lupien et al., 2009; Roozendaal et al., 2009; Vyas et al., 2002). In addition, changes in neuronal architecture and network dynamics have been observed including a reduction of adult neurogenesis, remodeling of dendritic spines and a reduction in synapse number in CA3 hippocampal neurons (Fuchs et al., 2006). While imaging studies have provided evidence for a reduction in hippocampal volume of patients with depression, the exact mechanisms of this (reversible) volume loss remain unclear. Neither neuronal loss nor suppression of neurogenesis appear to be decisive, but a decrease in dendritic arborization, amount of synapses, and loss of glial cells were proposed as cause (Czeh and Lucassen, 2007). A reduction in dendritic spine number was shown both upon stress and during depression, supporting the causal role of chronic stress in the etiology of affective diseases (Chen et al., 2008; Soetanto et al., 2010).

Moreover, structural changes of neurons in response to stress impact on learning and memory formation. In particular, dynamics of dendritic spines have been shown to be implicated in these processes (Kasai et al., 2010). Acute and mild stress has been shown to facilitate memory formation. In contrast, chronic stress exposure or high levels of glucocorticoids can severely impair cognitive performance (Reagan et al., 2008). The molecular underpinnings linking stress to cognition are just beginning to be understood. For example, chronic social defeat stress caused a sustained reduction in the levels of the Rho-GTPase Rac1 in the nucleus accumbens (a part of the limbic system) via epigenetic repression of the promotor, which resulted in depressive like behavior of mice. Since Rac1 is implicated in spine formation by impacting on actin dynamics, these findings indicate a tight regulatory network from stress, to the actin cytoskeleton and behavior (Golden et al., 2013).

Although vast evidence supports the mechanisms of adaptation and maladaptation to stress on the structural and behavioral level, molecular players translating such stressful stimuli into changes in synaptic transmission and behavior remain largely unknown.

1.1.3. Stress as a risk factor for psychiatric disorders

In the beginning of the 20th century, the German psychiatrist Emil Kraepelin was the first to classify affective disorders thereby initiating the modern era of scientific psychiatry. Although up to now the etiology of affective disorders including major depression, PTSD, anxiety, and bipolar disorder, is not fully understood, a causative role of high and prolonged stress has become obvious, particularly in individuals with a history of childhood adversity (McLaughlin et al., 2010). Today, strong evidence from correlative pre-clinical and clinical studies, genetically modified animals, and pharmacological studies analyzing HPA function in affective disorders supports the concept of stress as a risk factor for psychiatric disorders in genetically predisposed individuals (Ising and Holsboer, 2006; de Kloet et al., 2005).

Malfunctions of the HPA axis during affective disorders have been acknowledged since the late 60s after the observation of increased levels of cortisol in patients suffering from severe depression (Butler and Besser, 1968). Years later, HPA hyperactivity caused by an aberrant negative-feedback loop of the GR and increased CRH activity were found as a pathological mechanism underlying depression (Holsboer, 2000; Parker et al., 2003; Steckler et al., 1999). In contrast, PTSD patients were characterized by reduced blood cortisol levels (Yehuda, 2002).

Furthermore, genetic polymorphisms causing stress vulnerability have been identified, like an allele of the gene FKBP5, which correlated with increased recurrence of depressive episodes (Binder et al., 2004). This vulnerability was later associated with allele-specific

DNA demethylation in the functional GREs of the FKBP5 promotor, occurring upon childhood trauma and programming promotor reactivity to stress later in life (Klengel et al., 2013). Further evidence exists showing that pathological alterations in HPA axis activity are often induced by early life stress and, particularly, by epigenetic programming in response to environmental stressors (Halligan et al., 2007; Lupien et al., 2009; Weaver et al., 2004).

1.2. Actin dynamics and actin binding proteins

Actin, a 42 kDa big globular protein, is the major cytoskeletal and structural component at the synapse. Thus, it has to be rearranged to bring about the structural and functional alterations induced by stress surveyed above. In the following, the mechanisms of actin rearrangement are briefly reviewed.

1.2.1. Actin polymerization

Actin is the smallest fiber of the cellular cytoskeleton, which is composed of intermediate filaments, microtubules, and actin microfilaments. It is involved in a high variety of cellular functions including scaffolding, motility, cell division, and intracellular trafficking. This versatility is facilitated by its highly dynamic structure.

Actin exists in two states: monomeric, globular (G-)actin and polymeric, filamentous (F-)actin. It is an ATPase that tightly binds ATP together with a divalent cation (Mg^{2+} or Ca^{2+}). Under appropriate conditions, spontaneous assembly of actin filaments occurs in two phases. The first, energetically unfavorable step consists in the association of three ATP-bound actin subunits, a process termed nucleation. In the second step, the filament is rapidly elongated by the incorporation of additional actin monomers. Along the filament, the bound ATP is hydrolyzed to ADP, eventually causing the dissociation of monomers at the opposite end. In this way, the filament length eventually reaches a stable equilibrium of elongation and degradation (Pollard, 1986). Thus, actin filaments undergo a constant turnover of filaments referred to as treadmilling, in which new monomers are added at the barbed or “+” end, and depolymerization happens at the opposite pointed or “-“ end (Harris and Higgs, 2006).

1.2.2. Regulation of actin structures and dynamics

A plethora of actin binding proteins (ABPs) is involved in the regulation of actin polymerization dynamics and higher-order actin structures (Figure 1). Proteins influencing

on actin turnover can affect nucleation of G-actin or, by binding to the monomers or filament ends promote or prevent assembly and disassembly of F-actin (Figure 1A).

Nucleation of actin can be initiated either *de novo* by association of monomers into dimers and trimers, or by branching from preexisting filaments. The most widely studied class of *de novo* actin nucleators are the formins, including the diaphanous-related formins mDia (Dominguez, 2010). In the resting state, formins are autoinhibited by the interaction between their diaphanous autoregulatory domain (DAD) and the N-terminal diaphanous inhibitory domain (DID). Upon activation by Rho GTPases, this autoinhibition is released, and the formin-homology (FH) domains within the central region are enabled to promote *de novo* nucleation and filament elongation, by remaining bound to the barbed end (Pruyne et al., 2002). In contrast, the Arp2/3 complex generates new actin filaments by nucleation from existing filaments, thus creating new and free barbed ends for elongation (Mullins et al., 1998).

Elongation is terminated by capping proteins that bind to the barbed ends and inhibit the addition of further actin monomers, thereby limiting the length of the filament. In this way, they are essential for the regulation of actin turnover (Edwards et al., 2014).

Disassembly and shortening of older filaments, processes called severing, are performed by ADF/cofilin, the most prominent severing protein (Bernstein and Bamburg, 2010). Cofilin enhances actin filament turnover by inducing depolymerization and creating new barbed ends by releasing actin oligomers (Carlier et al., 1997; Lappalainen and Drubin, 1997).

At physiological concentration of Mg^{2+} within the cell in the millimolar range and at favorable pH conditions, ATP-actin should spontaneously associate to filaments leaving only a small fraction of monomers. Thus, the question arises how the high amount of unpolymerized actin is maintained in the cell. This effect can be attributed to another class of ABPs, the sequestering proteins. Such a sequestering protein, profilin, binds G-actin and inhibits nucleation. In addition, it promotes the nucleotide exchange of ADP-actin to ATP, thereby recycling old actin. Yet, profilin-actin monomers can associate to the barbed end, meaning that elongation is not inhibited by profilin (Pollard and Cooper, 1984).

Actin filaments can be arranged into higher-order structures like branched meshworks or thick actin bundles. Regulation of these structures is crucial for cell morphology and many cellular processes.

Sheet-like membrane protrusions at the leading edge of motile cells are composed of Arp2/3-branched actin meshworks (Figure 1B). Upon activation by the Wiskott-Aldrich syndrome protein (WASP), Arp2/3 nucleates new filaments by creating branches from existing ones at a fixed 70° angle, thus generating the lamellar structure (Higgs et al., 1999; Mullins et al., 1998). Furthermore, crosslinking proteins like filamin can stabilize

such an orthogonal meshwork structure by binding to two filaments (Figure 1C) (Nakamura et al., 2011).

Other crosslinking proteins create tight actin bundles which for example produce finger-like protrusions in the cell (Figure 1D). Due to the polarity of actin filaments, bundles can be either parallel or antiparallel, a parameter which is controlled by the respective bundling factor. For example, α -actinin generates both, parallel and anti-parallel actin bundles, while fascin generates a parallel organization (Jayo and Parsons, 2010; Sjöblom et al., 2008). Crosslinking proteins either feature two actin binding sites or one actin binding site and a dimerization region, thereby crosslinking filaments as monomers or dimers, respectively.

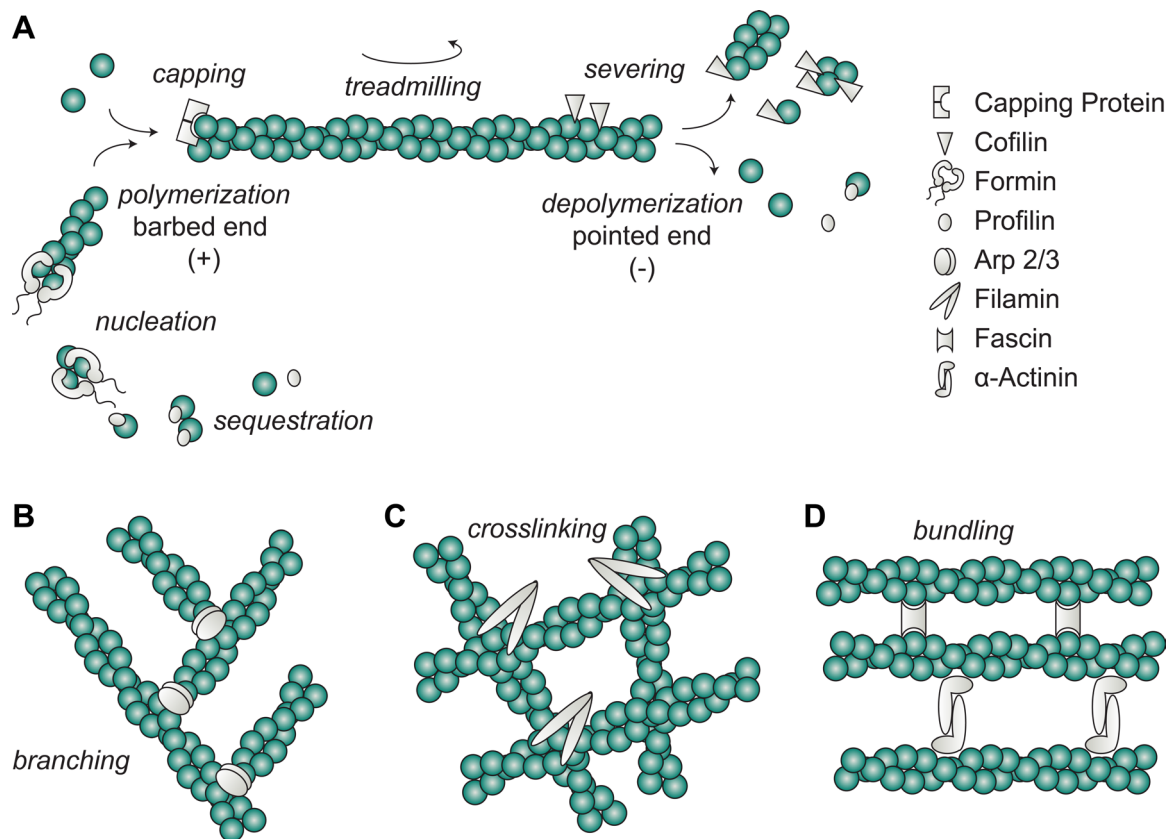


Figure 1. Overview of actin dynamics and actin binding proteins. (A) Actin filaments are polymerized at the barbed (+) end and depolymerized at the pointed (-) end, thereby undergoing a constant turnover (treadmilling). This basic polymerization kinetic is regulated by a variety of ABPs. Profilin helps to keep a pool of unpolymerized actin within the cell by sequestering G-actin, formins promote nucleation, capping proteins inhibit elongation at the barbed end, and severing proteins depolymerize and shorten the filaments. (B) A branched network of F-actin is created by the Arp2/3 complex by nucleation from preexisting filaments. (C) Orthogonal crosslinking of F-actin generates a meshwork structure (e.g. with filamin). (D) Bundling of actin filaments is performed by crosslinkers exhibiting either two actin-binding sites (e.g. fascin) or one actin-binding site concomitant with dimerization (e.g. α -actinin).

1.3. Actin-dependent processes in cells

1.3.1. Basic cellular functions of actin dynamics

Many basic cellular processes depend on proper regulation of actin dynamics. These include, among others, cell adhesion, morphogenesis, endo-/exocytosis, motility and cytokinesis.

Directional motility is a fundamental process for all organisms, for example during development, wound healing, or immune response; but is also used by cancer cells to invade neighboring tissue. While microtubules play an important role for cell polarization, it is commonly accepted that actin is the driver of cell locomotion (Euteneuer and Schliwa, 1984; Pletjushkina et al., 1994). Cell migration relies on three basic actin structures: a branched filamentous network termed lamellipodia comprising the sheet-structure of the leading edge, finger-like filopodial bundles at the plasma membrane, and contractile stress fibers in the cytoplasm (Pollard and Borisy, 2003). Actin bundles in filopodia are parallel-oriented, while stress fibers contain antiparallel actin fibers bundled with myosin (Cramer et al., 1997). Actin polymerization drives forward the leading edge of motile cells, and rapid depolymerization is necessary at the rear part of the cell to enable retraction and locomotion (Rohatgi et al., 1999; Zigmond, 1993). Lamellipodia at the leading edge consist of a highly structured meshwork of short actin filaments with the rapidly growing ends pointed towards the membrane. The filaments are branched by Arp2/3, are highly crosslinked, and reach a density of above $1000 \mu\text{m F-actin}/\mu\text{m}^3$ with a G-actin concentration of about $8.5 \mu\text{M}$ (Abraham et al., 1999). In contrast, filopodial protrusions are promoted by barbed-end nucleators like formins (Dominguez, 2010). Thus, the shape of the protrusion – lamellar or filopodial – is controlled by the balance of capping proteins and nucleators (Mejillano et al., 2004).

Furthermore, coordination of these actin-dependent processes with cycles of adhesion at the front and destabilization of adhesion at the rear via formation and disassembly of focal adhesions is essential for cell movement (Mitchison and Cramer, 1996). The focal adhesions in turn, are anchored to stress fibers and thereby mechanically interlinked with the actin machinery (Patla et al., 2010).

Tumor cells were shown to use the same basic strategies as non-neoplastic cells for metastatic migration (Friedl and Wolf, 2003). Meanwhile, a role for actin-bundling proteins has been described in cancer metastasis (Stevenson et al., 2012). Mechanical stiffness of the cell was inversely correlated with migratory and invasive potential of tumor cells, although this does not seem to be a general rule (Narumiya et al., 2009; Swaminathan et al., 2011).

Interestingly, nuclear shape was shown to be linked to cell shape and cell adhesion via an “actin-cap” on top of the nucleus, comprised of actin-myosin bundles. Defects in this actin cap were associated with diseases like progeria (accelerated aging), in which the nuclear shape is distorted (Khatau et al., 2009).

During cell division, extensive rearrangements of the actin and microtubule cytoskeleton take place. Upon entering mitosis, cells acquire their characteristic round shape. The separation of the centrosomes and subsequent spindle assembly is coordinated by actin and myosin (Uzbekov et al., 2002). At the end of mitosis, actin forms a contractile ring with myosin at the cleavage furrows to direct cytokinesis (Lee et al., 2012; Mabuchi, 1994). The importance of actin for cell cycle progression became obvious from studies using drugs impacting on actin polymerization or by overexpression of ABPs. For example, overexpression of the depolymerizing ADF/cofilin resulted in cell cycle arrest in G1 for more than 90% of the cells (Lee and Keng, 2005). An excess of F-actin induced by treatment with the drug Jasplakinolide, which stabilizes filaments, or overexpression of the WASP protein resulting in excessive Arp2/3 activation, generated polynucleated cells, suggesting defects in mitosis and cytokinesis (Moulding et al., 2007).

In neuronal cells, several fundamental aspects are regulated by actin dynamics, including proliferation, migration, axonal vesicle trafficking, and synaptic transmission. While the majority of migratory events take place during embryonic development, there is still migration in the postnatal and even in the mature, adult brain (Ghashghaei et al., 2007). The significance of actin in neuronal migration becomes evident by the association of mutations in the cytoplasmic β - and γ -actin genes with a neuronal defect causing structural brain abnormalities (Rivière et al., 2012). In mature neurons, actin is the most prominent cytoskeletal component at the synapse. Its functional significance goes beyond merely regulating the morphology of the synapse. The efficacy of synaptic transmission is modulated in a use-dependent manner and is believed to be the basis of learning and memory (Neves et al., 2008). Actin is a key regulator in both, pre- and post-synaptic mechanisms impacting on synaptic transmission (Dillon and Goda, 2005).

1.3.2. Effects of nuclear actin

Although during the last decade increasing evidence supports not only the presence, but also the crucial role of actin in the nucleus, its exact functional implications are still enigmatic. To begin with, controversial findings argue that nuclear actin is exclusively monomeric, or exists as filamentous F-actin stretches as well (McDonald et al., 2006; Pederson, 2008; Vartiainen et al., 2007). Suggested functions of actin-including complexes in the nucleus range from chromatin-remodeling during DNA replication and repair, to transcriptional regulation and to structural scaffolding (Castano et al., 2010).

DNA transcription was shown to be induced by association of Arp2/3 with RNA polymerase II. In a manner similar to its cytoplasmic function, Arp2/3 promotes actin assembly upon activation by N-WASP, resulting in increased RNA polymerase II-dependent transcription (Yoo et al., 2007). In fact, RNA pol II-dependent transcription was proposed to be regulated by a general actin-based mechanism during the initial phase, mediated by interactions with ribonucleoproteins (Kukalev et al., 2005; Percipalle et al., 2003).

Many nuclear hormone receptors are activated or repressed by ABPs. For example, the actin bundling protein supervillin acts as the primary coactivator of the androgen receptor (Ting et al., 2002). Furthermore, ADF/cofilin was found to inhibit the glucocorticoid receptor presumably via its actin severing and depolymerization activity (Rüegg et al., 2004).

1.3.3. Signal transduction of actin dynamics

Reorganization of the actin cytoskeleton is tightly regulated by complex signaling pathways in order to accomplish the high variety of cellular functions. Members of the Ras superfamily of small GTPases, in particular RhoA, Cdc42, and Rac1, have emerged as key players in linking surface receptors to the actin cytoskeleton. They function as molecular relay in response to extracellular signals by cycling between their inactive GDP-bound state and active GTP-bound state (Hall, 1998).

Constitutively active and dominant-negative mutants of the Rho GTPases have shed light on their effects. RhoA leads to the assembly of stress fibers (i.e. contractile actin-myosin filaments) and focal adhesions. While both Rac1 and Cdc42 promote actin polymerization, Rac1 leads to the formation of an F-actin meshwork at the cellular edge, generating lamellipodia and membrane ruffles; Cdc42 induces finger-like cell surface protrusions called filopodia (Burrige and Wennerberg, 2004).

Various aspects of neuronal development are regulated by Rho GTPases including neuronal outgrowth, axonal pathfinding, and dendritic spine formation (Govek et al., 2005). Formation of neurites depends on Rac1 and Cdc42 activity, concomitant with RhoA inactivation (Aoki et al., 2004; Jeon et al., 2011; Sarnier et al., 2000). Moreover, Rac1 and RhoA play distinct roles during dendrite formation. While RhoA and its effector kinase ROCK shape neuronal morphology by inhibiting dendritic pruning, Rac1 activity is necessary for the formation of dendritic spines (Nakayama et al., 2000). Cdc42 also promotes the complexity of dendrites, although to a lesser extent than Rac1 (Kuhn et al., 2000; Ruchhoeft et al., 1999).

Furthermore, actin dynamics is not only regulated by upstream pathways, but also impacts on downstream processes, not only by directly affecting RNA pol II-dependent

transcription as described above, but also by regulating the activity of the serum response factor (SRF). The transcription factor SRF was found to be regulated in response to changes in the G-/F-actin equilibrium via its coactivator MAL (also known as MKL-1 or MRTF-A), which shuttles from the cytosol to the nucleus (Figure 2). Under normal conditions and bound to G-actin, MAL is rapidly exported from the nucleus. Triggered by serum-stimulated activation of the GTPase RhoA leading to actin polymerization, however, it is released from G-actin and translocated to the nucleus, where it activates SRF resulting in the transcription of genes with serum responsive elements (SREs) (Posern and Treisman, 2006; Vartiainen et al., 2007). ABPs influencing actin dynamics in the cytosol or the nucleus have also been linked to SRF activity. For example, nuclear formins were revealed as potent activators of SRF (Baarlink et al., 2013). SRF-responsive genes encode regulators of the actin and microtubule cytoskeleton, cell growth and motility, adhesion, extracellular matrix synthesis and processing, and transcription (Esnault et al., 2014).

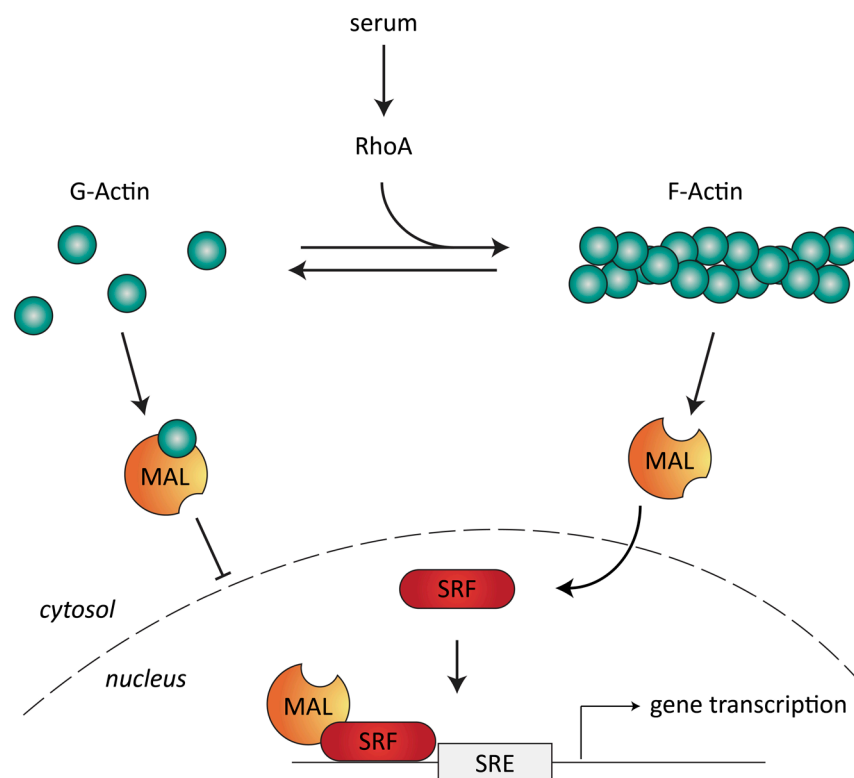


Figure 2. The pathway of the serum response factor (SRF). Serum activates the small Rho GTPase RhoA, which shifts the G-/F-actin equilibrium towards F-actin. In the resting state, the SRF cofactor MAL is inhibited by binding to G-actin. With increasing actin polymerization, MAL is released from G-actin and translocated to the nucleus, where it activates SRF. SRF activity leads to the transcription of genes with serum responsive elements (SREs) in their regulatory regions.

In neurons, MAL and SRF regulate migration, axonal outgrowth and guidance, dendritic branching, spine morphogenesis, and learning behavior (Kalita et al., 2012). MAL is

particularly highly expressed in the hippocampus, and to a lesser extent in the olfactory bulb, caudate putamen, and cerebral cortex (Shiota et al., 2006). RNAi-mediated inhibition of MAL in hippocampal or cortical neurons led to a decrease of neurite length and dendritic processes suggesting that SRF control the formation of neural circuits (Knöll et al., 2006; Shiota et al., 2006). Evidence from SRF knockout mice showing less dendritic spines and learning deficits further supports the idea of the MAL-SRF pathway playing a significant role in memory formation (Etkin et al., 2006; Ramanan et al., 2005; Stritt and Knöll, 2010).

1.3.4. Synaptic plasticity, learning and memory

Actin functions as a key player impacting on synaptic transmission. Actin dynamics regulated by a variety of ABPs are crucial in shaping synaptic morphology, but furthermore affect neurotransmitter vesicle release and receptor distribution at the postsynaptic spine, thereby impacting on synaptic transmission (Cingolani and Goda, 2008; Dillon and Goda, 2005).

In presynaptic terminals, actin is implicated in all steps of the synaptic vesicle cycle, which includes docking, priming, fusion (leading to neurotransmitter release) and recycling (i.e. endocytosis). While it serves as a guide for neurotransmitter vesicles, it might also act as a physical barrier for the priming step (Cingolani and Goda, 2008; Lee et al., 2013). Mobility of synaptic vesicles was shown to increase upon treatment with actin depolymerizing agents (cytochalasin and latrunculin), providing evidence for the dual function of actin at the presynapse (Jordan et al., 2005; Shtrahman et al., 2005). The release of neurotransmitter is directly affected by alterations in actin dynamics as shown by experiments with latrunculin A. Moreover, an increase in paired-pulse facilitation was found, supporting an increased release probability of neurotransmitter vesicles upon actin depolymerization (Morales et al., 2000).

At the postsynaptic-site, which is composed of a dendritic spine in most excitatory synapses, actin is involved in shape, receptor anchoring and trafficking. It has become evident, that synapse morphology is intimately linked with synaptic function: smaller spines are less stable, exhibit less neurotransmitter receptors, and consequently show a lower synaptic strength (Hotulainen and Hoogenraad, 2010). During long-term potentiation (LTP), the G-/F-actin ratio is shifted towards F-actin and the spine volume increases, while the opposite was found for long-term depression (LTD) (Fukazawa et al., 2003; Okamoto et al., 2004). Different shapes of spines have been identified and, being a highly dynamic structure, these shapes are not static, but undergo constant turnover and remodeling (Bourne and Harris, 2008). Neuronal activity modulates dendritic spine maturation from a filopodia-like shape (thin spines), to shorter and thicker spines lacking a well-defined neck (stubby spines), and finally to larger spines with a pronounced head

and neck structure (mushroom spines) (Calabrese et al., 2006). These findings suggest dendritic spine plasticity to be a crucial process of learning and memory (Yuste and Bonhoeffer, 2001). Moreover, the glutamate receptors AMPA (α -amino-3-hydroxy-5-methyl-4-isoxazole-propionic acid receptor) and NMDA (N-Methyl-D-aspartic acid receptor) have been shown to disperse from the post-synaptic density upon actin depolymerization (Allison et al., 1998). Yet, distinct specialized actin populations appear to exist within the dendritic spine, as suggested by many studies (Osterweil et al., 2005; Zhou et al., 1994).

A study using superresolution microscopy and photoactivatable GFP-labeled actin revealed distinct sites of actin polymerization at the tip of the spines but also away from the synapse to some extent. Within dynamic subregions, a structure comprised of dense F-actin with heterogeneous distribution was proposed due to slower movement of photoactivated GFP-actin. Actin filaments in the neck were often oriented with the (growing) barbed end towards the dendritic shaft (Frost et al., 2010). In addition to actin, dynamic microtubules have been shown to transiently enter dendritic spines to influence on the actin cytoskeleton and spine dynamics (Jaworski et al., 2009).

Altogether, an active contribution of actin dynamics to synaptic transmission at pre- and post-synaptic sites is well recognized. With dendritic spines being a key parameter in synaptic transmission, it is not surprising that many stress-dependent psychiatric and neurologic diseases – including amongst others schizophrenia, compulsive behavior, autism, and Alzheimer’s disease – have been associated with anomalies in spine number and morphology (Newey et al., 2005; Spronsen and Hoogenraad, 2010). These findings also provide the basis for a central role of actin dynamics during stress response and upon maladaptation in affective disorders.

1.4. Effects of antidepressants on cytoskeletal dynamics

Mood disorders like depression, anxiety or bipolar disorder are a major disability worldwide. The discovery of tricyclic antidepressants (TCAs) led to the development of the monoamine deficiency hypothesis of depression, stating an imbalance of serotonergic and noradrenergic function (Lanni et al., 2009). This hypothesis was strengthened when the first selective serotonin reuptake inhibitor (SSRI) – fluoxetine – was developed showing a comparable therapeutic outcome with concomitant reduction of side effects (Montgomery, 1989).

Yet, nowadays evidence is accumulating that all classes of antidepressants might affect further cellular pathways besides the monoamines resulting in their therapeutic benefit.

While the knowledge about the etiology of mood disorders is expanding, limits of the monoamine hypothesis have been identified. Currently available therapies are far from being satisfactory: antidepressants are not effective for some patients, the onset of therapeutic benefits can take up four to six weeks and there are still major side effect (Chang and Fava, 2010).

Another proposed model is the “disturbed cytoskeletal theory” of mood disorders. Nakatani et al. analyzed gene expression of mice either vulnerable or resilient to depression-like behavior and found that an altered balance towards actin depolymerization might contribute to the disease. They identified a reduction in Cap1, an important mediator of rapid actin turnover, as a quantitative trait in mice vulnerable to depression as well as a trend to its reduction in postmortem brains of bipolar patients. Other regulated actin-related proteins in the vulnerable animal model included cofilin1 and profilin1 (upregulated) and the Rho family GTPase member Pak1 (downregulated) (Nakatani et al., 2007).

Moreover, several antidepressants have been shown to impact on cytoskeletal-dependent processes. The TCA desipramine enhanced microtubule assembly via upregulation of MAP-4 in chronically stressed mice, while fluoxetine upregulated Drebrin A, an actin-associated protein promoting neuronal growth (Yang et al., 2003). Amitriptyline, another TCA, reduced neurite outgrowth in chick cerebral neurons by reducing the activity of adenylate cyclase and therefore cAMP levels, which promotes outgrowth (Wong et al., 1991). A proteomic analysis of prefrontal cortex and hippocampus of a rat model of depression-like behavior revealed escitalopram and nortryptiline to affect actin-related proteins and actin itself in the depression-like behavior sensitive rat line (Piubelli et al., 2011a, 2011b).

1.5. The stress-induced protein DRR1

1.5.1. Identification of a novel, stress-induced protein

A microarray study of the neonatal mouse brain on genes induced upon maternal separation identified *downregulated in renal cell carcinoma gene 1* (DRR1) as one of the most strongly upregulated genes (Liebl et al., 2009). Maternal separation is a robust stressor resulting in profound activation of the HPA axis and is being used as a model of early trauma (Levine, 2001). In the PVN and the CA3 hippocampal region, DRR1 levels were also increased by 24 h of food deprivation in adult mice. The highest mRNA expression of DRR1 in response to stress was found in the hypothalamic paraventricular nucleus (PVN) and the CA3 region of the hippocampus. Basal levels were highest in the septum, the neocortex, the CA3 region of the hippocampus, and the cerebellum. DRR1’s

upregulation was moreover shown to be dependent on the GR, as it was induced in response to the synthetic GR agonist dexamethasone and this induction was blocked by treatment with the GR antagonist RU486. Three conserved glucocorticoid responsive elements (GREs) were identified in the gene regulatory regions of DRR1, although an indirect effect mediated by other transcription factors could not be excluded (Schmidt et al., 2011). The stress-induction of DRR1 was recently validated by a proteomic study measuring gene expression in mice in response to acute stress, where DRR1 was significantly upregulated in the prefrontal cortex (Stankiewicz et al., 2014).

Previously, DRR1 was described as a potential tumor suppressor gene, as it was found to be downregulated in renal cell carcinoma and various cancer cell lines including renal cell, ovarian, cervical, gastric, prostate, and non-small cell lung cancer (Kholodnyuk et al., 2006; Liu et al., 2009; Vanaja et al., 2006; Wang et al., 2000; Yamato et al., 1999). Furthermore, it was downregulated with progression of neuroblastoma, meningioma and malignant glioma. It was expressed at lower levels in malignant gliomas (WHO grade IV), than in diffuse astrocytomas (grade II) (Asano et al., 2010; van den Boom et al., 2006; Fèvre-Montange, 2009). Awakura et al. described promotor hypermethylation as the silencing mechanism in cancer, indicating that its function might be under epigenetic control (Awakura et al., 2008). However, DRR1 was also suggested as a tumor invasive factor in human glioma due to its increasing expression with malignant astrocytoma progression (Le et al., 2010). Moreover, the analysis of shared gene expression patterns in bipolar disorder and schizophrenia provided evidence for a strong increase of DRR1 in dorsolateral prefrontal cortex of patients suffering from either of the diseases, presumably indicating an aberrant adaptation to chronic stress (Shao and Vawter, 2008). Interestingly, DRR1 was also proposed as a candidate biomarker in ulcerative colitis for differential diagnosis with Crohn's disease (Lin et al., 2014).

The protein consists of 144 amino acids (in mammals) and is strongly conserved across most species, including mammals, *Xenopus*, fish, and *Drosophila* (Nakajima and Koizumi, 2014; Zhao et al., 2007). DRR1 is also referred to as *family of sequence similarity 107 member A* (FAM107A) or *Tohoku University cDNA clone A on chromosome 3* (TU3A). Fam107B is the unique paralog of DRR1 consisting of 131 amino acids (in mammals). The sequences of FAM107A and B are highly conserved, except for the 15 N-terminal amino acids of FAM107A (Masana et al., 2015). Due to its induction in response to hyperthermia, FAM107B is also termed heat-shock-inducible tumor small protein (HITS). Although it shares GREs with DRR1, it is not stress-inducible in the adult mouse, but it has been proposed to exert a tumor suppressive function as well (Nakajima et al., 2010, 2012). Basal expression of DRR1 in adult mice is highest in limbic areas of the brain, while FAM107B expression was predominantly found in the forming telencephalon during embryogenesis and neurogenic niches like the dentate gyrus (Masana et al., 2015; Schmidt et al., 2011; Su et al., 2004).

DRR1 was found to strongly colocalize with F-actin structures in the cell like membrane ruffles, filopodia and stress fibers (Schmidt et al., 2011; Wang et al., 2000). Its direct interaction with F-actin was confirmed in F-actin co-sedimentation assays with purified proteins. Additionally, it was suggested to stabilize F-actin by crosslinking filaments into bundles (Schmidt et al., 2011). With its molecular and cellular function being not yet fully unraveled, considering its interaction partners provides interesting insights into its potential impact during stress.

1.5.2. Interaction partners of DRR1

In addition to β -actin, Schmidt et al. identified peroxiredoxin 1 (Prdx1) and protein arginine methyltransferase 5 (Prmt5) as direct or indirect interaction partners of DRR1 via co-immunoprecipitation and mass spectrometry (Schmidt et al., 2011). Moreover, DRR1 was suggested to act as a bridge between actin and microtubule cytoskeletal components, by binding to the microtubule-associated protein 1A (MAP1A) and to have an impact on gene transcription via the transcription factor Tada2 α (Frijters et al., 2010; Le et al., 2010). A short summary of the interactors' functions are provided in the following.

Peroxiredoxins protect thiols against oxidation and have been proposed as important players in the peroxide detoxification of the cell due to their high abundance (Wood et al., 2003). This mechanism is of relevance in removing peroxides produced at basal levels as normal cell metabolites, but furthermore to avoid damage of cellular components by H₂O₂ transiently produced as intracellular messenger. Increasing evidence supports the notion of H₂O₂ as a relevant intracellular messenger modifying protein function through oxidation of crucial cysteines, for example of protein tyrosine phosphatases (Sies, 2014).

The second interactor of DRR1, Prmt5, mediates methylation of a variety of proteins including histones, many RNA-binding proteins, signal transducers, DNA-binding transcriptional regulators, and transcriptional coregulators (Lee and Stallcup, 2009). Although protein phosphorylation is likely to be the most studied post-translational modification, protein methylation is also quite relevant, as about 2% of the nuclear proteins are methylated (Boffa et al., 1977).

Le et al. identified the light chain 2 (LC2) subunit of MAP1A as a candidate DRR1-binding protein. This interaction is presumably relevant for the disassembly of focal adhesions and malignant glioma invasion (Le et al., 2010). MAP1-family members bind along and stabilize the microtubule lattice (Halpain and Dehmelt, 2006). They exhibit a temporal and regional expression pattern in the nervous system, with MAP1A preferentially localizing to dendrites and post-synaptic densities in adult neurons, indicating that the interaction with DRR1 might be significant mature neurons

(Schoenfeld et al., 1989). Interestingly, MAP1A was identified as an interaction partner of DISC-1, a candidate gene for schizophrenia and bipolar disorder, suggesting a potential relationship between DRR1 and DISC-1 in addition to the described increase of DRR1 in schizophrenia patients (Morris et al., 2003; Shao and Vawter, 2008).

A further study suggested the transcription factor Tada2 α as an interaction partner of DRR1. Being a core protein of the histone acetyltransferase complex, this interaction suggests an involvement of DRR1 in epigenetic gene regulation (Frijters et al., 2010).

1.5.3. Cellular effects of DRR1

As mentioned above, DRR1 was suggested as a promotor of tumor invasion, as it significantly enhanced the invasiveness of the U251 glioma cell line. This effect was attributed to its ability to bind to F-actin and the LC2 chain of MAP1A, thereby promoting the disassembly of focal adhesions. While RNAi-mediated downregulation of DRR1 yielded round-shaped glioma cells, DRR1 overexpression altered cell morphology towards an elongated spindle shape promoting motility (Le et al., 2010). Meanwhile, an apparent increase in F-actin correlating with DRR1 expression level was also described (Schmidt et al., 2011).

DRR1's novel mechanism of tumor invasion was attributed to its recruitment of the kinase AKT to focal adhesions. Dependent on adhesion and the activity of SRC-family kinases, it increases phosphorylation of AKT (at both phosphorylation sites T308 and S473) leading to its activation and thereby promoting downstream effectors of AKT involved in cell proliferation, survival, metabolism, and invasion (Dudley et al., 2013).

1.5.4. Effects of DRR1 on neuronal cells

DRR1 is highly expressed during embryogenesis in the brain the spinal cord. In particular, its expression was found in the axonal projections of central and peripheral neural cells of mice during embryonic day E10.5 to 16.5. There, it was proposed to promote cell survival, as an RNAi-mediated knock down of DRR1 caused cell death in comparison to the control RNAi (Asano et al., 2010).

Moreover, in 3-4 weeks old primary rat hippocampal neurons, endogenous DRR1 was visualized as a punctuate pattern along the neurites. Neurite outgrowth was inhibited with heterologous expression of DRR1 in hippocampal neurons and the Neuro2a cell line, but it did not affect already developed neurites. Staining signals overlapping with synaptophysin and synapsin indicated localization to the pre-synaptic site, while it was also partially found at post-synaptic boutons. Stable virus-mediated increase of DRR1 in mice hippocampi indicated a reduction of spine density on apical dendrites. Interestingly, it

affected efficacy of synaptic transmission by increasing paired-pulse facilitation but reducing LTP magnitude (Schmidt et al., 2011).

1.5.5. DRR1 shapes cognition and social behavior

Upregulation of DRR1 using adeno-associated virus in the CA3 region of the hippocampus had no negative impact on normal locomotor activity of mice in homecage or open field. With a virus-mediated increase similar to the one observed by stress, DRR1 enhanced hippocampal-dependent memory in a Y-maze and the object relocation test, and cognitive flexibility in the reversal learning task (Schmidt et al., 2011).

To assess regional specificity of the behavioral effect of increased DRR1, it was overexpressed in the lateral septum, again using an adeno-associated virus. DRR1 was expressed in neurons and astrocytes of the lateral septum, it increased social behavior of the mice but did not impact on cognitive, anxiety-like or anhedonic behavior. These findings support the idea of DRR1 as a protective buffer counterbalancing aversive stress effects on social behavior (Masana et al., 2014). It is likely that timing and degree of DRR1 upregulation upon stress are crucial, but maladaptive consequences, e.g. due to long-term stress exposure, cannot be excluded.

1.6. Objective

The link between stress and actin dynamics appears to be a critical component of the general adaptation mechanism (Masana et al., 2014; Schmidt et al., 2011). However, up to now, a profound mechanistic understanding of the pathway from stress to neuronal reorganization and cognitive performance remains elusive. Assuming that the mechanism of DRR1 is not only relevant for coping with stress but also during tumor development and progression, elucidating DRR1's mechanism of action could contribute to several physiologically relevant processes. For the present work, the aim was to dissect the molecular mechanism of DRR1 and its significance in actin-dependent cell function. As a second approach the effects of certain antidepressants on actin dynamics were to be analyzed.

2. Material

2.1. Consumable supplies

NAME	MANUFACTURER
Cell culture dishes, multi-well plates	TPP (Trasadingen, Switzerland)
Cell scrapers sterile	Peske (Aindlingen-Arnhofen)
Centrifugation tubes 50 mL, 15 mL	TPP (Trasadingen, Switzerland)
Centrifugation tubes for the UZ	Beckman (Krefeld)
Coverslips	Carl Roth (Karlsruhe)
Cryotubes 2 mL	TPP (Trasadingen, Switzerland)
Electroporation cuvettes	Bio-Rad Laboratories (München)
Eppendorf reaction tubes 1.5 mL, 2 mL	TPP (Trasadingen, Switzerland)
Eppendorf reaction tubes 1.5 mL, low-binding	Eppendorf (Wesseling-Berzdorf)
Eppendorf reaction tubes 1.5 mL, safe-lock	Eppendorf (Wesseling-Berzdorf)
Filter paper 3 MM Whatman	Carl Roth (Karlsruhe)
Folded filter	Carl Roth (Karlsruhe)
Glass slides	Carl Roth (Karlsruhe)
Luminometer plate 96 well (white)	Nalgene Nunc International (USA)
Nitrocellulose membrane	GE Healthcare (Freiburg)
Pasteur pipettes 230 mm	Carl Roth (Karlsruhe)
Petri dishes unsterile	TPP (Trasadingen, Switzerland)
Pipette Stripette 1, 5, 10, 25 mL	Corning Inc. (Acton, USA)
Pipette tips 0.5-10 μ L, 5-200 μ L, 100-1000 μ L	Corning Inc. (Acton, USA)
Plastic supplies for tissue culture	TPP (Trasadingen, Switzerland)
Serological pipettes 2, 5, 10, 25 mL	Peske (Aindlingen-Arnhofen)
Sterile filter units	Nalgene Nunc International (USA)
Vivaspin 20 filter columns (30 kDa MWCO)	GE Healthcare (Freiburg)

Table 1. List of consumable supplies.

2.2. Chemicals

NAME	MANUFACTURER
3-(N-morpholino)propanesulfonic acid (MOPS)	Carl Roth (Karlsruhe)
Acetic acid (CH ₃ COOH)	Sigma-Aldrich (St. Louis, USA)
Acrylamide/Bis Solution, 37.5:1 (30% w/v)	Serva (Heidelberg)
Adenosine 5'-triphosphate (ATP)	Sigma-Aldrich (St. Louis, USA)
Agar agar	Carl Roth (Karlsruhe)
Agarose	Biozym (Oldenburg)
Ammonium sulfate	Carl Roth (Karlsruhe)
Ammonium persulfate (APS)	Carl Roth (Karlsruhe)
Ampicillin	Sigma-Aldrich (St. Louis, USA)
AMPUWA ddH ₂ O	Fresenius Kabi (Bad Homburg)
BES	Carl Roth (Karlsruhe)
Boric acid	Sigma-Aldrich (St. Louis, USA)
Bovine Serum Albumin (BSA)	Sigma-Aldrich (St. Louis, USA)
Brilliant blue G	Sigma-Aldrich (St. Louis, USA)
Bromophenol blue	Sigma-Aldrich (St. Louis, USA)
Calcium chloride (CaCl ₂ · 2 H ₂ O)	Carl Roth (Karlsruhe)
Casein	Carl Roth (Karlsruhe)
Chloroform (CHCl ₃)	Sigma-Aldrich (St. Louis, USA)
Citalopram hydrobromide	Sigma-Aldrich (St. Louis, USA)
Clomipramine hydrochloride	Sigma-Aldrich (St. Louis, USA)
Coomassie Brilliant Blue G	Sigma-Aldrich (St. Louis, USA)
Crosslinker DSS, DSG, BMB	Thermo Fisher (Rockford, USA)
Cytochalasin D (Cyto D)	Sigma-Aldrich (St. Louis, USA)
DAPI (4',6-diamidino-2-phenylindole)	Sigma-Aldrich (St. Louis, USA)
Deoxynucleotide triphosphates (dNTPs)	Peqlab (Erlangen)
Dipotassium phosphate (K ₂ HPO ₄ · 3 H ₂ O)	Carl Roth (Karlsruhe)
Disodium phosphate (Na ₂ HPO ₄)	Carl Roth (Karlsruhe)
DMSO (dimethyl sulfoxide)	Sigma-Aldrich (St. Louis, USA)
Doxepin hydrochloride	Sigma-Aldrich (St. Louis, USA)
DTT (1,4-Dithiothreitol)	Carl Roth (Karlsruhe)
Ethanol absolute p.a.	Sigma-Aldrich (St. Louis, USA)
Ethidium bromide	Sigma-Aldrich (St. Louis, USA)
Ethylene glycol tetraacetic acid (EGTA)	Carl Roth (Karlsruhe)
Fibronectin (bovine)	Merck Millipore (Darmstadt)
Gelatin	Sigma-Aldrich (St. Louis, USA)
Glucose	Carl Roth (Karlsruhe)
Glycerol	Merck Millipore (Darmstadt)

Glycin	Sigma-Aldrich (St. Louis, USA)
Hydrochloric acid (HCl)	Merck Millipore (Darmstadt)
IGEPAL	Sigma-Aldrich (St. Louis, USA)
Isopropyl alcohol	Sigma-Aldrich (St. Louis, USA)
Isopropyl- β -D-1-thiogalactopyranoside (IPTG)	Peqlab (Erlangen)
Laminin	Sigma-Aldrich (St. Louis, USA)
Magnesium chloride ($MgCl_2$)	Carl Roth (Karlsruhe)
Magnesium sulfate ($MgSO_4$)	Merck Millipore (Darmstadt)
Maltose	Carl Roth (Karlsruhe)
Manganese(II) chloride ($MnCl_2 \cdot 4 H_2O$)	Carl Roth (Karlsruhe)
Methanol	Sigma-Aldrich (St. Louis, USA)
Milk powder	Carl Roth (Karlsruhe)
Paraformaldehyde (PFA)	Carl Roth (Karlsruhe)
Phalloidin Alexa Fluor 488	Life Technologies (Frankfurt)
Phalloidin Alexa Fluor 546	Life Technologies (Frankfurt)
Phosphoric Acid, 85%	Sigma-Aldrich (St. Louis, USA)
PMSF (Phenylmethylsulfonyl fluoride)	Sigma-Aldrich (St. Louis, USA)
Poly-D-lysine	Sigma-Aldrich (St. Louis, USA)
Potassium acetate (CH_3COOH)	Carl Roth (Karlsruhe)
Potassium chloride (KCl)	Carl Roth (Karlsruhe)
Potassium hydroxide (KOH)	Carl Roth (Karlsruhe)
Ribonuclease A	Sigma-Aldrich (St. Louis, USA)
Rubidium dichloride ($RbCl_2$)	Carl Roth (Karlsruhe)
Sodium chloride (NaCl)	Carl Roth (Karlsruhe)
Sodium dodecyl sulfate (SDS)	Fluka (USA)
Sodium hydroxide (NaOH)	Merck Millipore (Darmstadt)
Sucrose	Carl Roth (Karlsruhe)
TEMED (Tetramethylethylenediamine)	Carl Roth (Karlsruhe)
Tris-(hydroxymethyl)-aminomethane (Tris)	Riedel-de Haen (Seelze)
Triton X-100	Carl Roth (Karlsruhe)
Tween 20	Sigma-Aldrich (St. Louis, USA)
β -Mercaptoethanol	Sigma-Aldrich (St. Louis, USA)

Table 2. List of chemicals.

2.3. Solutions and media

NAME	MANUFACTURER
Antibiotic-Antimycotic (100x)	Life Technologies (Frankfurt)
B-27 Supplement (50x) serum free	Life Technologies (Frankfurt)
Dulbecco´s Modified Eagle Medium (DMEM), High Glucose w/o Phenol red	Life Technologies (Frankfurt)
Fetal bovine serum (FBS)	Life Technologies (Frankfurt)
GlutaMAX Supplement	Life Technologies (Frankfurt)
HBSS	Life Technologies (Frankfurt)
HEPES (1M)	Life Technologies (Frankfurt)
LB broth	Sigma-Aldrich (St. Louis, USA)
Neurobasal A-Medium	Life Technologies (Frankfurt)
PBS (10x)	Life Technologies (Frankfurt)
S.O.C. Medium	Life Technologies (Frankfurt)
Sodium pyruvate solution (100x)	Life Technologies (Frankfurt)
Trypan blue	Carl Roth (Karlsruhe)
Trypsin-EDTA Solution (10x)	Life Technologies (Frankfurt)

Table 3. List of solutions and media.

2.4. Kits and ready-to-use materials

NAME	MANUFACTURER
Albumin Standard	Thermo Scientific (Rockford, USA)
BCA Protein Assay	Thermo Scientific (Rockford, USA)
β -actin	Cytoskeleton, Inc. (Denver, USA)
BSA (100x) for restriction of DNA	NEB (Frankfurt)
Dynabeads Protein G	Life Technologies (Frankfurt)
EndoFree Plasmid Maxi Kit	Qiagen (Hilden)
EZ-PCR Mycoplasma Test Kit	Biological Industries (Frankfurt)
GeneArt Site-Directed Mutagenesis System	Life Technologies (Frankfurt)
GFP-Trap (with agarose beads)	Chromotek (München)
Immobilon Western Chemiluminescent HRP Substrate	Merck Millipore (Darmstadt)
Lipofectamine 2000	Life Technologies (Frankfurt)
NEBuffers 1-4 for restriction of DNA	NEB (Frankfurt)
NucleoBond AX100 Columns	Macherey-Nagel (Düren)
peqGOLD DNA ladder mix	Peqlab (Erlangen)
peqGOLD Prestained Protein-Marker IV	Peqlab (Erlangen)

ProLong Gold Antifade	Life Technologies (Frankfurt)
Protease inhibitor cocktail (PI) containing 2 mM AEBSF, 0.3 μ M Aprotinin, 130 μ M Bestatin, 14 mM E-64, 1 mM Leupeptin, and 1 mM EDTA	Sigma-Aldrich (St. Louis, USA)
QIAquick Gel Extraction Kit	Qiagen (Hilden)
TurboFect Transfection Reagent	Thermo Scientific (Rockford, USA)

Table 4. List of kits and ready-to-use materials.

2.5. Enzymes

2.5.1. Restriction endonucleases

All restriction endonucleases were purchased from NEB (Frankfurt).

2.5.2. DNA polymerases and ligases

Herculase II Fusion DNA Polymerase (and 5x buffer and DMSO)	Agilent Technologies (Santa Clara, USA)
Pwo Polymerase (and 10x buffer)	Peqlab (Erlangen)
T4-DNA Ligase (and 10x buffer)	NEB (Frankfurt)
Taq DNA Polymerase (and 10x buffer and MgCl ₂)	Life Technologies (Frankfurt)

2.6. Antibodies

2.6.1. Primary antibodies

NAME	HOST	MANUFACTURER
anti-Prx1 (N-19)	goat	Santa Cruz Biotech. (Heidelberg)
anti-acetyl-Histone H4	rabbit	Upstate (Schwalbach)
anti-Synaptophysin	mouse	Cell Signaling (Frankfurt)
anti-Actin (I-19)	goat	Santa Cruz Biotech. (Heidelberg)
anti-AKT	rabbit	Cell Signaling (Frankfurt)
anti-DRR1	rabbit	Biogenes (Berlin)

anti-FLAG-M2-HRP	mouse	Sigma-Aldrich (St. Louis, USA)
anti-GFP (B-2)	mouse	Santa Cruz Biotech. (Heidelberg)
anti-Histone Core	sheep	Abcam (Cambridge, UK)
anti-MBP-HRP	mouse	NEB (Frankfurt)
anti-Prmt5	mouse	Santa Cruz Biotech. (Heidelberg)
anti-PSD95	mouse	Thermo Scientific (Rockford, USA)

Table 5. List of primary antibodies.

2.6.2. Secondary antibodies

NAME	HOST	MANUFACTURER
anti-goat Alexa Fluor 488	donkey	Life Technologies (Frankfurt)
anti-goat Alexa Fluor 594	donkey	Life Technologies (Frankfurt)
anti-goat HRP	donkey	Santa Cruz Biotech. (Heidelberg)
anti-mouse Alexa Fluor 488	donkey	Life Technologies (Frankfurt)
anti-mouse Alexa Fluor 546	goat	Life Technologies (Frankfurt)
anti-mouse HRP	goat	Cell Signaling (Frankfurt)
anti-rabbit Alexa Fluor 488	goat	Life Technologies (Frankfurt)
anti-rabbit Alexa Fluor 488	donkey	Life Technologies (Frankfurt)
anti-rabbit Alexa Fluor 647	goat	Life Technologies (Frankfurt)
anti-rabbit HRP	goat	Cell Signaling (Frankfurt)
anti-sheep HRP	rabbit	Santa Cruz Biotech. (Heidelberg)

Table 6. List of secondary antibodies.

2.7. Bacterial clades

CLADE	GENOTYPE
<i>E. coli</i> BL21(DE3)pLysS	B F- dcm ompT hsdS(r B-;m B-) gal λ (DE3)[pLysS Cam ^r]
<i>E. coli</i> DH5 α	F- Φ 80LacZ Δ M15 Δ (lacZYA-argF)U169 deoR recA1 endA1 hsdR17 (r k-;m r+) phoA supE44 thi-1gyrA96relA1

Table 7. List of bacterial clades.

2.8. Cell lines

NAME	CELL TYPE	ATCC CATALOG #
HEK-293	human kidney cells	CRL-1573
HeLa	human cervix carcinoma cells	CCL-2

Table 8. List of cell lines.

2.9. Oligonucleotides

NAME	SEQUENCE (5' – 3')	APPLICATION
3'-HindIII-DRR1m	GGC AGA AGC TTG ATG GAG GGA GCT CTA CAG	Cloning
3'-HindIII-DRR1m- FLAG	GCA GAA GCT TGC TCA CTT GTC ATC GTC GTC CTT GTA GTC CAG TGC TCT TTC CTC GCT GGT	Cloning
5'-XhoI-DRR1m	TGC CTC CTC GAG CCT CCA TGT ACT CAG AGA	Cloning
C94A-F	GCC AAG CGG ATG CAG GCC CCC TTC AAG CAG GAG	Cloning
C94A-R	CTC CTG CTT GAA GGG GGC CTG CAT CCG CTT GGC	Cloning
C94S-F	GCC AAG CGG ATG CAG AGC CCC TTC AAG CAG G	Cloning
C94S-R	CCT GCT TGA AGG GGC TCT GCA TCC GCT TGG C	Cloning
dN2-XhoI-16_F	CAT CCT CGA GAC ATG GCC AGA CCA GAG TAC	Cloning
DRR1m-ΔM-fw	AGG GGC TTG GGT ATG GAC AGC CCC TTC AAG CAG GAG CTG CT	Cloning
DRR1m-ΔM-rv	AGC AGC TCC TGC TTG AAG GGG CTG TCC ATA CCC AAG CCC CT	Cloning
DRR1m-HindIII-112- rev	ATA GAA GCT TCA TCA GTT TTC CAG CTG GTT CAG TC	Cloning
DRR1m-HindIII- FLAG-112-rev	ATA GAA GCT TGC TCA CTT GTC ATC GTC GTC CTT GTA GTC GTT TTC CAG CTG GTT CAG TC	Cloning
DRR1m-XhoI-61-fw	TGA TCT CGA GGT ATG GAC AGC AAG CCT GAG	Cloning
L15M-F	ATC GAG GGA ATG ATG GCC AGA CCA GAG TAC AG	Cloning
L15M-R	TCT GGC CAT CAT TCC CTC GAT GTC AGC CCG CTC	Cloning
M13	TGT AAA ACG ACG GCC AG	Sequencing
N-HindIII-60_R	CTA TAA GCT TGC CTA ACC CAA GCC CCT TTT G	Cloning
P19L-F	CTC ATG GCC AGA CTA GAG TAC AGA GAG TGG AAC	Cloning

P19L-R	CTC TCT GTA CTC TAG TCT GGC CAT GAG TCC CTC	Cloning
PE122AA-F	AGA GAC GAG GAC CAC GCC GCC GCC TTC ATC AAA GTC CGG GAA	Cloning
PE122AA-R	TTC CCG GAC TTT GAT GAA GGC GGC GGC GTG GTC CTC GTC TCT	Cloning
PE65AA-F	TTG GGT ATG GAC AGC AAG GCC GCC CTG CAG CGA GTT CTA GAG	Cloning
PE65AA-R	CTC TAG AAC TCG CTG CAG GGC GGC CTT GCT GTC CAT ACC CAA	Cloning
pRK5SV40.1	CTA TAG AAT AAC ATC CAC	Sequencing

Table 9. List of oligonucleotides.

2.10. Plasmids

NAME	FEATURES	SOURCE	VECTOR
pMAL-cR1	Cloning vector for protein expression in prokaryotic cells with N-terminal MBP-Fusion.	NEB (Frankfurt)	pMAL-cR1
pRK5-SV40-Pur-MCS (pRK5)	Cloning vector for protein expression in mammalian cells.	Plasmid obtained from G. Wochnik	pRK5
pEGFP-C1	Cloning vector for protein expression with N-terminal EGFP in mammalian cells.	Clontech (Saint-Germain-en-Laye, France)	pEGFP-C1
pMAL-DRR1	Recombinant protein expression of DRR1 in E.coli with N-terminal MBP.	Plasmid obtained from J. Schülke	pMAL-cR1
pMAL-N	Recombinant protein expression of DRR1-N in E.coli with N-terminal MBP.	Subcloned from pRK5-N with XhoI and HindIII	pMAL-cR1
pMAL-dN2	Recombinant protein expression of DRR1- Δ N2 in E.coli with N-terminal MBP.	Subcloned from pRK5- Δ N2 with XhoI and HindIII	pMAL-cR1
pMAL-dN	Recombinant protein expression of DRR1- Δ N in E.coli with N-terminal MBP.	Subcloned from pRK5- Δ N with XhoI and HindIII	pMAL-cR1
pMAL-dC	Recombinant protein expression of DRR1- Δ C in E.coli with N-terminal MBP.	Subcloned from pRK5- Δ C with XhoI and HindIII	pMAL-cR1
pMAL-dM	Recombinant protein expression of DRR1- Δ M in E.coli with N-terminal MBP.	Subcloned from pRK5- Δ M with XhoI and HindIII	pMAL-cR1
pMAL-M	Recombinant protein expression of DRR1-M in E.coli with N-terminal MBP.	Subcloned from pRK5-M with XhoI and HindIII	pMAL-cR1
pMAL-C94A	Recombinant protein expression of DRR1-C94A in E.coli with N-terminal MBP.	Cloned with Site-Directed Mutagenesis	pMAL-cR1
pMAL-C94S	Recombinant protein expression of DRR1-C94S in E.coli with N-terminal MBP.	Cloned with Site-Directed Mutagenesis	pMAL-cR1
pMAL-dPEPE	Recombinant protein expression of DRR1-PEPE in E.coli with N-terminal MBP.	Subcloned from pRK5-PEPE with XhoI and HindIII	pMAL-cR1

pMAL-L15M	Recombinant protein expression of DRR1-L15M in E.coli with N-terminal MBP.	Subcloned from pRK5-L15M with XhoI and HindIII	pMAL-cR1
pMAL-P19L	Recombinant protein expression of DRR1-L15M in E.coli with N-terminal MBP.	Subcloned from pRK5-P19L with XhoI and HindIII	pMAL-cR1
pRK5-DRR1	Expression of murine DRR1 in mammalian cells.	Plasmid obtained from J. Schülke	pRK5
pRK5-DRR1-F	Expression of murine DRR1-FLAG in mammalian cells.	Plasmid obtained from J. Schülke	pRK5
pRK5-N	Expression of murine DRR1-N in mammalian cells.	Cloned with PCR and mutation primers	pRK5
pRK5-dN2	Expression of murine DRR1-ΔN2 in mammalian cells.	Cloned with PCR and mutation primers	pRK5
pRK5-dN	Expression of murine DRR1-ΔN in mammalian cells.	Cloned with PCR and mutation primers	pRK5
pRK5-dN-F	Expression of murine DRR1-ΔN-FLAG in mammalian cells.	Cloned with PCR and mutation primers	pRK5
pRK5-dC	Expression of murine DRR1-ΔC in mammalian cells.	Cloned with PCR and mutation primers	pRK5
pRK5-dC-F	Expression of murine DRR1-ΔC-FLAG in mammalian cells.	Cloned with PCR and mutation primers	pRK5
pRK5-dM	Expression of murine DRR1-ΔM in mammalian cells.	Cloned with PCR and mutation primers	pRK5
pRK5-dM-F	Expression of murine DRR1-ΔM-FLAG in mammalian cells.	Cloned with PCR and mutation primers	pRK5
pRK5-M	Expression of murine DRR1-M in mammalian cells.	Cloned with PCR and mutation primers	pRK5
pRK5-M-F	Expression of murine DRR1-M-FLAG in mammalian cells.	Cloned with PCR and mutation primers	pRK5
pRK5-C94A	Expression of murine DRR1-C94A in mammalian cells	Subcloned from pRK5-C94A with XhoI and HindIII	pRK5
pRK5-C94A-F	Expression of murine DRR1-C94A-FLAG in mammalian cells	Subcloned from pRK5-C94A with XhoI and HindIII	pRK5
pRK5-C94S	Expression of murine DRR1-C94S in mammalian cells	Subcloned from pRK5-C94A with XhoI and HindIII	pRK5
pRK5-C95S-F	Expression of murine DRR1-C94S-FLAG in mammalian cells	Subcloned from pRK5-C94A with XhoI and HindIII	pRK5
pRK5-PE65AA	Expression of murine DRR1-PE65AA in mammalian cells	Cloned with PCR and mutation primers	pRK5
pRK5-PE65AA-F	Expression of murine DRR1-PE65AA-FLAG in mammalian cells	Cloned with PCR and mutation primers	pRK5
pRK5-PE122AA	Expression of murine DRR1-PE122AA in mammalian cells	Cloned with PCR and mutation primers	pRK5
pRK5-dPEPE	Expression of murine DRR1-PEPE in mammalian cells	Cloned with PCR and mutation primers	pRK5

pRK5-dPEPE-F	Expression of murine DRR1-PEPE-FLAG in mammalian cells	Cloned with PCR and mutation primers	pRK5
pRK5-L15M	Expression of murine DRR1-L15M in mammalian cells	Cloned with PCR and mutation primers	pRK5
pRK5-P19L	Expression of murine DRR1-P19L in mammalian cells	Cloned with PCR and mutation primers	pRK5
pRK5-DRR1-EGFP	Expression of murine DRR1-EGFP in mammalian cells.	Plasmid obtained from J. Schülke	pEGFP-C1
pRK5-N-EGFP	Expression of murine Δ N-EGFP in mammalian cells.	Subcloned from pRK5- Δ N with XhoI and HindIII	pEGFP-C1
pRK5-dN2-EGFP	Expression of murine Δ N-EGFP in mammalian cells.	Subcloned from pRK5- Δ N with XhoI and HindIII	pEGFP-C1
pRK5-dN-EGFP	Expression of murine Δ N-EGFP in mammalian cells.	Subcloned from pRK5- Δ N with XhoI and HindIII	pEGFP-C1
pRK5-dC-EGFP	Expression of murine Δ C-EGFP in mammalian cells.	Subcloned from pRK5- Δ C with XhoI and HindIII	pEGFP-C1
pRK5-dM-EGFP	Expression of murine Δ M-EGFP in mammalian cells.	Subcloned from pRK5- Δ M with XhoI and HindIII	pEGFP-C1
pRK5-M-EGFP	Expression of murine M-EGFP in mammalian cells.	Subcloned from pRK5-M with XhoI and HindIII	pEGFP-C1
pRK5-C94A-EGFP	Expression of murine C94A-EGFP in mammalian cells.	Subcloned from pRK5-C94A with XhoI and HindIII	pEGFP-C1
pRK5-dPEPE-EGFP	Expression of murine PEPE-EGFP in mammalian cells.	Subcloned from pRK5-PEPE with XhoI and HindIII	pEGFP-C1
pRK5-L15M-EGFP	Expression of murine L15M-EGFP in mammalian cells.	Subcloned from pRK5-L15M with XhoI and HindIII	pEGFP-C1
pRK5-P19L-EGFP	Expression of murine P19L-EGFP in mammalian cells.	Subcloned from pRK5-P19L with XhoI and HindIII	pEGFP-C1
3DA.luc	SRF-driven firefly reporter plasmid	Robert Grosse (Universität Marburg, Germany)	
mDia1-dDAD	Control plasmid for SRF activity expressing mDia1-dDAD (inhibitory domain)	Robert Grosse (Universität Marburg, Germany)	
Gaussia-KDEL	SV40-driven gaussia luciferase reporter plasmid (C-terminal ER retention signal)	Project Group Rein	pRK5

Table 10. List of plasmids.

2.11. Instruments

NAME	MANUFACTURER
Balance Voyager 50187	Ohaus (Giessen)
ChemiDoc Imaging System	Bio-Rad Laboratories (München)
Electroporation System, Gene Pulser II	Bio-Rad Laboratories (München)
High-voltage power supply PowerPac 400	Bio-Rad Laboratories (München)

Incubator CB210	Binder (Tuttlingen)
Magnetic stirrer RCT basic IKAMAG	Labortechnik (Staufen)
Microplate reader MR 7000	Dynatech (Denkendorf)
Mini Trans-Blot Cell	Bio-Rad Laboratories (München)
Mini-PROTEAN Electrophoresis system	Bio-Rad Laboratories (München)
Overhead stirrer Rotamix	ELMI (Latvia)
pH meter pH538	WTW (Weilheim)
Pipettes PIPETMAN	Gilson (Middletown, USA)
Sonicator, Cell Disruptor B15	Branson (USA)
Spectrophotometer DU 640	Beckman (Krefeld)
Stirrer DUOMAX 1030/POLYMAX1040	Heidolph (Schwabach)
Supplies for agarose gels	Bio-Rad Laboratories (München)
Thermocycler Primus 25	Peqlab (Erlangen)
Thermocycler Tgradient	Biometra (Göttingen)
Thermomixer comfort	Eppendorf (Wesseling-Berzdorf)
TriStar LB941 Luminometer	Berthold Tech. (Bad Wildbad)
UV-Transilluminator	Stratagene (La Jolla, USA)
UV-Transilluminator GelDoc	Bio-Rad Laboratories (München)
Vortexer MS2 IKA	Labortechnik (Staufen)
Voyager 50228 (Precision balance)	Ohaus (Giessen)
Water bath type 1008	Gesellschaft für Labortechnik (Burgwedel)
Microscopes:	
Axioplan 2	Carl Zeiss (Jena)
CK30	Olympus (Hamburg)
IX50	Olympus (Hamburg)
LSM FV1000	Olympus (Hamburg)
TSC SP5	Leica (Solms)
Centrifuges:	
Allegra 21	Beckman (Krefeld)
Allegra X-22R	Beckman (Krefeld)
Biofuge pico	Heraeus (Mannheim)
J2 MC (Rotor JA-14)	Beckman (Krefeld)
Refrigerated centrifuge (5417 R)	Eppendorf (Wesseling-Berzdorf)
Refrigerated centrifuge (5804 R)	Eppendorf (Wesseling-Berzdorf)
Ultracentrifuge LB-70M (Rotor: SW 60 Ti)	Beckman (Krefeld)
Varifuge 3.0R	Heraeus (Mannheim)

Table 11. List of instruments.

2.12. Software

NAME	APPLICATION
Adobe Acrobat 8.0	Creating and editing pdf-files
Adobe Illustrator CS3	Editing of figures
Adobe Photoshop CS3	Image processing
FluoView FV1000 (Olympus, Hamburg)	Image acquisition, processing and analysis of confocal microscopy
Image Lab 5.0 (Bio-Rad, München)	Analysis of SDS-PAGE and Western Blot
ImageJ / Fiji	Image processing and analysis
MS Office Home and Student 2010	Office suite for desktop application
Vector NTI 10 (Invitrogen, Karlsruhe)	Sequence analysis of DNA and proteins

Table 12. List of software.

TFB2 buffer: 10 mM MOPS (3-N-morpholino-propansulfonic acid)-KOH
pH 6.8, 10 mM RbCl, 75 mM CaCl₂, 15% glycerol, sterile
filtered.

3.1.3. Transformation

Bacteria were transformed with the heat shock method. For this, 100 μ L of competent bacteria were thawed on ice and 10 μ L of a ligation or 10-50 ng plasmid-DNA were added. After an incubation of 30 min on ice, the heat shock was performed at 42°C for 45 s, then the cells were cooled down on ice for two minutes and 900 μ L of S.O.C. medium was added. The bacteria were then incubated on 37°C for 1 h on a shaker at 400 rpm to enable the expression of antibiotic resistance. Finally the bacteria were streaked on agar plates and incubated at 37°C overnight.

3.1.4. Isolation of DNA from bacteria (Mini/Midi/Maxi)

For Minipreps the pellets (centrifuged for 5 min, 5,000 rpm) of 2/10 mL (high-/low-copy plasmid) of fresh overnight cultures were resuspended in 200/400 μ L resuspension buffer S1. The cells were lysed by addition of 200/400 μ L lysis buffer S2, inverting the tube 6x and incubation at RT for 5 min. Then 200/400 μ L of neutralization buffer S3 were added, the tube was mixed by inverting it 6x, and incubated on ice for 5 min. Subsequently, the cell debris was removed by centrifugation for 30 min at 13,000 rpm. The supernatant containing the plasmid was transferred to a new tube, 500/800 μ L of isopropanol was added to precipitate the DNA. After centrifugation (5 min, 13,000 rpm) the DNA was washed with 1 mL 70% ethanol and centrifugation (5 min, 13,000 rpm). The ethanol was removed and the pellet was air-dried for about 30 min. Finally, DNA was resuspended in 50/30 μ L ddH₂O. The average yield for Minipreps with this protocol was 2-10 μ g plasmid-DNA.

Midipreps were performed with anion-exchange columns AX-100 (Macherey-Nagel, Düren) following the manufacturer's instructions with homemade buffers. The average DNA yield was 20-100 μ g. The DNA pellet was resuspended in about 200-400 μ L ddH₂O.

For transfection of primary neurons, plasmids were purified free of endotoxins with the EndoFree Plasmid Maxi Kit (Qiagen, Hilden) according to the manufacturer's protocol. Plasmids were resuspended in 200 μ L endotoxin-free TE buffer or water included in the kit and subsequently adjusted to a concentration of 1 μ g/ μ L. Plasmid-DNA was stored at -20°C.

S1 buffer: 50 mM Tris-HCl, 10 mM EDTA, pH 8.0, autoclave,
store at 4°C, add 100 μ g/mL RNase A prior to use.

S2 buffer:	200 mM NaOH, 1% SDS.
S3 buffer:	2.8 M KAc, pH 5.1.
N2 buffer:	100 mM Tris, 15% ethanol, 900 mM KCl, 0.15% Triton X-100, adjust to pH 6.3 with H ₃ PO ₄ .
N3 buffer:	100 mM Tris, 15% ethanol, 1.15 M KCl, adjust to pH 6.3 with H ₃ PO ₄ .
N5 buffer:	100 mM Tris, 15% ethanol, 1 M KCl, adjust to pH 8.5 with H ₃ PO ₄ .

3.2. Cloning

In order to analyze the functional domains of DRR1, several mutants (dN, dC, dM, and M) had been cloned during previous work (Kretzschmar, 2010). During the present work, all point mutants were cloned as well as the mutants N, dN2, and dPEPE. Shortly, the point mutants C94A, C94S, and PE65AA were generated with the GeneArt Site-directed Mutagenesis System (Life Technologies, Frankfurt) while N, dN2, L15M, P19L, PE122AA, and dPEPE were generated with mutational primers and linker PCR. Mutants were subcloned into different vectors for specific applications as described in the following chapters. The coding sequence of all constructs was verified by sequencing.

3.2.1. Polymerase chain reaction (PCR)

In vitro amplification of DNA fragments and mutations of DRR1 were performed with the polymerase chain reaction (PCR). All fragments subsequently needed for cloning were amplified with polymerases containing 3' - 5' proofreading exonuclease activity. The PCR reaction was prepared in a total reaction volume of 50 μ l with the following components: 20 ng DNA template, 10-30 pmol of each primer, 200 μ M dNTPs (10 mM stock), 1-2.5 U polymerase, 1x reaction buffer, and ddH₂O. The plasmid pRK5-DRR1 was used as a template for most mutants. PE65AA was used as a template for dPEPE using mutational primers of PE122AA.

The sequences of all primers used in this work are listed in chapter 2.9.

MUTANT	FORWARD PRIMER	REVERSE PRIMER
C94A	C94A-F	C94A-R
C94A	C94S-F	C95S-R
L15M	(A1) 5'-XhoI-DRR1m (A2) L15M_F	L15M_R 3'-HindIII-DRR1m
	(B) 5'-XhoI-DRR1m	3'-HindIII-DRR1m
P19L	(A1) 5'-XhoI-DRR1m (A2) P19L_F	P19L_R 3'-HindIII-DRR1m
	(B) 5'-XhoI-DRR1m	3'-HindIII-DRR1m
N	5'-XhoI-DRR1m	N-HindIII-60_R
dN2	dN2-XhoI-16_F	3'-HindIII-DRR1m
PE65AA	PE64AA-F	PE65AA-R
PE122AA	(A1) 5'-XhoI-DRR1m (A2) PE122AA_F	PE122AA_R 3'-HindIII-DRR1m
	(B) 5'-XhoI-DRR1m	3'-HindIII-DRR1m
dPEPE	(A1) 5'-XhoI-DRR1m (A2) PE122AA_F	PE122AA_R 3'-HindIII-DRR1m
	(B) 5'-XhoI-DRR1m	3'-HindIII-DRR1m

Table 13. Cloned mutants and respective primers used.

The temperature program for the PCR was usually performed as follows:

Initial Denaturation	95°C	5 min	
Denaturation	95°C	30 s	
Annealing	56°C	45 s	25 cycles
Elongation	68°C	30 s	
Final Elongation	68°C	5 min	

Table 14. Standard program for PCR.

If Herculase II Fusion polymerase was used the elongation time was decreased to 20 s, the denaturation temperature was increased to 98°C and the elongation temperature increased to 72°C. PCR products were analyzed on agarose gels loading 5 µL of each reaction.

3.2.2. Site-directed mutagenesis

Site-directed mutagenesis was performed to generate the point mutants C94A, C94S, and PE65AA using the GeneArt Site-directed Mutagenesis System (Life Technologies, Frankfurt) according to the manufacturer. Shortly, the PCR was performed using Herculase II Fusion polymerase and the plasmid pMAL-DRR1 as a template with the following program:

Plasmid methylation	37°C	20 min	
Initial Denaturation	94°C	2 min	
Denaturation	94°C	20 s	
Annealing	57°C	30 s	18 cycles
Elongation	72°C	3.5 min	
Final Elongation	72°C	5 min	

Table 15. PCR program for site-directed mutagenesis.

After the PCR, the mutated plasmids were transformed into DH5 α -T1 *E. coli* cells included in the kit and selected clones were analyzed for successful mutations.

3.2.3. Agarose gel electrophoresis

Agarose gel electrophoresis was performed in order to analyze restricted plasmid-DNA or linear DNA fragments, quantify the amount of DNA or isolate a particular band. The size of the fragments was determined by loading the size marker peqGOLD DNA ladder mix (Peqlab, Erlangen) on the gel. Depending on the size of the DNA fragments, the gels were prepared with 0.8-2% (w/v) agarose. The agarose was added to 60 or 150 mL of 1x TBE buffer in a conical flask and dissolved by heating. After cooling down to at least \sim 60°C, ethidium bromide was added to a final concentration of 0.5 μ g/mL, swirled to mix and poured into the gel tank. The comb was inserted and any bubbles were removed, then the gel was left to dry for at least 30 min. To run the electrophoresis, the gel was transferred to the electrophoresis tank filled with running buffer (1x TBE) and the comb was carefully removed. The DNA samples were prepared with 1:5 volume of DNA loading buffer and carefully loaded on the gel. The electrophoresis was performed at 100 V for 40-60 min. After the run the gels were analyzed with UV light of 302 nm in the UV-Transilluminator (Stratagene, La Jolla, USA).

TBE buffer (10x): 90 mM boric acid, 2.5 mM EDTA, 90 mM Tris-HCl, pH 8.3.

DNA loading buffer (5x): 5% glycerol, 0.5% SDS, 10 mM EDTA, 0.025% bromophenol blue, 0.025% xylene cyanol.

Ethidium bromide: 10 mg/mL

3.2.4. Purification of DNA from agarose gels

Particular DNA fragments, e.g. PCR products or specific restriction bands, were isolated from agarose gels by cutting out the band from the gel with a sterile scalpel. Subsequently, the DNA was purified from the gel with the QIAquick Gel Extraction Kit (Qiagen, Hilden), eluted in 30-50 μL ddH₂O and stored at -20°C.

3.2.5. Restriction of DNA

Restriction of DNA or PCR products with restriction endonucleases was performed in the appropriate buffer following the manufacturer's instructions and BSA was added if needed. Different amounts of DNA were used for the digestion: the whole volume of PCR products for cloning, 5-10 μL of minipreps for control digestions, and 2-10 μg of DNA for other digestions. 2-5 Units of restriction enzyme were added to the reaction and the volume was adjusted to a total of 50 μL with ddH₂O (or 80 μL for overnight digestions). The reaction was performed at 37°C for 2 h or overnight.

3.2.6. Ligation of DNA

Digested PCR products (inserts) were connected to the target vector by ligation of the sticky ends catalyzed by the T4 DNA ligase. In this ATP-dependent reaction a covalent phosphodiester bond is formed between the 3' OH and the 5' phosphate group of the deoxyriboses of vector and insert, respectively. The ligation was performed in a final volume of 20 μL using 1 μL of T4 DNA ligase in 1x reaction buffer at 4°C overnight. On the next day the product was transformed into *E. coli* using 10 μL of the ligation reaction.

3.2.7. Subcloning

In order to subclone DRR1 mutants into different vectors, inserts digested with XhoI and HindIII and purified from an agarose gel after restriction were ligated into the equally digested target vector. Prior to this step, the correct sequence of the insert was confirmed by Sanger sequencing. After transformation into bacteria the success of the subcloning was verified by digestion with XhoI-HindIII and PvuI, respectively.

3.2.8. Measurement of DNA concentration

The concentration of nucleic acids was determined in a spectrophotometer by measuring the absorbance of UV light at 260 nm in a quartz crystal cuvette. Usually the DNA solution was diluted 1:50 in ddH₂O or higher if needed to measure OD₂₆₀ in the range of 0.1 to 1.0. Additionally, the absorbance at 280 nm was measured to check for possible

protein contaminations. At this, the ratio of OD_{260}/OD_{280} was confirmed to be between 1.8 and 2.0.

3.2.9. Sequencing

The coding sequence of successfully cloned plasmids was sequenced by Microsynth AG (Lindau). For this, the DNA was adjusted with ddH₂O to a concentration of 80 ng/ μ L in a final volume of 10 μ L. Primers were added in 20 pmol if needed.

3.3. Cell culture

3.3.1. Culturing of eukaryotic cell lines

All cell lines used in this work were cultured as adherent cells in sterile tissue culture dishes or flasks at 37°C and 5% CO₂ atmosphere in an incubator. High glucose DMEM was used as culture medium supplemented with 10% FCS, 1% sodium pyruvate, and 1% antibiotic-antimycotic (penicillin-streptomycin). The cells were passaged every 3-4 days after reaching a confluency of approximately 90%. For this, the adherent cells were carefully washed with ~10 mL PBS (for an T-75 flask), then detached by incubation with 2 mL trypsin-EDTA for about 5 min at 37°C. Trypsin-EDTA was then inactivated by the addition of 3 mL DMEM. The detached cells were flushed from the surface and transferred to a sterile tube. To remove the trypsin-EDTA the cells were centrifuged (4 min, 1,000 rpm) and resuspended in the appropriate amount of fresh medium for dilution in the desired ratio. Usually, this ratio was between 1:4 and 1:12 depending on the cell type and growth rate. The diluted cells were then placed in a new flask with fresh medium for further cultivation.

3.3.2. Storage of cell lines

For the long-term storage of cell lines, the cell pellet of a confluent T-75 flask was resuspended in 1 mL freezing medium, consisting of DMEM supplemented with 50% FCS and 10% DMSO. The cell suspension was transferred to a cryotube and frozen overnight at -80°C. The cells were placed in a liquid nitrogen tank for long term storage.

In order to take frozen cells into culture, the cells were thawed rapidly by incubation at 37°C, then the freezing medium was removed by centrifugation (4 min, 1,000 rpm) and the cell pellet was resuspended in fresh culture medium. Thereby, the DMSO was removed which might have a cytotoxic effect. The cells were then transferred to a T-75 flask, incubated at 37°C overnight and passaged on the next day.

3.3.3. Coating of glass coverslips/dishes and cell seeding

The adherence of cells to the growth surface can be improved by coating the surface with different substrates. There is a variety possible of substrates all mimicking the natural interactions between the cells and the extracellular matrix (ECM). Different coatings were used in this work including fibronectin, gelatin, laminin and poly-D-lysine. Fibronectin is an ECM glycoprotein mediating adhesion by binding to integrins. Gelatin is derived from the major ECM component collagen and therefore a cheap and easy agent to coat culture flasks. Poly-D-lysine exhibits polycationic properties promoting effective attachment of cells to the growing surface and laminin is the most abundant non-collagen component of the basal lamina. Prior to coating the coverslips were sterilized with pure EtOH, air-dried and washed with PBS. Glass bottom dishes were directly coated. Gelatin, poly-D-lysine and laminin coatings were incubated at 37°C for > 3 h or overnight. Afterwards the coverslips/dishes were washed three times with PBS. Fibronectin was incubated for 45 min at RT without washing the coverslips subsequently. For immunostainings, round 12 mm coverslips were placed in 24-well plates and 10,000 – 20,000 cells were seeded on each coverslip. Transfection was performed 24 h after seeding.

Fibronectin:	0.96 mg/mL stock solution, diluted 1:200 in DMEM.
Gelatin:	0.1% gelatin in ddH ₂ O, autoclaved.
Laminin:	1 mg/mL in Ampuwa ddH ₂ O, diluted 1:1000 in ddH ₂ O prior to use.
Poly-D-lysine:	10 mg/mL in Ampuwa ddH ₂ O, diluted 1:100 in ddH ₂ O prior to use.

3.3.4. Transfection by electroporation

Electric pulses increase the permeability of cell membranes without disrupting its structural integrity. This effect is used to introduce foreign plasmid DNA by diffusion through the small reversible gaps in the membrane (Chu et al., 1987).

For each electroporation the cells of a confluent 10 cm dish (60 cm²) were washed with PBS and resuspended in 400 µL resuspension buffer. The cell suspension was transferred to an electroporation cuvette and the plasmid DNA was added (max. 20 µg per sample). Immediately prior to electroporating the cells, the suspension was carefully mixed by slow vortexing. The optimal electroporation conditions are dependent on the cell type. HEK-293 cells were electroporated with a pulse of $U = 350$ V and $T = 700$ µF. After electroporation the cells were rapidly transferred into a new 10 cm dish with pre-warmed DMEM medium and incubated for 2-3 days.

MgSO ₄ buffer:	1 M MgSO ₄ · 7 H ₂ O, adjust to pH 6.7 with NaOH.
Electroporation buffer:	50 mM K ₂ HPO ₄ · 3 H ₂ O, 20 mM KAc, adjust to pH 7.35 with acetic acid, sterile filtered.
Resuspension buffer:	390 µL electroporation buffer, 10 µL MgSO ₄ buffer for each electroporation (~60 m ² confluent cells).

3.3.5. Transfection with TurboFect

Adherent HeLa cells were transfected with TurboFect Transfection Reagent according to the manufacturer's protocol. TurboFect is a cationic polymer forming compact, stable, positively charged complexes with the negatively charged DNA. Shortly, cells in a 24-well plate seeded on the day before transfection were transfected using 1 µg DNA, 2 µL TurboFect in 100 µL DMEM. In 35-mm dishes 4 µg DNA, 6 µL TurboFect and 400 µL DMEM were used. The DNA was diluted in DMEM, then TurboFect was added, mixed by vortexing and incubated at RT for 15-20 min. The transfection mixture was then added to the cells drop-by-drop. The medium was changed 24 h after transfection.

3.3.6. Transfection with Lipofectamine 2000

As an alternative to TurboFect, adherent HeLa cells were also transfected with Lipofectamine 2000, a transfection reagent based on liposomal complexes. In a 24-well plate, 0.5 µg DNA were diluted in 25 µL DMEM in one tube, and 2 µL Lipofectamine 2000 were diluted in another tube with 25 µL DMEM. After an incubation of 5 min, the first tube was added to the second, thoroughly mixed by vortexing and incubated for another 20 min at RT. Finally, the DNA-lipid complex was added to the cells. The medium was changed after 6 h.

3.4. Primary hippocampal culture

3.4.1. Preparation of primary mice hippocampal neurons

Primary hippocampal neurons were prepared from mice by Dr. Sebastián Giusti, Research Group Dr. Damián Refojo, Max Planck Institute of Psychiatry, Munich (Dotti et al., 1988). DIV0 (day *in vitro*) is defined as the day of preparation. Animals were handled according to the Guide for the Care and Use of Laboratory Animals of Government of Bavaria, Germany.

3.4.2. Culturing of hippocampal neurons

Primary hippocampal neurons were seeded on coverslips (12 mm round) in a 24-well plate in a density of 50,000 cells per coverslip (250 cells/mm²) in 1 mL medium. Previously, coverslips were pre-treated with chloroform for 10 min followed by three washing steps (~10 min each) with absolute ethanol. After sterilization for 2-4 h at 180°C the coverslips were coated with poly-D-lysine (50 µg/mL, >3 h or overnight at 37°C) and laminin (1 µg/mL, > 3 h or overnight at 37°C). Neurobasal A supplemented with 2% B-27 and 0.5 mM GlutaMax was used as a culture medium. The medium was not changed during cultivation at 37°C in the incubator. If needed, little amounts of fresh medium were added to the conditioned medium during transfection of the cells or above DIV10-14.

3.4.3. Transfection with the calciumphosphate method

Transfection of primary hippocampal neurons with the calciumphosphate method was performed on DIV7-14 and analysis was performed on the indicated time points in each experiment (Jiang and Chen, 2006). For four wells, 8 µg of endotoxin-free plasmid DNA were diluted in 37.5 µL Ampuwa ddH₂O (subtracting the volume of the DNA) in a 1.5 mL Eppendorf tube. Then, 12.5 µL of CaCl₂ were added and mixed by fast vortexing. For precipitation, the tube was placed on a vortexer and 50 µL BBS buffer were slowly added to the tube during slow vortexing followed by the addition of 900 µL pre-warmed Neurobasal A medium and fast vortexing. This mixture was incubated at RT for 15 min. The conditioned medium was then withdrawn from the neurons and 250 µL of the calciumphosphate-DNA precipitate were added. To avoid drying of the neurons and minimize exposure to oxygen, each well was processed separately working with two pipettes at a time. The neurons were then placed back in the incubator and incubated with the transfection mix for 1-2 h depending on the age of the neurons. 20-30% of fresh Neurobasal A was added to the conditioned medium which was then filtered sterile to remove any cell debris or contaminations. After incubation, the transfection mix was removed and the neurons were washed well-per-well 8x with warm HBSS working again with two pipettes. Finally 1 mL medium was added and the neurons were incubated at 37°C.

BBS buffer (2x): 50 mM BES, 280 mM NaCl, 1.5 mM Na₂HPO₄,
in Ampuwa ddH₂O, adjust to pH 7.26, sterile filtered,
store at -20°C.

CaCl₂: 1 M CaCl₂ · 2 H₂O, in Ampuwa ddH₂O, sterile filtered,
store at -20°C.

HBSS (1x): for washing, supplement with 3 mL HEPES to adapt pH.

3.5. Proteinbiochemical methods

3.5.1. SDS-Polyacrylamide gel electrophoresis

In order to separate proteins depending on their molecular weight in an electric field a discontinuous SDS-polyacrylamide gel electrophoresis (SDS-PAGE) was used (Fling and Gregerson, 1986). Protein samples were prepared with 1:5 volume of Laemmli sample buffer and heated to 95°C for 5 min. In doing this, proteins were denatured by β -Mercaptoethanol and the anionic detergent SDS included in the sample buffer. SDS further applies a negative charge to the protein in proportion to its molecular weight. The gels were polymerized in a gel caster (Bio-Rad) with a thickness of 1 mm. The resolving gel was poured into the apparatus immediately after the addition of APS and TEMED and covered with a thin layer of isopropanol. After polymerizing for at least 30 min, the isopropanol was removed, the stacking gel was poured on the resolving gel and a comb with 10 or 15 wells was inserted. After polymerization for about 30 min the gel was either directly used or stored for up to week at 4°C wrapped in wet paper towels. For gel electrophoresis the comb was carefully removed under running water and the gel was placed into the electrophoresis apparatus. The buffer chamber was filled with SDS running buffer (1x). The protein samples were loaded on the stacking gel with a syringe (Hamilton) and 5 μ L of peqGOLD Prestained-Protein marker IV were injected into the first well to estimate the molecular weight of the proteins. The electrophoresis was performed at 100 V for 15-20 min to allow the proteins to focus in the stacking gel and enter the resolving gel, then the voltage was increased to 120-150 V for about an hour for separation in the resolving gel. After SDS-PAGE the gels were either stained with Coomassie Brilliant Blue or transferred to a nitrocellulose membrane for Western Blotting.

Stacking gel buffer (4x): 1 M Tris-HCl, pH 6.8.

Resolving gel buffer (4x): 1.5 M Tris-HCl, pH 8.8.

Laemmli sample buffer (5x): 5% SDS, 40% glycin, 160 mM Tris pH 6.8,
5% β -Mercaptoethanol, bromophenol blue.

Laemmli running buffer (10x): 25 mM Tris, 192 mM glycin, 0.5% SDS.

APS: 10% w/v in ddH₂O

10% Resolving gel (2 gels): 4 mL ddH₂O, 3.3 mL Acrylamide/Bis-Solution,
2.5 mL Resolving gel buffer, 0.1 mL 10% SDS,
add 100 μ L APS and 10 μ L TEMED for polymerization.

- 12% Resolving gel (2 gels): 3.3 mL ddH₂O, 4 mL Acrylamide/Bis-Solution, 2.5 mL Resolving gel buffer, 0.1 mL 10% SDS, add 100 µL APS and 10 µL TEMED for polymerization.
- 15% Resolving gel (2 gels): 2.3 mL ddH₂O, 5 mL Acrylamide/Bis-Solution, 2.5 mL Resolving gel buffer, 0.1 mL 10% SDS, add 100 µL APS and 10 µL TEMED for polymerization.
- 3.2% Stacking gel (2 gels): 3.1 mL ddH₂O, 0.55 mL Acrylamide/Bis-Solution, 1.25 mL Stacking gel buffer, 0.05 mL 10% SDS, add 50 µL APS and 7.5 µL TEMED for polymerization.

3.5.2. Colloidal Coomassie staining of PAA gels

Following the electrophoresis the gels were stained with colloidal Coomassie for visualization of all protein bands on the gel. For this, the gel was shortly washed in ddH₂O after SDS-PAGE to remove SDS and fixed overnight in Colloidal fix (1x). On the next day, the gel was washed with ddH₂O (3 x 10 min) and equilibrated in 10 mL Colloidal stain (1x) for 1 h. Finally, about 10 mg Brilliant blue G was added and the incubation was continued overnight or up to three days for staining. Prior to scanning the gel was washed with ddH₂O. All incubation steps were performed on a shaker.

Colloidal fix (3x): 90% EtOH, 6% Phosphoric acid 85%, in ddH₂O.

Colloidal stain (1x): 17% Ammonium sulfate, 2% Phosphoric acid 85%, 34% methanol, in ddH₂O.

3.5.3. Western Blot

Prior to Western blotting the proteins separated by SDS-PAGE were transferred from the polyacrylamide gel to a nitrocellulose membrane in a Wetblot. The transfer sandwich was carefully assembled avoiding the formation of air bubbles with the following components from cathode to anode: sponge (for isolation), 3x Whatman filter paper, gel, membrane, 3x Whatman paper, and sponge. All components were previously equilibrated in Wetblot buffer (1x) for 5-10 min. The entire stack was placed in the blotting chamber filled with Wetblot buffer (1x) and a cooling pack. The transfer was performed in the cold room at 100 V for 90 min.

In order to rapidly control the effectiveness of protein transfer from the gel to the nitrocellulose membrane, the membrane was stained with Ponceau S by incubation in the staining solution for about 5 min. Ponceau S is an azo dye reversibly binding to the

positively charged amino groups of the proteins. The proteins were destained with ddH₂O and the dye was removed by washing with TBS-T.

A Western Blot was performed for immunological detection of specific proteins. Usually two antibodies were used for this: the primary antibody binds specifically to the target protein, while the secondary antibody recognizes the constant region of the first and is coupled to the horseradish peroxidase (HRP) of fluorescent dyes. Some primary antibodies like anti-FLAG are already HRP-conjugated making the secondary antibody dispensable. The detection is based on the chemiluminescent reaction catalyzed by the HRP at which the substrate luminol is oxidized in the presence of H₂O₂ resulting in blue light emission or on the excitation of the fluorescent dye. These light emissions were detected in the ChemiDoc Imaging System (Bio-Rad, München). Since the membrane exerts a high capability of binding protein, all non-specific binding sites were blocked by incubation in 5% milk powder in TBS-T (1x) for 1 h. Finally, the membrane was incubated with the primary antibody (1:500 – 1:5,000 in TBS-T with 2% milk, overnight at 4°C) followed by the secondary (1:10,000 in TBS-T with 2% milk, 2-3 h at RT). The Western Blot was developed according to the manufacturer of the luminescence reagents (Immobilon Western Chemiluminescent HRP Substrate, Merck Millipore, Darmstadt) if HRP was used. After each antibody incubation and prior to the detection the membrane was washed three times for 10 min with TBS-T. All incubation steps were performed on a shaker.

Wetblot buffer (10x):	480 mM Tris, 390 mM glycine, 0.375% SDS.
Wetblot buffer (1x):	10% Wetblot buffer (10x), 20% methanol.
Ponceau solution:	2% Ponceau S, 30% trichloroacetic acid, 30% sulfosalicylic acid, diluted 1:10 in ddH ₂ O.
TBS-T (1x):	150 mM NaCl, 10 mM Tris-HCl, pH 7.6, 0.1% Tween 20.

3.5.4. Measurement of protein concentration

To measure the protein concentration of e.g. cell lysates the commercially available BCA Protein Assay Kit (Thermo Scientific, Rockford, USA) was used according to the manufacturer's protocol. The reaction is based on the biuret reaction at which Cu²⁺ is reduced to Cu⁺ in the presence of protein in an alkaline solution followed by a highly specific detection for Cu⁺ with bicinchoninic acid (BCA). BCA reacts in a 1:1 stoichiometry with Cu⁺ ions to a violet product with an absorbance maximum at 562 nm allowing for the sensitive quantification of the protein amount in the solution. Shortly, the samples were usually diluted 1:10 in ddH₂O prior to the BCA reaction and then pipetted into a 96-microtiter plate in triplicates. The BCA reagent was then added according to the

manufacturer and incubated at 60°C for 20-30 min. The absorbance was measured at 550 nm in a microplate reader. The protein concentration was calculated by comparison with a BSA calibration curve.

3.5.5. Recombinant protein expression and purification

Recombinant DRR1 proteins were expressed and purified as MBP fusion proteins in order to enhance stability and solubility (Fox and Waugh, 2003). DRR1 and the cloned mutants were subcloned into pMAL, an expression vector that leads to the expression of proteins attached to MBP at the N-terminus. Although MBP can be removed by cleavage with the specific protease factor Xa after purification, this resulted in denaturation of DRR1 which is why all further experiments were performed with MBP-fusion proteins. All experiments with recombinant proteins were performed with buffer only and MBP as controls, respectively. Since there were no detectable differences between buffer and MBP, the latter is shown in all figures as control. For expression of MBP-fusion proteins a 100 mL culture of BL21(DE3)pLysS *E. coli* bacteria was incubated overnight at 37°C in LB/Amp with 0.2% glucose. The following day 50 mL of the culture were transferred to 500 mL fresh medium and incubated at 37°C until the OD₅₉₅ was between 0.4 and 0.6. The protein expression was induced by 0.3 mM IPTG (final concentration) and incubation at 37°C for 2 h. Before and after induction, 1 mL of the bacterial suspension was centrifuged (4,000 rpm, 10 min) and resuspended in 50 µL and 100 µL 2x Laemmli sample buffer, respectively. After induction, the cells were centrifuged (4,000 rpm, 20 min, 4°C). The bacterial pellets were lysed by the freeze-thaw method in a dry-ice ethanol bath and then resuspended in 15 mL lysis buffer, incubated on ice 1 h and sonicated. Finally, the soluble proteins were separated from the cell debris by centrifugation (48,400x g, 45 min, 4°C). From this point on, all following steps were done at 4°C to avoid denaturation or aggregation of the protein. Prior to loading on the affinity column the cleared lysates were filtered through a 0.8 µm and a 0.22 µm filter. Protein purification was performed using the ÄKTApurifier system (GE Healthcare, Freiburg) with affinity chromatography (MBPTrap HP, 1 mL, GE Healthcare) followed by gel filtration (Superdex200 10/300 GL, GE Healthcare). All buffers for FPLC were filtered through a 0.22 µm filter and degassed. Cleared and filtered bacterial lysates were loaded on equilibrated MBPTrap at a constant flowrate of 0.5 mL/min with 15 mL binding buffer, washed by 5 mL binding buffer and eluted by 10 mL elution buffer. Samples containing recombinant protein as controlled by SDS-PAGE and Coomassie staining were pooled and concentrated with Vivaspin 20, molecular weight cut off (MWCO) 30 kDa. Then the buffer was exchanged to superdex running buffer. Gel filtration was performed on a Superdex200 10/300 GL column (GE Healthcare) at a constant flowrate of 0.5 mL/min and samples were analyzed subsequently on SDS-PAGE. Samples containing recombinant protein were pooled. The concentration was measured by UV absorbance at 280 nm and by densitometry with a protein standard

on colloidal Coomassie stained SDS-PAGE. Purified proteins were aliquoted and frozen in liquid N₂. Freshly thawed aliquots of recombinant protein were used for all experiments.

IPTG:	1 M, diluted in ddH ₂ O.
PMSF:	200 mM in EtOH
Lysis buffer:	BB with PI (1:100), PMSF (1 mM), lysozyme (1 mg/mL).
Binding buffer (BB):	20 mM Tris-HCl pH 7.4, 200 mM NaCl, 1 mM EDTA, 1 mM DTT.
Elution buffer (EB):	10 mM maltose in CB.
Superdex running buffer:	20 mM Tris-HCl pH 7.4, 150 mM NaCl, 1 mM DTT

3.5.6. Determination of protein concentration

In order to determine protein concentration and to check the protein purity, an SDS-PAGE was done loading 1, 2, 5, and 10 μ L of protein, and a protein standard of 1, 2, and 5 μ g (protein on gel) BSA as a reference. In addition, a BCA test was performed with 1:5 dilutions (see 3.4.5) and the absorbance of UV light at 260 nm of appropriate dilutions was measured. However, the latter two methods measure the total protein concentration including contaminations. Thus, the concentration of the MBP-fusion proteins was expected to be slightly lower depending on the purity of the sample.

3.6. Cellular assays

3.6.1. Dual-luciferase reporter gene assay

For dual-luciferase reporter gene assays 10,000 HEK-293 cells/well were seeded in 96-well plates. The SRF reporter plasmid 3DA.luc and mDia1-dDAD plasmids were kind gifts from Robert Grosse (Universität Marburg, Germany). Simian virus 40 promoter-driven non-secretory gaussia luciferase expression vector (10 ng per well in a 96-well plate) was cotransfected with SRF reporter (25 ng) to correct for transfection efficiency. The indicated test plasmids (150 ng) were also cotransfected. Twenty-four hours after transfection, SRF activity was stimulated with 20% FBS or inhibited (0.5% FBS) for 16-18 h until measurement. To measure reporter gene activity, cells were lysed in 50 μ L passive lysis buffer for 30 min at RT under constant shaking. Firefly and gaussia luciferase activities were measured in the same aliquot using the TriStar LB941 Luminometer (Berthold Technologies, Bad Wildbad). Firefly activity was measured first by adding

50 μ L firefly substrate solution to 10 μ L lysate in white microtiter plates. By adding 50 μ L gaussia substrate solution the firefly reaction was quenched and gaussia luminescence was measured after a 5 s delay. Firefly activity data represent the ratio of background (i.e. untransfected) corrected firefly to gaussia luminescence values. To compare different experiments, the SRF activity in the serum-stimulated control with pRK5 vector was set to 1. To verify protein expression, triplicate lysates were pooled, briefly sonicated and analyzed by SDS-PAGE followed by Western Blot.

Passive lysis buffer: 0.2% Triton X-100, 100 mM K_2HPO_4/KH_2PO_4 pH 7.8

Firefly substrate solution: 3 mM $MgCl_2$, 2.4 mM ATP, 120 mM D-Luciferin

Gaussia substrate solution: 1.1 M NaCl, 2.2 mM Na_2EDTA , 0.22 M K_2HPO_4/KH_2PO_4 , pH 5.1, 0.44 mg/mL BSA, Coelenterazine 3 μ g/mL

3.6.2. Co-immunoprecipitation with GFP-Trap

For co-immunoprecipitation, agarose beads coupled to GFP-Trap (ChromoTek, Planegg-Martinsried) were used. GFP-Trap is based on a single-domain antibody fragment derived from alpaca, a so-called nanobody, specifically binding to GFP or GFP-fusion proteins. HEK-293 cells were transfected by electroporation with 15 μ g plasmid per sample of ~ 60 cm² cells using plasmids expressing EGFP-fusion proteins. Lysis was performed with 200 μ L ice-cold lysis buffer. The extract was incubated for 1 h on ice, diluted with 700 μ L dilution buffer and centrifuged for 10 min at 13,000 rpm to remove cell debris. Each lysate was incubated with 25 μ L GFP-Trap agarose beads for 1 h at 4°C¹. Beads were previously equilibrated in wash buffer as recommended by the manufacturer (centrifugation for 2 min at 2,500x g, 4°C). Then, the beads were washed two times with 1 mL wash buffer and samples were eluted by incubation for 10 min at 95°C in 50 μ L Laemmli sample buffer (1x). The beads were then collected by centrifugation and eluates were transferred to a new tube. Lysates and eluates were analyzed by SDS-PAGE and Western blot. To analyze and compare actin binding, background corrected IP and Co-IP bands were quantified. The co-precipitated actin signal (if present) in the EGFP control was defined as background and subtracted from all other signals. Next, the ratio of co-precipitated actin and the corresponding precipitated protein was formed and defined as “actin binding”. The “mean actin binding” for each experiment using the same mutants (wt, dN, dC, dM and M) was calculated and actin binding of each mutant was normalized to the mean actin binding of the respective experiment.

¹ The incubation time was increased as recommended by the manufacturer, as GFP-Trap has a slightly lower affinity to C-terminal fusions than N-terminal fusion.

Lysis buffer: 10 mM Tris-HCl, pH 7.5, 150 mM NaCl, 0.5 mM EDTA, 0.5% NP-40, 1x PI cocktail (freshly added)

Dilution & Wash buffer: 10 mM Tris-HCl, pH 7.5, 150 mM NaCl, 0.5 mM EDTA, 1x PI cocktail (freshly added)

3.6.3. Chemical crosslinking

Chemical crosslinking of HEK-293 cells transfected with DRR1 was performed with the membrane-permeable crosslinkers DSS, DSG and BMB. DSS (Disuccinimidyl suberate) and DSG (Disuccinimidyl glutarate) are NHS esters reacting with primary amines leading to crosslinking of lysine residues. DSS has a spacer arm of 11.4 Å, while DSG is slightly shorter with 7.7 Å. BMB (1,4-Bismaleimidobutane) is a maleimide with a spacer arm length of 10.9 Å generating chemical bonds between sulfhydryl groups, i.e. cysteine residues. HEK-293 cells were transfected with pRK5-DRR1 plasmids by electroporation and incubated for 2 days at 37°C. Cells were then detached by trypsinization and washed with PBS. Each 10 cm dish transfected with one plasmid was divided into two new tubes and resuspended in 5 mL of crosslinker conjugation buffer. Controls were performed by replacing the crosslinker with DMSO in the conjugation buffer. Cells were incubated on a shaker with DSS for 30 min at RT, then 2 h at 4°C, with DSG and BMB for 2 h at 4°C. After crosslinking, samples were quenched by incubation for 30 min at 4°C in 1 mL quenching buffer per sample. Finally, the cells were collected by centrifugation and lysed by resuspension in SDS-lysis buffer, short sonication and heating to 95°C for 5 min. Protein concentration was determined with the BCA method and 5-10 µg protein were loaded on SDS-PAGE for analysis in Western Blot.

DSS stock (300x): 22.5 mM in DMSO (1 microtube), working conc. 75 µM

DSG stock (100x): 200 mM in DMSO, working conc. 2 mM

BMB stock (100x): 20 mM BMB in DMSO, working conc. 0.2 mM

DSS/DSG conjugation buffer: DSS/DSG in PBS

DSS/DSG quenching buffer: 50 mM Tris-HCl pH 7.5

BMB conjugation buffer: 1:100 volume BMB stock, 5 mM EDTA in PBS

BMB quenching buffer: 10 mM DTT in PBS

SDS-lysis buffer (3x): 62.5 mM Tris-HCl pH 7.4, 10% sucrose, 2% SDS, 1x PI cocktail (freshly added)

3.6.4. Cell spreading

In contrast to the active process of cellular migration, adhesion and early spreading of a cell in suspension to a substrate are more passive processes influenced by substrate stiffness and density, integrin-receptor diffusion to the adhesive patch, and mechanical properties of the cell (Cuvelier et al., 2007; Li et al., 2014; Yauch et al., 1997). Later stages of cell spreading include active processes like actin polymerization and myosin contraction (Chamaraux et al., 2005). For analysis of cell spreading with DRR1 overexpression, HeLa cells in a 6-well-plate were transfected with EGFP fusion proteins using TurboFect as described above. On the next day, cells were harvested with PBS, diluted to about 20,000 cells/mL and replated on 12 mm round coverslips coated with 50 μ g/mL fibronectin placed in 24-well-plates (1 mL/well). For cell spreading analysis with antidepressants, HeLa cells were trypsinized from the culture dish and the medium was changed to antidepressant-containing medium immediately prior to replating on fibronectin. After 30 min spreading at 37°C, cells were washed once with PBS and fixed in 4% paraformaldehyde (PFA) for 20 min at RT. Cells were then stained with Alexa Fluor 546-phalloidin and mounted on glass slides as described in chapter 3.7.5. Images were captured with the fluorescence (20x or 40x objective) or confocal microscope (10x/0.40 NA or 40x/1.15 NA objective). The cell size was determined from up to 10 randomly selected fields with about 100-200 cells total using the open-access image processor *ImageJ*. Shortly, the images were scaled, the phalloidin-channel was thresholded (lower threshold level 250, upper threshold level 4095) and adjacent cells were separated by the “Watershed” algorithm. Correct cell separation was double-checked manually. By means of the thresholded phalloidin-channel, the mean gray value in the EGFP channel was measured and the cell size in the original phalloidin-channel using the “Analyze Particles” algorithm. Cells with a mean gray value of >500 were defined as transfected. In order to compare different conditions and experiments, the mean area of transfected cells was normalized with the mean area of untransfected cells in the same condition. In experiments with DRR1, the control refers to the EGFP-transfected sample, in experiments with antidepressants it refers to untransfected cells.

3.6.5. Cellular fractionation

In order to analyze nuclear and cytoplasmic localization of DRR1, HEK-293 cells were transfected with pRK5-DRR1 plasmids and after two days incubation a cytosolic-nuclear cell fractionation was performed. For this, cells were trypsinized, washed with PBS and resuspended in 250 μ L hypotonic lysis buffer per 10 cm dish. After an incubation of 10 min on ice, cells were briefly vortexed and disruption of the outer cell membrane was analyzed in the microscope. The samples were centrifuged (6,500 rpm, 30 s, 4°C) and the supernatant containing cytosolic proteins was transferred to a new tube. The pellet was

carefully washed three times with 500 μ L hypotonic lysis buffer and finally the nuclei were lysed by incubating in 200 μ L SDS-lysis buffer (1x) 5 min at 95°C and short sonication. After centrifugation (full speed, 1 min) the supernatant was transferred to a new tube. Concentration of cytosolic and nuclear fractions was determined by BCA and the samples were analyzed by SDS-PAGE and Western Blot. About 7-10 μ g cytosolic fraction and the same volume of the corresponding nuclear fraction were loaded.

Hypotonic lysis buffer: 10 mM HEPES pH 7.9, 10 mM KCl, 0.5 mM EDTA,
 0.1% NP-40, 10% glycerol, 1 mM DTT and PI (freshly
 added)

SDS-lysis buffer (3x): 62.5 mM Tris-HCl pH 7.4, 10% sucrose, 2% SDS,
 1x PI cocktail (freshly added)

3.6.6. 2D-Migration assay

For 2D-Migration assays (also known as Wound Healing or Scratch assay) 30-50.000 HeLa cells were seeded in each well of a 24-well plate and cultured to confluency. The cellular monolayer was scratched with a P10 pipette tip mimicking a two-dimensional wound. After the scratch, the medium was changed to fresh medium containing antidepressants or the solvent (50% EtOH, 5 mM HCl) in the same volume as a control. Cell debris from the scratch was also removed with this medium change. The scratch was imaged after the medium change ($t = 0$) and after 24 h at 37°C with a bright field microscope (4x or 10x objective). Markings were made at the bottom of the well to image the same field of view each time. In order to quantify the migrated distance, the area of the scratch at $t = 0$ and 24 h were measured in *ImageJ*. The difference of the area at $t = 0$ with the area at 24 h was normalized to the 0 h area to compare different conditions and experiments.

3.6.7. Fluorescence recovery after photobleaching (FRAP)

HeLa cells were seeded on 50 μ g/mL fibronectin-coated 35 mm glass dishes (Greiner Bio One, Germany, 50,000 cells/dish). On the day after cell seeding, cells were cotransfected with GFP-Actin (1 μ g) and pRK5 plasmids expressing DRR1 (or empty vector as a control, 3 μ g) using TurboFect. The medium was changed 24 h post transfection. Time-lapse images were acquired in the confocal microscope (20x/0.8 NA objective, 5x zoom, C.A. 200 μ m, LSM FV-1000, 2% laser power) with 2 sec intervals for 5 min. Five frames were imaged pre-bleach. Bleaching was performed with the circular “TurboTool” for 1000 msec at 100% 488-laser power at an image resolution of 320x320 px. Quantification of the acquired images was performed in *ImageJ*, by selecting the bleached area in frame 6

with the Wand tool (“legacy”, “tolerance” = 150), fitting a circle (ROI 1), and measuring the mean gray intensity. An equally sized area within the cell (ROI 2) was used to normalize the fluorescence intensity in each frame. The mean intensity of the first frame was set to 1 in order to compare different cells and conditions. In this experiment, “n” refers to the number of cells analyzed from 2-3 independent experiments.

3.7. Cellular stainings

3.7.1. Fixation, Permeabilization and blocking of cells

For cellular stainings, cells were seeded on coated glass coverslips placed in 24-well-plates and transfected using Lipofectamine 2000 or TurboFect as described above. Cells were washed with PBS and fixed 24 h after transfection with 4% PFA in PBS for 20 min at RT. For permeabilization, the fixed cells were incubated with 0.1% Triton-X 100 (in PBS) for 10 min at RT. The non-ionic detergent Triton X-100 incorporates into the membrane thereby enabling the antibodies to penetrate the cell. After washing the cells again two times with PBS, unspecific binding sites were blocked by incubation in 10% goat serum for 1 h at RT. After blocking, the cells were washed once with PBS.

Triton-X 100: 10% v/v in PBS

3.7.2. Immunostaining

Immunostaining is an antibody-based method to specifically detect a protein target in intact cells. The detection is enabled by a primary antibody which specifically binds to the target and a fluorophore-coupled secondary antibody binding to the first one. By this, several targets can be simultaneously stained in one cell thereby allowing visualization of the sub-cellular localization of the target or potential interaction partners by colocalization. Primary antibodies were diluted 1:200 to 1:500 in 0.1% Triton X-100 in PBS and incubated overnight at 4°C. Secondary antibodies were added to the samples after 3x washing with PBS (10 min each) diluted 1:500 in 0.1% Triton X-100 in PBS and incubated for 2-3 h at RT. During this incubation and all following steps the samples were protected from light to avoid bleaching.

3.7.3. F-actin staining with phalloidin

Phallotoxins from the mushroom *Amanita phalloides* specifically bind to filamentous actin and therefore can be used for staining F-actin in fixed cells. For this, cells were

incubated with 165 nM Alexa Fluor 546-phalloidin in PBS for 20 min at RT. Subsequently the cells were 2x washed with PBS.

3.7.4. DAPI staining of nuclei

DAPI (4'-6-Diamidino-2-Phenylindol) is a fluorescent dye used to stain DNA as it incorporates into the minor grooves of AT-rich sequences. The DAPI stock solution was diluted 1:10,000 in PBS to a final concentration of 1 $\mu\text{g}/\text{mL}$. The cells were incubated for 15 min at RT with DAPI staining (in the dark) and then washed three

DAPI stock: 10 mg/mL in ddH₂O

3.7.5. Storage of stained cells

Stained coverslips were mounted onto SUPER FROST microscope slides (Fisher Scientific, Schwerte) using a drop of approximately 10 μL ProLong Gold Antifade Medium. Mounted coverslips were dried overnight and slides were stored in the dark at 4°C or -20°C. Usually, imaging was performed very soon after mounting in order to avoid quality loss of the staining.

3.7.6. Colocalization analysis

Images for colocalization analysis were taken with the 40x/1.15 NA objective, 3x zoom, and a pinhole of 200 μm . According to the “Nyquist Calculator” of the Scientific Volume Imaging Website (<http://www.svi.nl/>), Nyquist sampling of 60/60/214 nm (x/y/z plane) and a point spread function (PSF) of 4.25 nm were calculated using the Alexa Fluor 546-phalloidin channel for excitation/emission wavelengths. Using these parameters, colocalization analysis was performed in *ImageJ* with the plugin “Coloc 2”. ROIs containing one cell were generated by thresholding the DRR1 channel (lower limit: 300, upper limit: 4095 for a 16-bit image) and selecting individual cells with the “wand” tool. Pearson’s correlation coefficient R and Costes p value were calculated using 100 Costes Randomizations. Only R values with a corresponding Costes p of 1.0 were used. For each condition, 5-15 randomly selected cells from two independent experiments were analyzed.

3.7.7. Quantification of mean cellular F-actin content

Quantification of mean cellular F-actin content was performed in *ImageJ*. Shortly, the images were scaled, the phalloidin channel was thresholded (lower threshold level 150, upper threshold level 4095 for 16-bit images) and adjacent cells were separated by the “Watershed” algorithm. Correct cell separation was double-checked manually. By means of

the thresholded phalloidin channel, the mean gray value in the DRR1 channel was measured, while the cell size was measured in the thresholded phalloidin channel using the “Analyze Particles” algorithm. Cells with a mean gray value of >500 were defined as transfected. For each image, the mean gray value of F-actin in transfected cells was normalized to the mean value of all untransfected cells in the corresponding image in order to compare different images, conditions and experiments. The control refers to the mean cellular F-actin of untransfected cells and then set to 1.

3.8. *In vitro* actin assays

3.8.1. Preparation of purified G-actin from tissue

α -G-actin was obtained from rabbit skeletal muscle actin and labeled with pyrene by technicians in the lab of Prof. Dr. Andreas R. Bausch, Technische Universität München, as previously described (Cooper et al., 1983; Schmoller et al., 2011). All *in vitro* actin experiments except the F-actin co-sedimentation were performed in the lab of Prof. Dr. Andreas R. Bausch. β -Actin from human platelets was prepared and used according to the manufacturer’s protocol (Cytoskeleton, Inc., Denver, USA). In all experiments, “R” refers to the molar ratio of DRR1 recombinant protein or antidepressant to actin. G-actin was stored in G-buffer and the polymerization was induced in all experiments by addition of 1:10 volume of F-buffer (10x) and 1 mM ATP. Experiments were performed under reducing conditions with 1 mM DTT.

G-buffer: 2 mM Tris-HCl pH 8.0, 0.2 mM ATP, 0.2 mM CaCl_2 ,
0.2 mM DTT, 0.005% NaN_3 .

F-buffer (10x): 250 mM Tris-HCl pH 7.4, 250 mM KCl, 40 mM MgCl_2 ,
10 mM EGTA.

ATP (100x): 100 mM in ddH_2O .

DTT (100x): 100 mM in ddH_2O .

3.8.2. Pyrene-actin polymerization

The pyrene-actin polymerization assay is a quick method to analyze the function of a protein as an effector of actin polymerization and/or depolymerization. Fluorescence of pyrene-actin is enhanced two to twenty fold by the association of actin monomers into the polymer form (Kouyama and Mihashi, 1981) and can be measured by excitation at 365 nm and emission at 407 nm. Actin polymerization was monitored by the increase in

fluorescence of 20% pyrene-labeled actin at 407 nm (excitation at 365 nm) in a fluorescence spectrometer (Jasco FP-8500, Gross-Umstadt). The final concentration of actin in the reaction was 5 μM (1 μM pyrene-actin). Antidepressants or DRR1 proteins were added to G-actin in a constant volume and polymerization was induced by the addition of 1:10 volume of F-buffer (10x). The polymerization was monitored for 1-1.5 h at 21°C with a cycle interval of 5.5 s. In experiments with antidepressants, the control was performed with the solvent 50% EtOH/5 mM HCl. The solvent itself did not affect actin polymerization (Supplementary Figure 1).

3.8.3. Actin-filament elongation and nucleation assay

For visualization of single filament polymerization in the confocal microscope samples containing F-buffer (1x) and antidepressants or recombinant proteins (in a constant volume) were prepared. In experiments with antidepressants, the control was performed with the solvent 50% EtOH/5 mM HCl. The solvent itself did not affect actin polymerization (Supplementary Figure 1). Polymerization was induced by the addition of 1 μM G-actin. The sample was then immediately pipetted into a flow chamber consisting of two coverslips (60x24 mm and 20x20 mm) separated by vacuum grease and placed in the confocal microscope. To avoid unspecific surface interactions casein was added to the samples at 0.15 mg/mL. The larger coverslips were previously cleaned with a plasma cleaner (40-50 s at 4-6 mbar) and N-ethylmaleimide-modified heavy meromyosin (NEM-HMM, 2.7 $\mu\text{g}/\text{mL}$ diluted in F-buffer) was bound to the surface by incubation in the flow chamber for 3-5 min to keep actin filaments close to the surface during live visualization. The time between addition of actin to the sample and initiation of the visualization was 2 min. Images in the confocal microscope were taken with a 63x/1.4 NA oil immersion objective and 5x optical zoom. Time-lapse images of polymerization were acquired for 10 min every 3 s at a scan rate of 400 Hz.

The image analysis for single filament elongation and nucleation rate was performed with *ImageJ*. In all images the background was subtracted (rolling ball radius: 10 px, with sliding paraboloid algorithm) and subsequently brightness and contrast was adjusted automatically to the last image of polymerization and applied to all slices in the stack. A segmented line was drawn along the filament and plotted time versus filament length (i.e. fluorescence intensity) using the plugin “Multiple Kymograph”. The graph shows time (i.e. frames) on the Y-axis and filament length on the X-axis, both displayed in μm . The obtained data in μm were recalculated to actin monomers (1 μm filament contains 370 monomers, i.e. the length increase per monomer is 2.7 nm) and time in s (using the total number of frames and the frame interval of 3 s). The slope of this linear graph corresponds

to the filament elongation rate at the barbed end² and was about 12 actin monomers per second for the controls (range from 9 to 14 actin monomers/s, containing superdex buffer or MBP recombinant protein) depending on the actin preparation. This is in accordance to values described in the literature for ATP-actin at similar buffer conditions (Pollard, 1986). The filament elongation rate of the control was set to 100% in order to compare different experiments. For DRR1 experiments, ten filaments from three independent experiments with different actin preparations were measured for each condition.

For nucleation analysis, filaments in 4-8 frames with 30 s intervals (during the first 5 min of polymerization) were counted manually in *ImageJ* from 3 to 5 independent experiments, respectively. The number of filaments was plotted versus time of polymerization and the slope of the resulting linear graph was defined as relative nucleation rate. The control was set to 1.

3.8.4. Actin networks

For visualization of *in vitro* actin networks, samples were prepared with 4 μM actin and recombinant proteins in a constant volume at 2 μM final concentration ($R = 0.5$, DRR1 wt also in $R = 0.1$ and 0.25) or antidepressants in different concentrations at constant volume (from different stock solutions). The control was performed with the solvent 50% EtOH/5 mM HCl. The solvent itself did not affect actin polymerization (Supplementary Figure 1). To avoid unspecific surface interactions, casein was added to the samples in 0.15 mg/mL. Actin filaments or bundles were visualized by addition of Alexa Fluor 488-phalloidin (0.08 μM) to the sample. The polymerization was induced by the addition of 1:10 volume of F-buffer (10x) and the samples were immediately placed into a flow chamber. After sealing the flow chamber with vacuum grease, the samples were polymerized at RT for 1.5 – 2 h protected from light. Polymerized networks were then visualized at steady state in the confocal microscope (63x/1.4 NA oil immersion objective, 1x or 3x optical zoom). Z-stacks of each sample were taken with a 10 μm depth and slices with 0.38 μm step size. Maximum projections of the stacks were made in *ImageJ*, the background was subtracted (rolling ball radius 60 px) and brightness and contrast were adjusted automatically.

3.8.5. Rheology

Actin polymerization and viscoelastic properties of the actin network were analyzed by Rheology in a stress-controlled macrorheometer (Physica MCR301, Anton Paar, Graz, Austria). A sample of 470 μL was prepared with 10 μM actin and different concentrations

² Barbed and pointed ends could be easily distinguished in the graph resulting from the *Fiji* plug-in, as the elongation rate, i.e. the slope of fluorescence intensity, is much lower at the pointed end.

of antidepressants. The control was performed with the solvent 50% EtOH/5 mM HCl. Immediately after initiation of polymerization (addition of F-buffer) approximately 450 μL of the sample were loaded and polymerized on the rheometer using a 50 mm plate geometry with 160 μm plate separation. The polymerization was followed for 180 min by recording the elastic modulus G' at 0.5 Hz applying small torques (0.5 μNm) to ensure a linear response. Then, G' of the polymerized network was analyzed in a frequency scan of 0.01 from 10.0 Hz (7 points per decade, 5% strain). The non-linear response curve was measured at a shear rate of 0.125 per second for 40 s. All measurements were performed at 21°C.

3.8.6. F-Actin co-sedimentation

Polymerization of 1 μM G-Actin was induced by the addition of 1:10 volume of F-buffer (10x) for 1 h at RT. Freshly thawed recombinant DRR1 proteins were added at 0.5 μM to preformed F-actin ($R = 0.5$) and incubated on ice for 30 min to allow proteins to bind to F-actin. The samples of 100 μL total volume were then centrifuged at 150,000x g for 1 h at 21°C in an ultracentrifuge. A total protein sample was taken prior to centrifugation (“T” = total protein) and after centrifugation supernatant and pellet samples (“S” = supernatant, “P” = pellet). Supernatant samples contain G-actin and not sedimented protein, while F-actin and F-actin binding proteins are found in the pellet. All samples were loaded on SDS-PAGE, stained with colloidal Coomassie and subsequently analyzed by densitometry. Since the pellet fractions could be contaminated after removal of the supernatant, the fraction of co-sedimented protein was calculated by subtraction of the supernatant fraction from the total protein. In addition, each protein was centrifuged alone as a control, i.e. without the presence of F-actin. The amount of protein in the pellet calculated for these samples was defined as the background precipitation of the protein and subtracted from the co-sedimented protein amount. The co-sedimented protein was normalized to the amount of F-actin in the respective sample. This method turned out to be highly reproducible and consistent.

3.9. Statistical analysis

Statistical analysis was performed with the *SigmaPlot 12.5* software. Comparison of two groups was done with a two-tailed *t*-test. A one-way ANOVA with Bonferroni *post hoc* analysis was performed for multi-group comparisons. The level of significance was set at $p < 0.05$. All data is presented as mean + SEM (* $p < 0.05$, ** $p < 0.01$, *** $p < 0.001$). Grubb’s Test was run to identify significant outliers.

4. Results

4.1. Clomipramine impacts on actin dynamics

Three antidepressants were chosen in order to study their impact on actin dynamics: clomipramine (clomi), doxepin (dox), and citalopram (cital). Clomipramine is a tricyclic antidepressant (TCA) and was developed in the early 1960s. Besides major depressive disorder, it is also used to treat obsessive compulsive disorder and panic disorder, among others. Doxepin is another tricyclic antidepressant with a variation in the “classic” TCA chemical structure: it features an oxygen-atom in the tricyclic structure. Finally, citalopram is a representative of the selective-serotonin reuptake inhibitors, a newer and more specific class of antidepressants. Both of the latter are used in treatment of depression and anxiety.

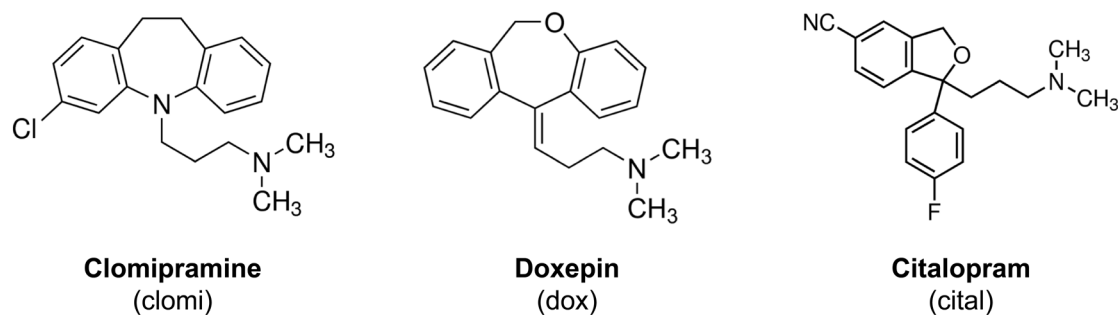


Figure 3. Chemical structures of antidepressants used in this study.

4.1.1. Clomipramine slows down actin polymerization

Inhibition of actin polymerization by clomipramine in the pyrene-assay

A first approach to analyze the impact of any compound or protein on actin dynamics, is the so-called “pyrene-assay”. Being the fundamental step of actin dynamics, the polymerization from monomeric actin to filaments is analyzed in this experiment *in vitro* with purified components. α -Actin is isolated from rabbit skeletal muscle and labeled with

the polycyclic aromatic hydrocarbon pyrene. The increase in pyrene-fluorescence upon polymerization – through stacking of the pyrene molecule in the filament – enables fluorimetric monitoring of the polymerization reaction (Kouyama and Mihashi, 1981).

The antidepressants clomipramine, doxepin, and citalopram were added to 5 μM globular 20% pyrene-labeled actin and the polymerization reaction was initiated by the addition of F-buffer. Actin polymerization was monitored by the increase in fluorescence at 407 nm in a fluorescence spectrometer. Antidepressants were added to the sample in a constant volume from different stock solutions and the control was performed with the equivalent volume of the solvent (50% EtOH/5 mM HCl). The solvent itself did not affect actin polymerization (Supplementary Figure 1).

While there were no effects on actin polymerization by the addition of doxepin and citalopram, clomipramine slowed down actin polymerization. This effect was already observable at a molar ratio of clomi with actin of $R = 2$, but became more pronounced at higher concentrations of $R = 10$ and 20 (Figure 4).

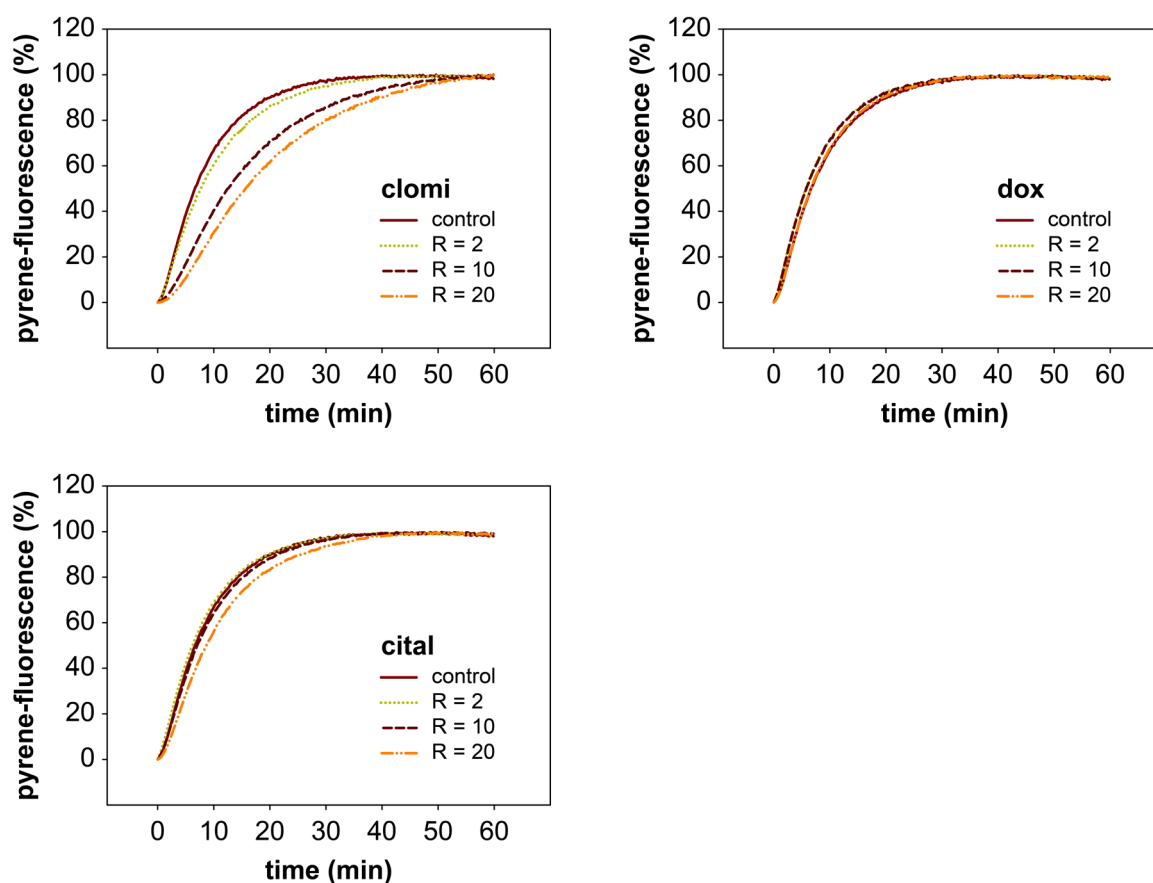


Figure 4. Clomipramine inhibits *in vitro* polymerization of pyrene-labeled actin, while doxepin and citalopram have no effect. 20% Pyrene-labeled actin (5 μM total concentration) was polymerized at RT in the presence of antidepressants and polymerization was monitored by the increase in fluorescence at 407 nm. Representative curves are shown (value at 60 min was set to 100%). „R“ refers to the molar ratio of antidepressant:actin.

Since the predominant cytosolic isoform of actin is β -actin, the pyrene-assay was also performed with β -actin from human platelets, which is commercially available. For this, β -actin was mixed with 20% pyrene-labeled α -actin and the experiment was performed as described above. At $R = 20$, the inhibitory effect of clomipramine on β -actin polymerization was similar to that on α -actin polymerization (Figure 5). At an even higher concentration of $R = 200$, the polymerization was very strongly slowed down with a notable extension of the nucleation phase (initial lag-phase). Nevertheless, it did reach the equilibrium state after approximately 60 min.

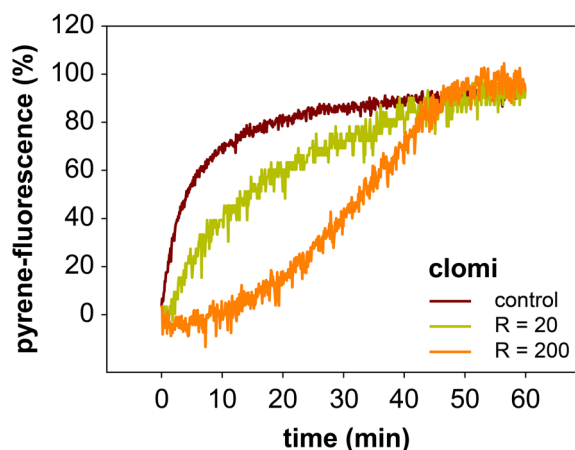


Figure 5. Clomipramine inhibits *in vitro* polymerization of pyrene-labeled β -actin to a similar extent as α -actin. 20% Pyrene-labeled β -actin (5 μ M total concentration) was polymerized at RT in the presence of clomipramine and polymerization was monitored by the increase in fluorescence at 407 nm. Representative curves are shown (value at 60 min was normalized to 100%). „R“ refers to the molar ratio of clomi:actin.

Inhibition of actin polymerization by clomipramine in a label-free assay

In order to verify whether the inhibitory effect of clomipramine on actin polymerization is indeed specific on actin and not unspecific e.g. by quenching pyrene fluorescence, macrorheological measurements were performed with label-free actin. Rheometry is another method to monitor actin polymerization by measuring the viscoelastic properties of the actin network. The polymerization takes place between the base of the rheometer and a plate and is started at the beginning of the measurement. During polymerization small torques of 0.5 μ Nm are applied to the sample. The elastic response of the network to the torques, monitored through the elastic modulus G' , increases with the progressing polymerization state of the sample. A diagram similar to the pyrene-assay is the result. Viscoelastic properties of the network are analyzed by measuring G' (and G'') in a frequency range from 0.01 to 10.0 Hz (only G' is shown). At the measured intermediate frequencies, the elastic properties of the entangled actin network are dominant. Finally, the non-linear response of the network to shear stress is monitored at a shear rate of 0.125 per second for 40 s.

Clomipramine was added to the sample at two concentrations ($R = 2$ and 20) and all three aspects were monitored: elastic response during polymerization (Figure 6A), elastic properties of the network over a frequency range at polymerization equilibrium (Figure 6B and C), and non-linear response to deformation, i.e. shear stress (Figure 6D). In order to characterize the stiffness of the network, an apparent plateau modulus G_0 was defined at G' of 0.01 Hz (Figure 6C).

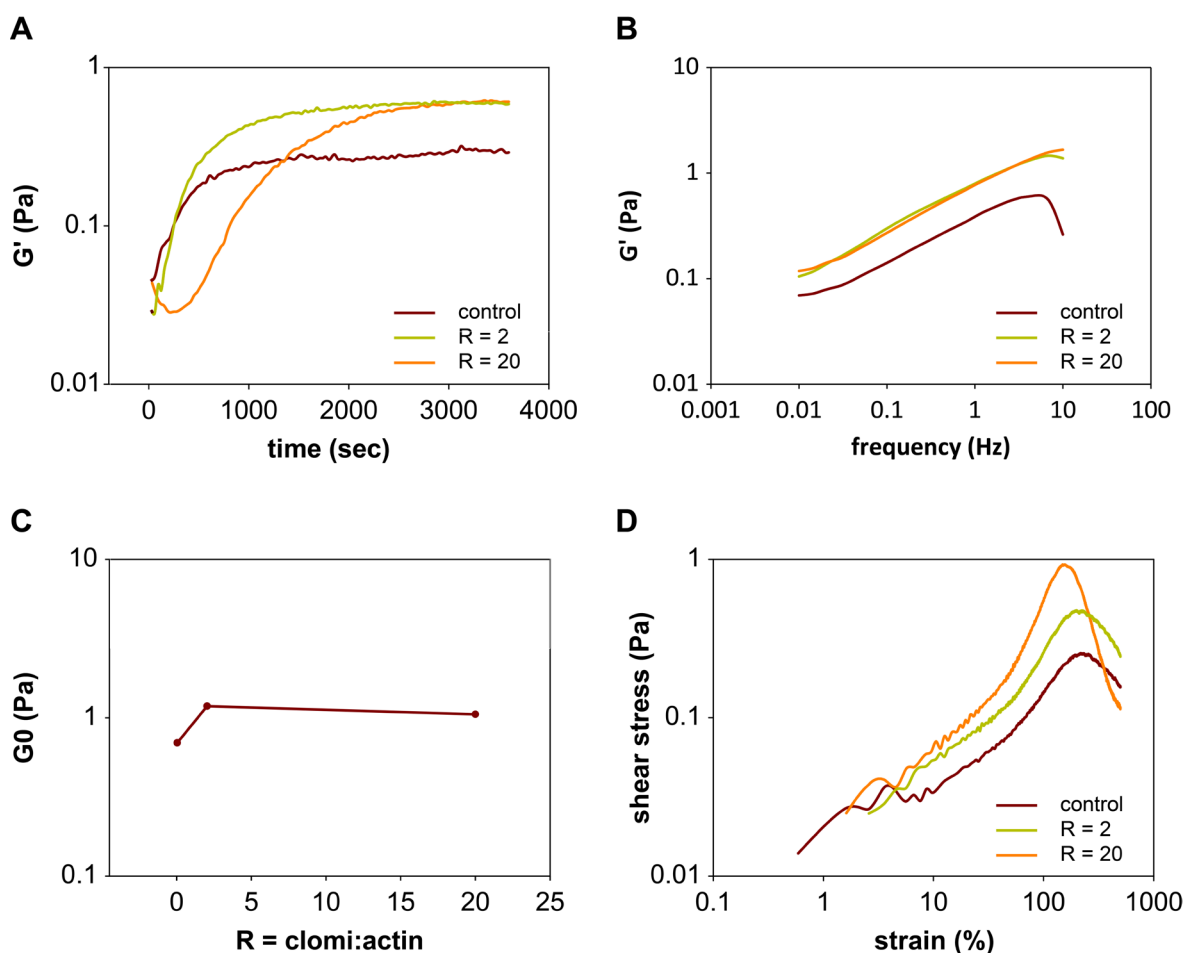


Figure 6. Inhibition of polymerization by clomipramine was confirmed with rheology using label-free actin. Actin ($10 \mu\text{M}$) was polymerized in a rheometer in the presence of clomipramine. (A) Polymerization was monitored by measuring the elastic (storage) modulus G' at a constant frequency of 0.5 Hz at RT with a torque of $0.5 \mu\text{Nm}$. (B) Elastic properties of the actin network were monitored by measuring the elastic (storage) modulus G' at frequencies from 0.01 to 10 Hz with 5% strain. (C) In order to characterize the stiffness of the network, an apparent plateau modulus G_0 was defined at G' of 0.01 Hz. (D) The non-linear response curve was measured at a shear rate of 0.125 per second for 40 s. „R“ refers to the molar ratio of clomi:actin.

The polymerization was slowed down as observed before in the pyrene-assays with a stronger effect at $R = 20$. Interestingly, the initial lag-phase, in which actin nucleation happens, seemed to be extended in comparison to the control, suggesting a potential effect of clomipramine on nucleation. In the frequency scan of G' , the elastic modulus G' seemed to be slightly increased at both concentrations over the entire frequency range. However,

when comparing the plateau modulus G_0 , the differences seem very small and thus insignificant. In the non-linear response to shear stress, clomipramine seems to have slight but likely negligible effect on the hardening of the networks. At the maximum point of the non-linear response curve, the network is disrupted. This point is reached at a lower strain by adding clomipramine, indicating a slight effect on strain hardening.

Clomipramine has no effect on single filament elongation

The pyrene-assay is a quick and easy analysis for effectors of actin dynamics. However, it is not possible to directly assign specific effects like nucleation or capping to the effectors, since the read-out of pyrene-fluorescence corresponds to the whole sample and cannot be attributed to single filaments or even actin monomers. I.e. inhibition of single filament elongation or nucleation cannot be distinguished.

Therefore, polymerization of actin in the presence of clomipramine was visualized in the confocal microscope to enable single filament analysis. Samples containing clomipramine at different concentrations and phalloidin in F-buffer were prepared and polymerization was induced by the addition of 1 μ M G-actin from rabbit skeletal muscle. In this experiment, less actin is used in comparison to the pyrene-assay, in order to enable single filament visualization. Antidepressants were added to the sample in a constant volume from different stock solutions and the control was performed with the equivalent volume of the solvent (50% EtOH/5 mM HCl). The solvent itself did not affect actin polymerization (Supplementary Figure 1). The sample was then immediately pipetted into a flow chamber and placed in the confocal microscope. The coverslips of the flow chamber were previously coated with heavy meromyosin. Thereby, actin filaments are bound to the surface via heavy meromyosin and maintained in one focal plane for visualization. The time-lapse recordings were started two minutes after induction of polymerization in the confocal microscope (63x/1.4 NA objective, 5x zoom) taking an image every 3 s for 10 min (Figure 7A). The image analysis for single filament elongation and nucleation rate was performed with the open-access image processing program *ImageJ*. The single filament elongation rate was quantified as the slope of the plot filament length vs. time. For nucleation analysis, filaments in 4-8 frames with 30 s intervals (during the first 5 min of polymerization) were counted and the slope of the plot number of filaments vs. time was determined as the nucleation rate.

Clomipramine did not affect single filament elongation rate (Figure 7B), but it seems to slightly reduce nucleation of filaments at $R = 50$, i.e. at 50 times excess of clomi (Figure 7C). The effect was not statistically significant though. Such a reduction of the nucleation rate is in accordance with the results from the rheological measurements, indicating, that nucleation might indeed be reduced.

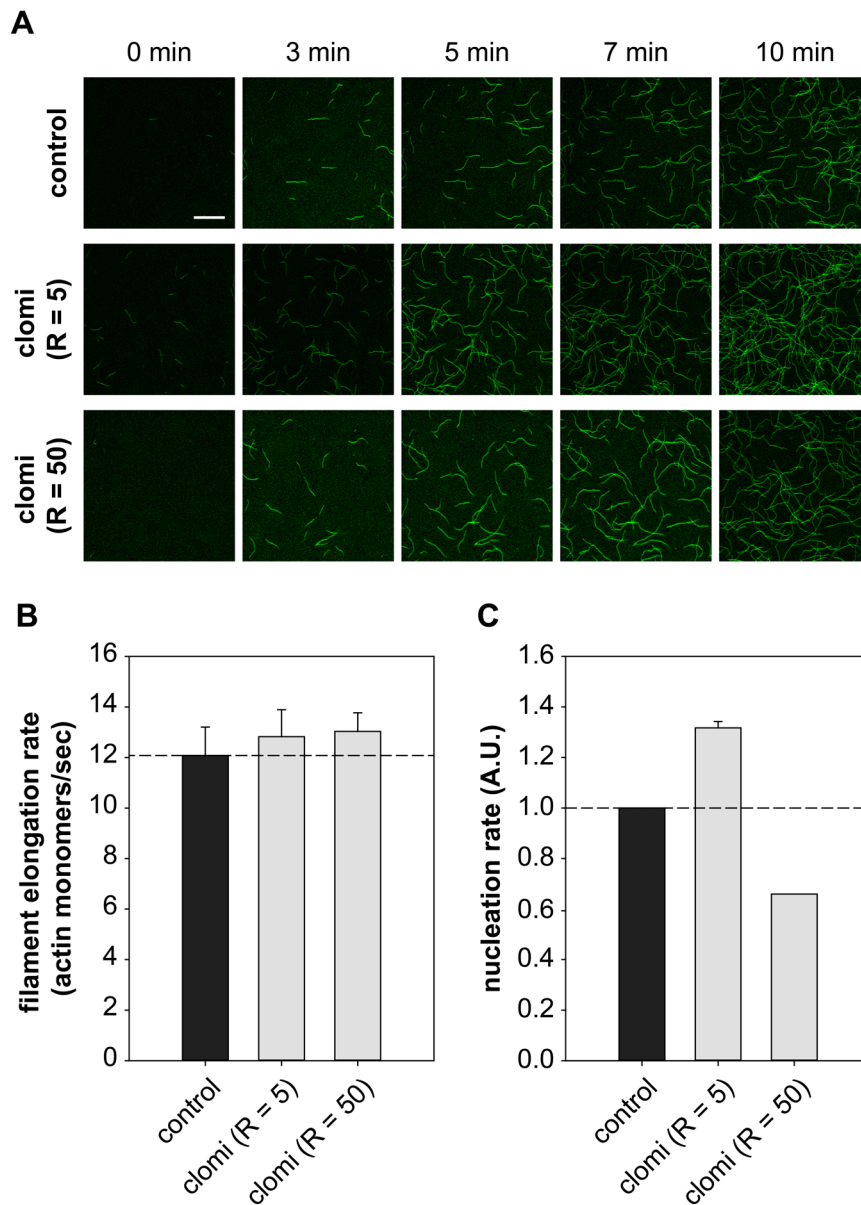


Figure 7. Clomipramine has no effect on single filament elongation while it slightly reduces nucleation. (A) Confocal time-lapse images of *in vitro* actin polymerization (1 μ M actin) in the presence of clomipramine indicate inhibition of single filament elongation at the barbed end. Filaments were visualized by phalloidin-488. Scale bar denotes 10 μ m. „R“ refers to the molar ratio of antidepressant:actin. (B) Quantification of filament elongation rate (control, clomi R = 5 and 50 n = 2, clomi R = 20 n = 1). (C) Nucleation rate defined as the slope of number of filaments per frame quantified in 3-5 frames (with 30 s intervals) normalized to the control (control n = 3, clomi R = 5 n = 2, clomi R = 50 n = 1). Bars represent means + SEM. No significant difference was found in comparison to control. Statistical analysis was performed with one-way ANOVA and Bonferroni *post hoc*.

4.1.2. Actin networks are not affected by antidepressants

In order to further dissect the effect of clomipramine and other antidepressants on actin dynamics, an interesting question is whether higher order structures of actin filaments are altered. Actin networks can be reconstituted *in vitro* and analyzed with confocal microscopy. A common and easy method to label actin filaments uses the phallotoxins from *Amanita phalloides*, which specifically bind F-actin, but not actin monomers. Covalently linked to a fluorescent dye they are commercially available as phalloidin dyes.

Samples containing 4 μM actin isolated from rabbit skeletal muscle and antidepressants in different concentrations were polymerized in a sealed flow chamber for > 2 h to ensure an equilibrium state of the network. Polymerization was initiated by the addition of F-buffer and Alexa Fluor 488-phalloidin was used for visualization. Antidepressants were added to the sample at a constant volume from different stock solutions and the control was performed with the equivalent volume of the solvent 50% EtOH/5 mM HCl. The solvent itself did not affect actin polymerization (Supplementary Figure 1). Polymerized networks were then visualized at steady state in the confocal microscope (63x/1.4 NA oil immersion objective). Maximum projections of z-stacks of each sample are shown.

There were no effects on actin network structure by the addition of clomipramine, doxepin or citalopram at $R = 5$ or 50 (Figure 8). All samples showed pure filamentous networks lacking any alterations like bundled or crosslinked filaments.

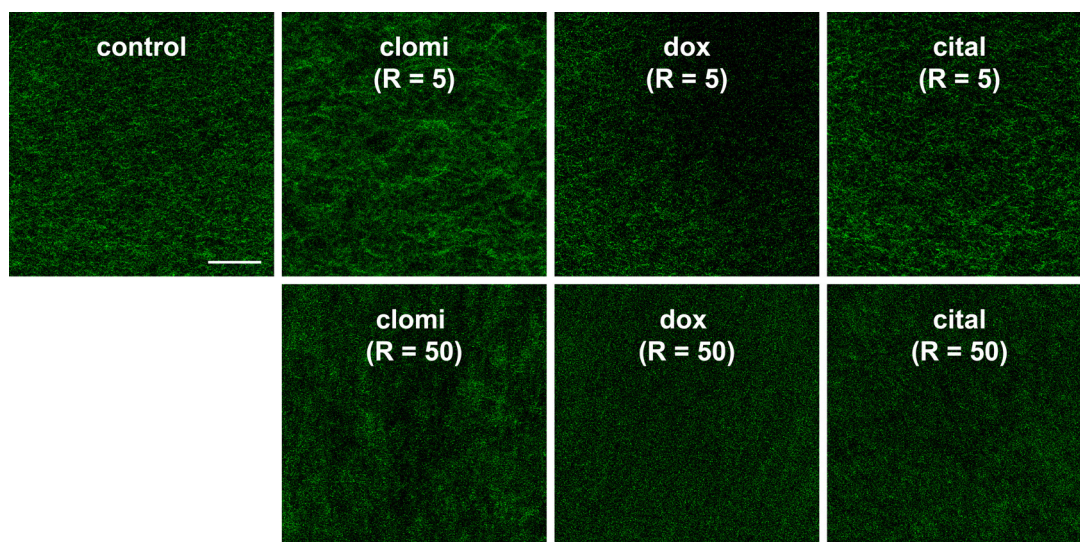


Figure 8. Antidepressants have no effect on actin network structure. Actin networks (4 μM actin) were polymerized in the presence of antidepressants at RT for > 2 h and visualized with phalloidin-488. Images were taken in a confocal microscope (63x/1.4 NA objective, 10 μm z-stacks). Scale bar denotes 50 μm . „R“ refers to the molar ratio of antidepressant:actin.

4.1.3. Actin-dependent effects of antidepressants in cells

Overall F-actin structure of astrocytes is unaffected by antidepressants

After characterization of the effect of clomipramine on actin dynamics in reconstituted *in vitro* systems, the actin network in cells was analyzed for possible structural alterations. Primary astrocytes from rat were chosen as a relevant cellular system, as they are crucial cells supporting and integrating brain function. Besides their structural and metabolic support of neurons, astrocytes are nowadays thought to be dynamic regulators of neural circuits in health and disease by controlling synapse formation and maturation (Clarke and Barres, 2013; Nedergaard et al., 2003). Thus, important actin-dependent processes in astrocytes impacting on synaptic function might be affected by clomipramine.

Primary rat astrocytes were cultivated for three days and treated with clomipramine, doxepin and citalopram at 1, 10 or 100 μM final concentration for 90 min. The control was performed with the solvent 50% EtOH/5 mM HCl. After fixing, nuclei were stained with DAPI, the actin cytoskeleton was stained with phalloidin and cell morphology was analyzed in the fluorescence microscope (Figure 9). At 1 and 10 μM , none of the three antidepressants showed obvious changes in F-actin structure. While doxepin and citalopram had no effect even at 100 μM , astrocytes treated with 100 μM clomipramine showed severe alterations: many cells were detached, while most of the remaining cells were contracted and in some cases exhibited a breakdown of stress fibers. However, an unspecific effect of clomipramine on the actin structure due to general cellular toxicity at this concentration cannot be excluded.

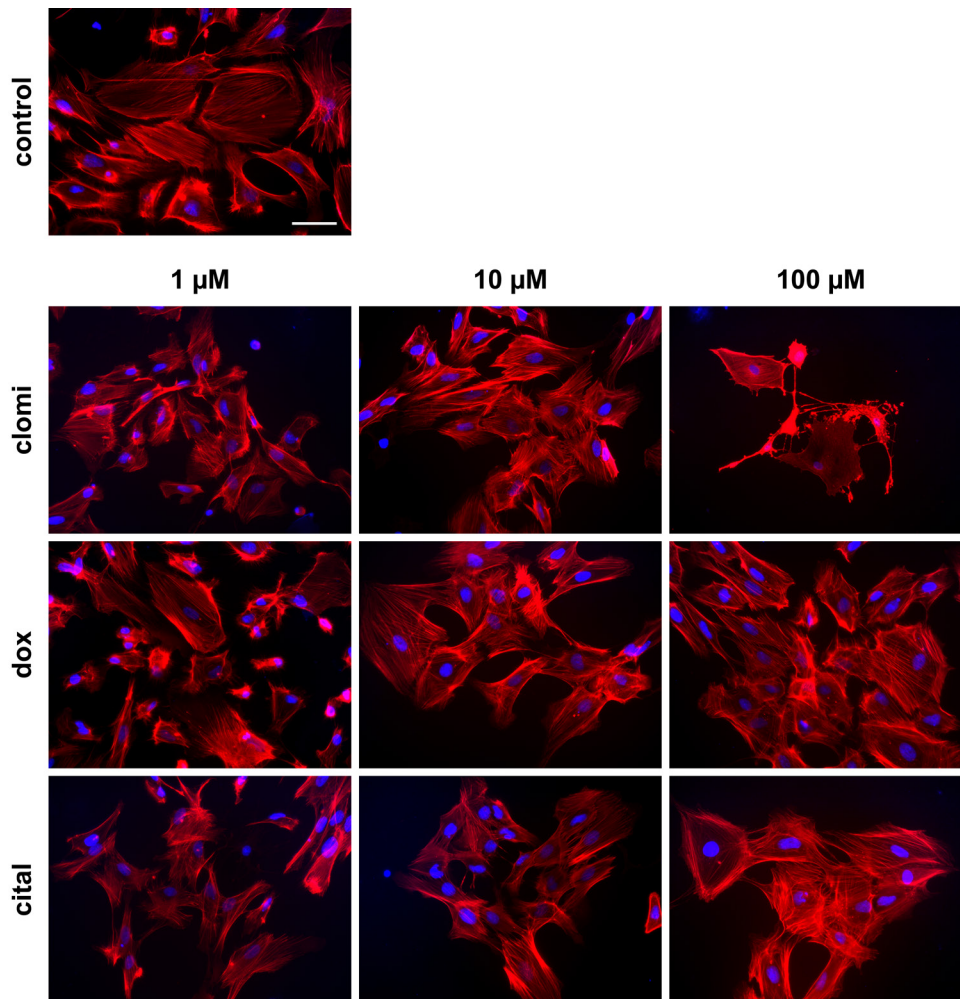


Figure 9. The overall structure of actin filaments in astrocytes is largely unaffected by antidepressants. Primary rat astrocytes were treated with antidepressant at the indicated concentrations for 90 min and fixed. Nuclei were stained with DAPI (blue), actin filaments with phalloidin (red). Images were taken with a fluorescence microscope (40x objective). Only clomipramine affects cellular morphology at high concentrations. Scale bar denotes 50 μm .

2D-Migration of HeLa cells is unaffected by clomipramine

In a next step, the impact of clomipramine on two crucial actin-dependent aspects of cellular function was analyzed: cell spreading and migration. Adhesion and extension of protrusion during spreading rely on elongation of actin filaments, while migration is a complex process of F-actin reorganization involving protrusion at the leading edge of a cell and retraction at the rear part (Pollard and Borisy, 2003; Pollard and Cooper, 2009). In the CNS, the importance of these processes becomes obvious in regard of neuronal migration during development or neurite extension during wiring of the brain.

For two-dimensional migration analysis, a classic “wound healing” or “scratch” assay was performed with HeLa cells. For this, a confluent cell layer was scratched with a pipette tip and the closing of the scratch or “wound” was monitored over time. Clomipramine was

added to the cells immediately after the scratch (10 and 20 μM wide) to assess its impact on migration. However, it did not show effects on migration of HeLa cells (Figure 10).

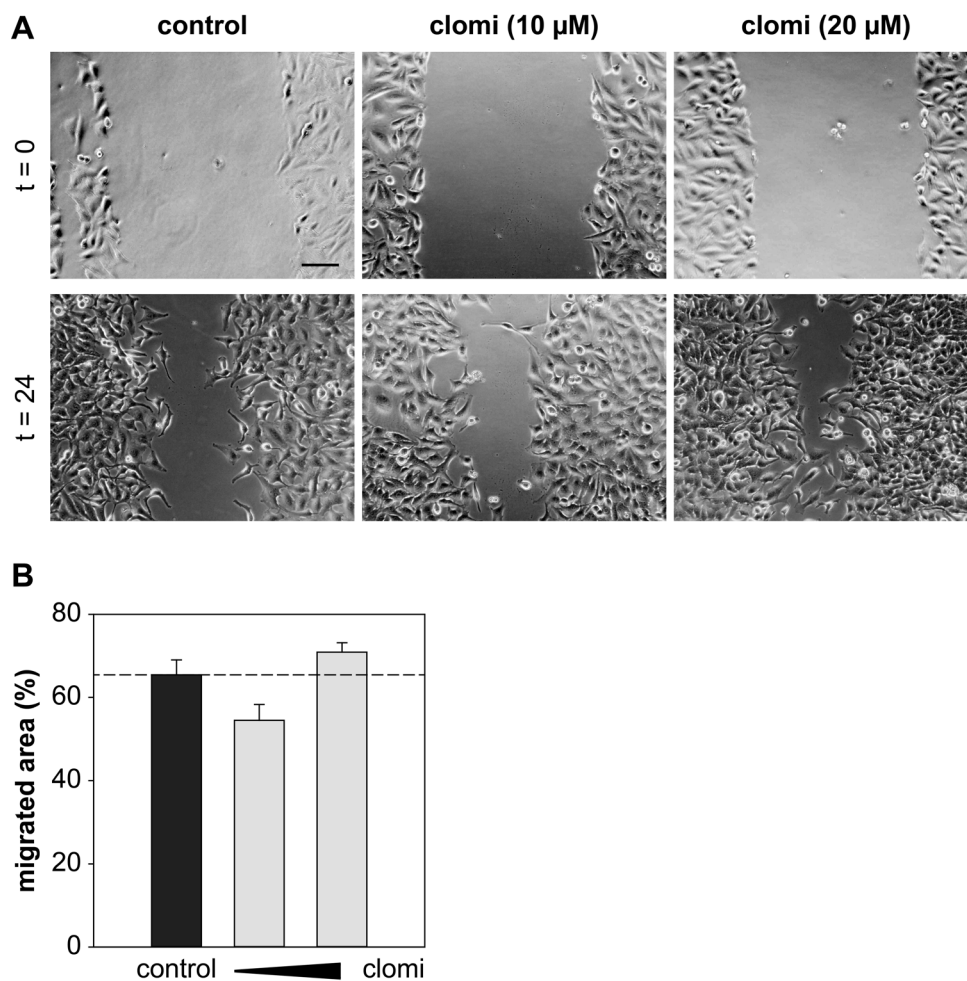


Figure 10. Clomipramine does not affect migration of HeLa cells in a 2D migration assay. A confluent HeLa cell layer in a 24-well plate was scratched with a pipette tip to mimic a wound in the presence or absence of clomipramine. (A) The cells were imaged immediately after the scratch ($t = 0$) and after 24 h. Images were taken with a bright field microscope (10x objective). Scale bar denotes 100 μm . (B) The migrated area was quantified in ImageJ as the normalized difference of the scratch area at $t = 0$ and $t = 24$ h. Bars represent means + SEM (control $n = 6$, clomi 10 μM $n = 6$, clomi 20 μM $n = 2$). There was no significant difference in comparison to control. Statistical analysis was performed with one-way ANOVA and Bonferroni *post hoc*.

High concentrations of clomipramine reduce HeLa cell spreading

While clomipramine had no effect on cellular migration, it significantly reduced spreading of HeLa cells (Figure 11). In this simple assay, HeLa cells were replated on a fibronectin-coated surface and simultaneously treated with clomipramine at 15 or 50 μM during spreading for 30 min. As a positive control for decreased actin polymerization the drug Cytochalasin D (Cyto D) was added to the cells at a final concentration of 2 μM . Cytochalasins are natural occurring molecules that inhibit polymerization by capping the growing ends of the filaments and thereby reduce cell spreading (Domnina et al., 1982;

Sampath and Pollard, 1991). While clomipramine had no effect on spreading at 15 μM , it reduced the cell size after 30 min of spreading to approximately 50% of the control cell size at 50 μM (Figure 11B). Cyto D, however, was much more potent in reducing cell size: at only 2 μM cells reached only about 25% of the control cell size.

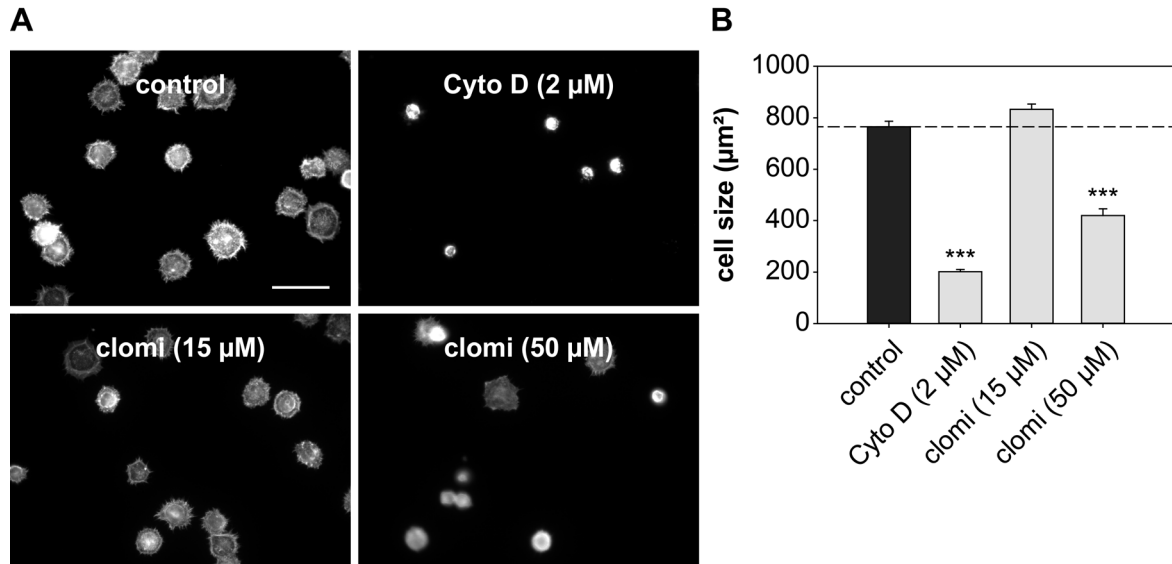


Figure 11. Clomipramine reduces spreading of HeLa cells at high concentrations. HeLa cells were replated on fibronectin-coated coverslips in the presence of clomipramine or Cyto D. After 30 min of spreading, cells were fixed and F-actin was stained with phalloidin. (A) Images were taken in a fluorescence microscope. Scale bar denotes 50 μm . (B) Quantification of cells size was performed in *ImageJ*. Bars represent means + SEM (n = cell number from one experiment, control and clomi n = 100-200 cells, Cyto D n = 30 cells). *** $p < 0.001$ in comparison to control. Statistical analysis was performed with one-way ANOVA and Bonferroni *post hoc*.

Taken together, clomipramine was the only of the three tested antidepressants to affect actin dynamics. It reduced actin polymerization in both, a label-based and a label-free approach, and this reduction can likely be attributed to decreased nucleation. Yet, in cells it only seems to affect actin-dependent processes at high concentrations (around 50 μM), while showing toxic effects at short treatments of 50-100 μM as evidenced by the unhealthy morphology of cells treated with this concentration (compare with Figure 9).

4.2. The stress-induced protein DRR1

The aim of this study was to thoroughly analyze the molecular effect of DRR1 on actin dynamics as well as to embed these findings into the overall knowledge about actin dynamics at the synapse and to shed light on DRR1's relevance for synaptic transmission and plasticity.

4.2.1. DRR1 has a tripartite effect on *in vitro* actin-dynamics

DRR1 directly interacts with F-actin

Initially, the actin binding ability of DRR1 was verified in cultured cells and *in vitro* with purified recombinant proteins. As a first step, actin binding of DRR1 ectopically expressed in HEK-293 cells was analyzed. DRR1 was overexpressed as a fusion protein with EGFP in HEK-293 and co-immunoprecipitated using GFP-Trap[®]. This Co-IP is based on agarose beads coupled to so-called nanobodies, recombinant single domain antibody fragments derived from alpaca, which feature high binding capacity and affinity. As expected and previously seen, DRR1 strongly bound actin in the Co-IP (Figure 12A) (Schmidt et al., 2011). The control was performed with EGFP protein and no actin binding could be detected.

However, indirect binding of DRR1 to actin cannot be excluded with the Co-IP experiment. It is also impossible to deduce whether binding occurs at actin monomers or filaments. Thus, an *in vitro* binding assay specific for F-actin was performed with purified recombinant DRR1 and purified actin from rabbit skeletal muscle. Actin filaments can be separated from globular actin by centrifugation at $\sim 150,000\times g$. While actin filaments sediment at this speed together with any F-actin binding proteins, G-actin remains in the supernatant. DRR1 was expressed in *E. coli* bacteria as a fusion protein with the maltose binding protein (MBP) in order to enhance its solubility and stability as well as for affinity purification.

For the co-sedimentation experiment, actin was polymerized at RT for 1 h to reach the equilibrium state. DRR1 was then added to the preformed filaments and after 30 min of incubation the sample was centrifuged to separate F- and G-actin. Samples of total protein (T) prior to centrifugation, supernatant (S) containing G-actin and non-F-actin binding protein, and pellet (P) samples with F-actin and F-actin binding protein were taken and analyzed by SDS-PAGE and colloidal Coomassie staining (Figure 12B). Actin and DRR1 were distinguished on the gel by their difference in molecular weight: actin has 42 kDa and DRR1 (as a fusion protein with MBP) 60 kDa. The control was performed with the protein MBP. All experiments with recombinant proteins were performed with

buffer only and MBP as controls, respectively. Since there were no detectable differences between buffer and MBP, the latter is shown in all figures as control. MBP itself did not affect actin dynamics (Supplementary Figure 1).

The amount of co-sedimented DRR1 (amount in P) was indirectly calculated as the difference before and after centrifugation (i.e. amount in S subtracted from the amount in T). A control without F-actin was made for each sample and subtracted from the co-sedimentation value, i.e. DRR1 was centrifuged alone, to quantify background sedimentation. The background-corrected co-sedimented DRR1 was then normalized to the amount of F-actin in each corresponding sample, also indirectly calculated from the decrease of actin signal from the total sample to the supernatant sample. Samples from the total protein and the supernatant are more adequate for quantification, as they are clean from contaminations. The pellet sample on the other hand is contaminated with supernatant and was therefore only used as a visual reference on the protein gel.

In spite of its complexity, this method of quantification was reliable and highly reproducible. In contrast, simply measuring the amount of protein in the pellet showed considerable variations derived from fluctuating amounts of residual supernatant.

At a ratio of DRR1:actin of 1:10 about 60% of DRR1 is bound to F-actin, demonstrating direct binding of DRR1 to the filament (Figure 12C). With increase of DRR1, the percentage of co-sedimentation decreased slightly. At $R = 0.25$, roughly 58% of DRR1 protein co-sedimented, while at a ratio of 1:2, about 50% of DRR1 was found in the pellet.

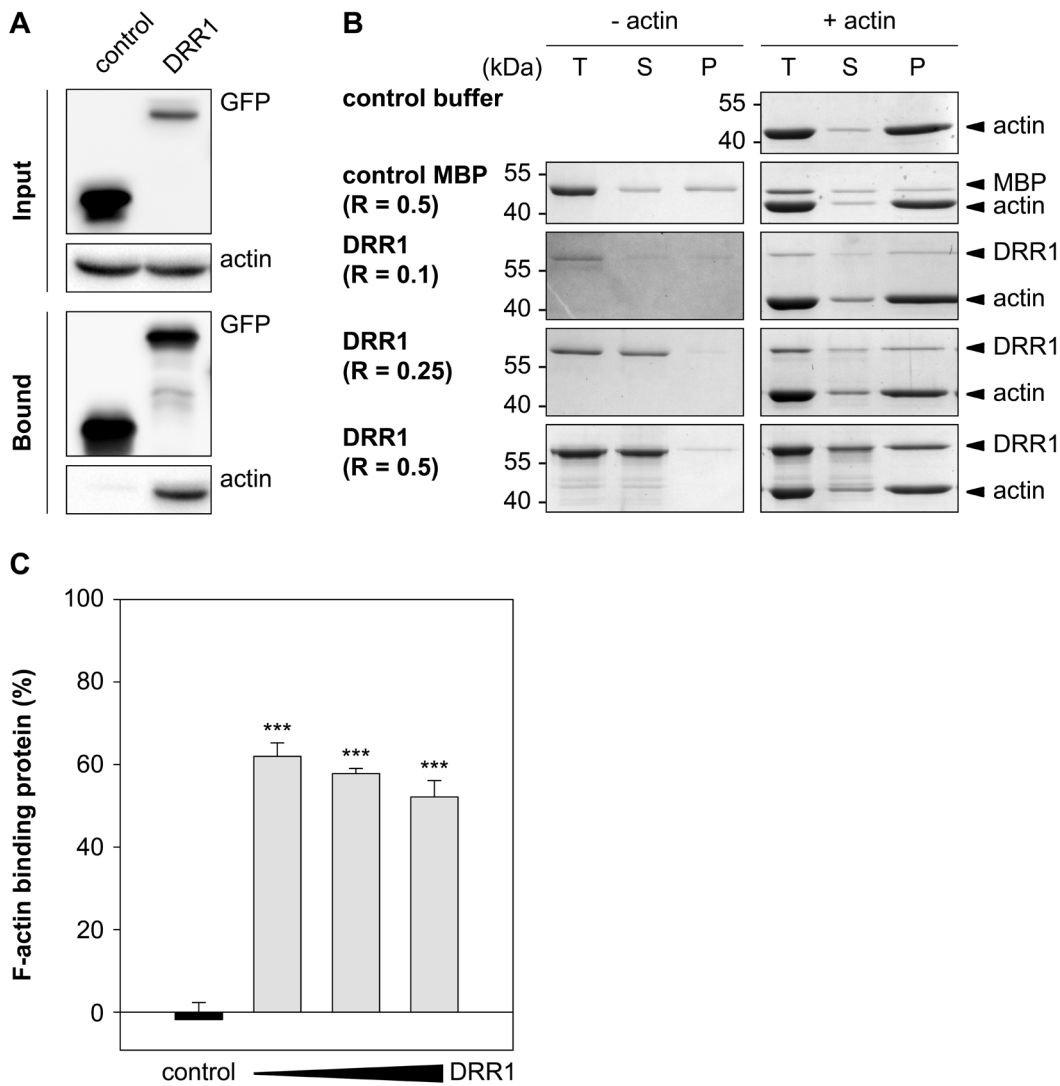


Figure 12. DRR1 binds actin in HEK-293 and F-actin *in vitro* in a concentration-dependent manner. (A) Co-immunoprecipitation with GFP-Trap[®] of DRR1 fused to EGFP overexpressed in HEK-293 cells. Control was performed with EGFP alone. Lysate and eluate samples were analyzed by SDS-PAGE and Western Blot. A representative Western Blot is shown. (B) Co-sedimentation of DRR1 recombinant protein with preformed F-actin (1 μ M) by ultracentrifugation. Coomassie-stained SDS-PAGE with total (T), supernatant (S) and pellet (P) fractions for controls and wt in different concentrations are shown. „R“ refers to the molar ratio of DRR1:actin. (C) Quantification of co-sedimented protein (DRR1 in R = 0.1, 0.25, 0.5) was calculated by subtracting background sedimentation (“- actin“ samples) and is shown as the fraction of total protein (n = 3). Bars represent means + SEM. *** p < 0.001 in comparison to control. Statistical analysis was performed with one-way ANOVA and Bonferroni *post hoc*.

DRR1 slows down actin polymerization in the pyrene-assay

The impact of DRR1 on actin polymerization was analyzed in a pyrene-assay as described before for antidepressants (chapter 4.1.1.). Shortly, the fluorescence of actin labeled with the aromatic hydrocarbon pyrene is strongly enhanced upon polymerization. This effect is used to monitor the polymerization reaction. DRR1 was added as a purified protein to 5 μM 20% pyrene-labeled actin at different concentrations (1.5, 3 and 5 μM) and the polymerization reaction initiated by the addition of F-buffer. In a fluorescence spectrometer, the reaction was monitored by following the absorbance at 407 nm.

At the lowest concentration ($R = 0.3$), DRR1 strongly slowed down the polymerization reaction. This effect was concentration-dependent and increased with more DRR1. While the control reached equilibrium after around 80 min, even with the lowest DRR1 concentration of $R = 0.3$, it did not fully reach equilibrium after 90 min. The end-point fluorescence value in the pyrene-assay provides an estimate of the amount of F-actin in the sample if the sample consists of filamentous actin only. With DRR1, this apparent amount was remarkably reduced. However, certain factors can distort the final value, especially light scattering due to network or bundled actin structures. Without knowledge of the network structure, the end value of the pyrene-assay can therefore not directly be attributed to the amount of F-actin.

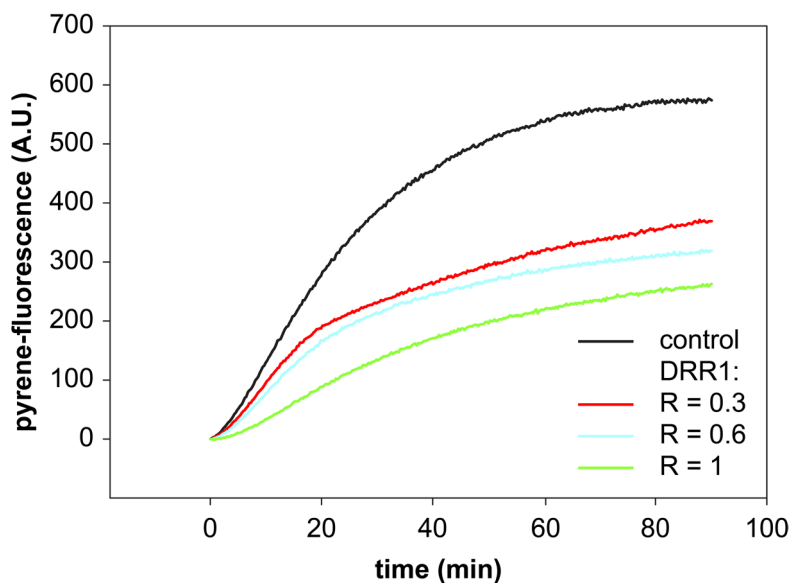


Figure 13. DRR1 inhibits *in vitro* polymerization of pyrene-labeled actin. Actin filaments ($c = 5 \mu\text{M}$, 20% labeled with pyrene) were polymerized in the presence of DRR1. Increase in fluorescence of pyrene-actin during polymerization of G-actin to F-actin was monitored in 5 s intervals for 90 min. Representative curves are shown. „R“ refers to the molar ratio of DRR1:actin.

DRR1 generates thick bundles in F-actin networks

In order to answer the question whether actin networks are altered by DRR1 and to verify its previously reported bundling activity, purified G-actin was polymerized in a sealed flow chamber in the presence of DRR1. Phalloidin was added coupled to a fluorophore to visualize actin filaments. Networks were polymerized > 2 h at RT to ensure an equilibrium state. Polymerized networks were then visualized at steady state in the confocal microscope (63x/1.4 NA oil immersion objective). Maximum projections of z-stacks of each sample are shown.

The polymerization in the absence of DRR1 (control) produced a purely entangled filamentous network, where single filaments can hardly be distinguished. In the presence of DRR1, thick actin bundles started to appear already at a ratio of 1:10, verifying the known bundling effect. At R 0.1, the network is composed of a mixture of filaments and bundles, with apparently more filaments. With increasing amount of DRR1, this pattern shifts towards more bundles resulting in a heavily bundled network at $R = 0.5$ (Figure 14).

Due to these bundles, the fluorescence of pyrene-actin in the previous assay is likely to be strongly reduced. Therefore, no conclusion about the amount of F-actin polymerized in the presence of DRR1 can be drawn from the pyrene-assay.

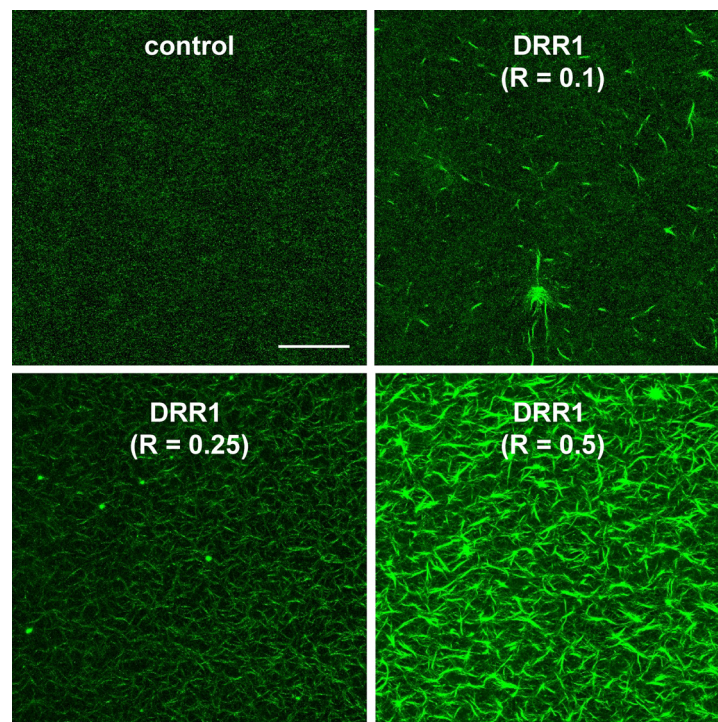


Figure 14. DRR1 strongly bundles actin filaments in a polymerized network. Actin networks ($4 \mu\text{M}$ actin) were polymerized in the presence of DRR1 at RT for > 2 h and visualized with phalloidin-488. Images were taken in a confocal microscope (63x/1.4 NA objective, $10 \mu\text{m}$ z-stacks). Scale bar denotes $50 \mu\text{m}$. „R“ refers to the molar ratio of DRR1:actin.

DRR1 reduces single filament elongation and increases nucleation

Finally, the polymerization reaction in the presence of DRR was also visualized in the confocal microscope, to analyze effects on single filament elongation and nucleation. In contrast to the networks above, where 10 μm thick z-stacks of the network were imaged, in this assay, actin filaments were bound to the surface via heavy meromyosin, which was adsorbed to the surface. Therefore, single filaments can be imaged and bundling of the filaments is likely to be strongly reduced.

Samples were prepared containing F-buffer for polymerization and DRR1 at different concentrations and the polymerization was initiated by the addition of G-actin. The sample was then immediately pipetted into a flow chamber and placed in the confocal microscope. At 2 min after starting the polymerization, images of the growing filaments were recorded every 3 s for 10 min (63x/1.4 NA objective, 5x zoom).

With this approach, a novel effect of DRR1 was revealed: the time-lapse images showed reduced elongation, while apparently more filaments were polymerizing in the captured field, suggesting enhanced nucleation (Figure 15A).

The image analysis for single filament elongation and nucleation rate was performed with *ImageJ*. The single filament elongation rate was quantified as the slope of the plot filament length vs. time. For nucleation analysis, filaments in 4-8 frames with 30 s intervals (during the first 5 min of polymerization) were counted and the slope of the plot number of filaments vs. time was determined as the nucleation rate. The barbed and the pointed end of the filaments could clearly be distinguished because of the growth rate, indicating that the addition of new actin subunits at the barbed ends was heavily inhibited by DRR1. This effect is commonly described as filament capping.

At $R = 0.1$, DRR1 reduced the single filament elongation rate to 30% of the control. At $R = 0.25$ the elongation rate was about 20% and at $R = 0.1$ less than 10%. These results present DRR1 as a potent capping protein, a function that was unknown before. Moreover, quantification of the nucleation rate showed enhanced nucleation concomitant with the novel capping effect. The nucleation was enhanced more than 3fold at $R = 0.5$. While this effect was significant and notable, it seems to be less significant than the capping effect. Furthermore, the enhanced nucleation could be an indirect effect *in vitro* dependent on the strong capping activity. With the strongly reduced growth of the filaments, the concentration of G-actin remains higher over time, allowing for a higher nucleation rate.

Taken together, a tripartite effect of DRR1 on actin dynamics was revealed *in vitro*. In addition to the previously described bundling effect, a pronounced capping activity was identified concomitant with nucleation activity. Thereby DRR1 shifts the actin network towards more, shorter and strongly bundled filaments.

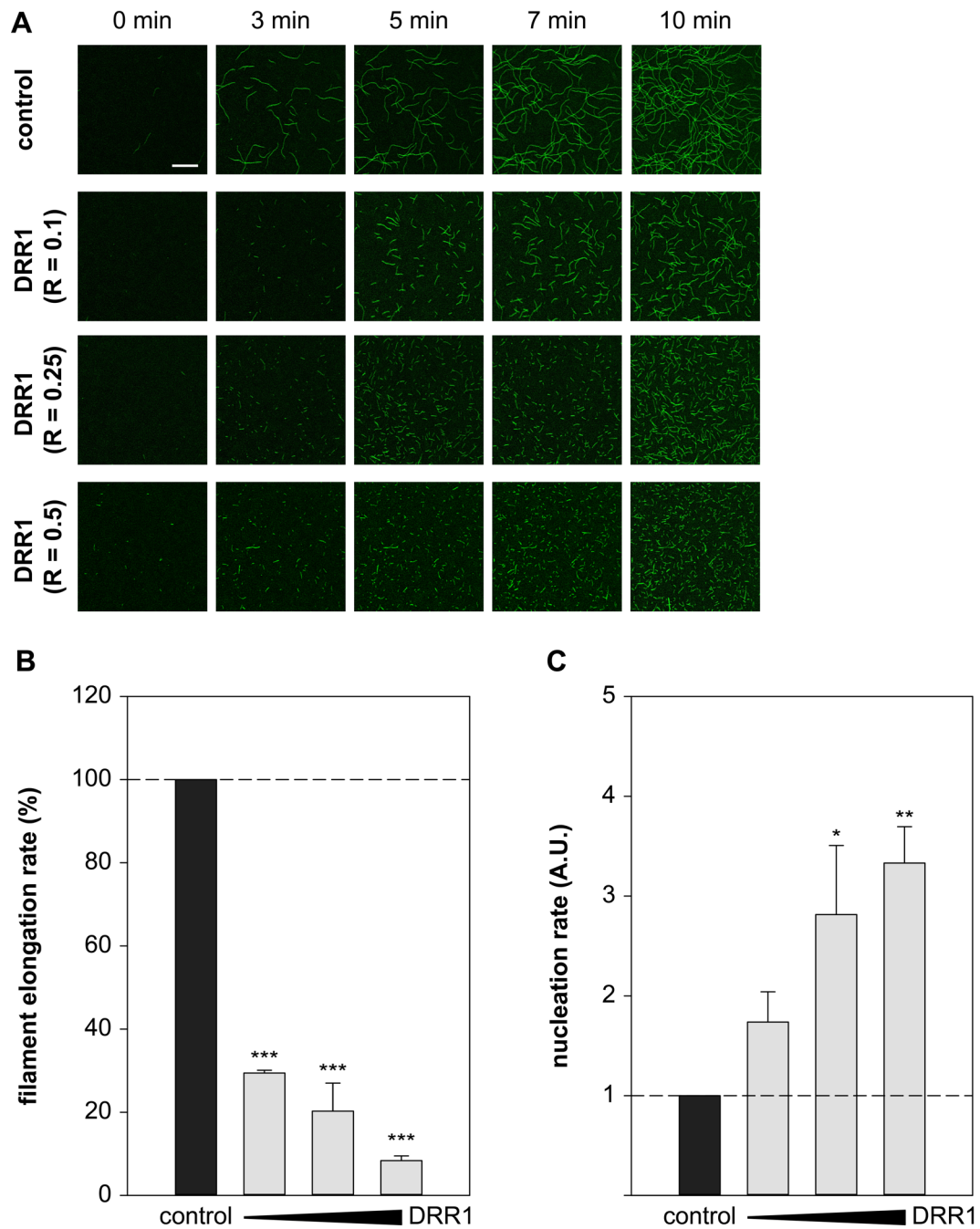


Figure 15. DRR1 strongly reduces single filament elongation and increases nucleation rate. (A) Confocal time-lapse images of *in vitro* actin polymerization (1 μ M actin) in the presence of DRR1 indicates inhibition of single filament elongation at the barbed end. Filaments were visualized by phalloidin. Scale bar denotes 10 μ m. „R“ refers to the molar ratio of DRR1:actin. (B) Quantification of filament elongation rate normalized to the control (n = 3, DRR1 in R = 0.1, 0.25, 0.5). (C) Nucleation rate defined as the slope of number of filaments per frame quantified in 3-5 frames (with 30 s intervals) normalized to the control (n = 3 – 4, DRR1 in R = 0.1, 0.25, 0.5). Bars represent means + SEM. * p < 0.05, ** p < 0.01, *** p < 0.001 in comparison to control. Statistical analysis was performed with one-way ANOVA and Bonferroni *post hoc*.

4.2.2. The functions of DRR1 are executed by two actin-binding regions and a dimerization domain

Domain analysis of DRR1 and design of truncation mutants

In order to identify actin binding regions of DRR1, several truncation and point mutants were generated. As there is no crystal structure available for DRR1, a sequence conservation analysis and a secondary structure prediction were made to design the mutations.

Murine DRR1 is a highly conserved protein with 144 amino acids containing the “conserved domain of unknown function 1151” (Figure 16A). Its paralog FAM107B lacks the first 15 N-terminal amino acids, but otherwise is highly conserved among most species from human, mice and rat to *Xenopus* and zebrafish. The secondary structure prediction revealed it to be a predominantly helical protein with three helices. The N-terminal domain is mostly unstructured loop region with a small helix, followed by the largest helix in the middle domain and a third C-terminal helix. A coiled coil motif was predicted from amino acids 66 to 93, i.e. within the central helical region, in the murine sequence. Coiled coils are protein motifs known to mediate protein-protein interactions and as such are interesting domains to be analyzed (Figure 16B).

Based on the tripartite domain structure suggested by the secondary structure prediction, three mutants were cloned during previous work each lacking one domain: dN, dC and dM, as well as the isolated central helix M (Kretzschmar, 2010). In the present study, three further mutants were cloned: the N-terminal domain (N) and two point mutants dPEPE and C94A (Figure 16C). The mutant dPEPE was published by Le et al., 2010, as a mutant lacking the actin binding sites of DRR1 as concluded from colocalization analysis in cells. Two so-called “PE-motifs” at positions 65 and 122 were mutated to AA, a mutation that disrupted colocalization with actin in cells (Lee et al., 2010). DRR1 exerts only one cysteine residue at position 94. The previously described interaction with Prdx1 (Schmidt et al., 2011) led to the speculation that C94 might have a potential redox-regulated function. Thus, the C94A mutant was generated.

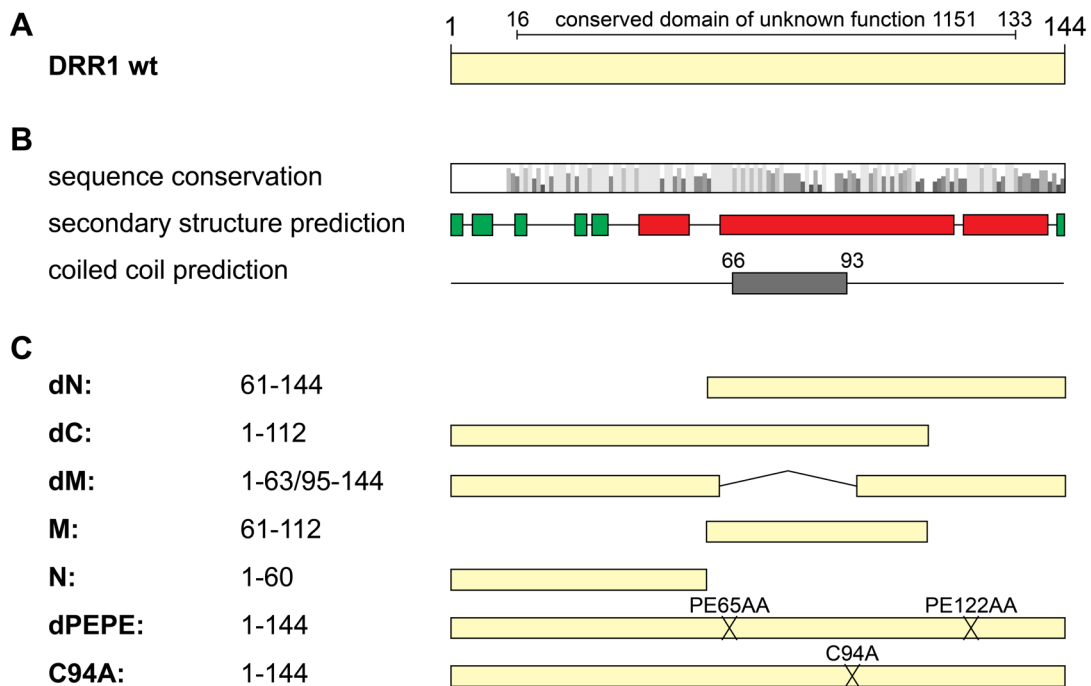


Figure 16. Domain structure and mutants of DRR1. (A) Murine DRR1 has 144 amino acids and contains the „domain of unknown function 1151“ from amino acid 16-133. (B) Sequence conservation of DRR1 with the closely related protein FAM107B from human, rat and mouse is shown. Secondary structure prediction was performed with the „Predict Protein Server“ (green: loop, red: helix). Coiled coil prediction was performed with the online tool „Coils“ (window: 21). (C) Truncation and point mutants of DRR1 used in this work. dPEPE was published by Le et al., 2010, as a mutant lacking the actin binding sites of DRR1 as concluded from colocalization analysis in cells.

Identification of two actin binding regions in DRR1

Using the same two approaches as for the wild type DRR1 (wt), the actin binding abilities of the mutants were analyzed with a Co-IP experiment in HEK-293 cells and in an F-actin co-sedimentation assay (described in chapter 4.2.1.).

The Co-IP using GFP-Trap showed that all mutants except M are able of co-precipitating actin from HEK-293 cells (Figure 17A). The finding that both the mutants dN and dC bound actin, while the M mutant didn't, indicates the presence of two separate actin binding regions in DRR1. Likely, the first and the third helix bind actin, while the central helix containing the coiled coil motif mediates protein-protein interactions. The series of Co-IPs, however, showed some variations from experiment to experiment. For quantification of the relative actin binding, the “mean actin binding” in each experiment was calculated from the amount of (background corrected) actin in the eluates of wt, dN, dC, dM and M, and the binding of each DRR1 mutant was related to this mean. While the wt, dN and dM mutants showed statistically significant actin binding, this was not the case for dC, M and N. It was remarkable that dPEPE showed actin binding similar to DRR1 wt, in spite of being previously described as non-actin binding mutant.

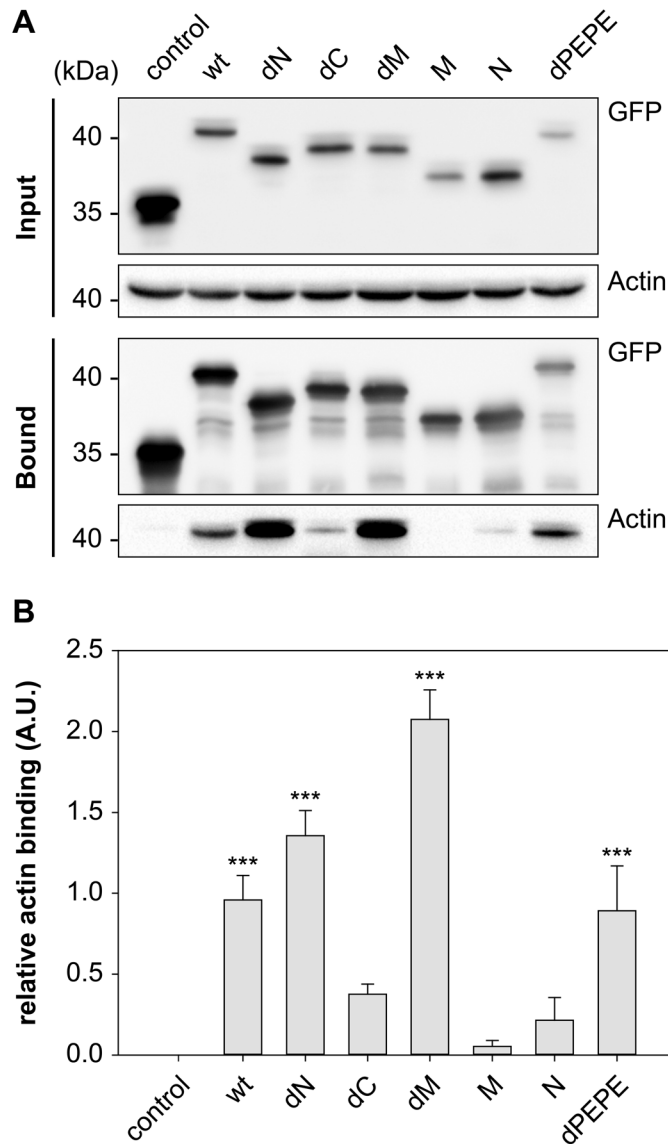


Figure 17. DRR1 shows two actin binding regions separated by a central non-binding region. (A) Co-immunoprecipitation with GFP-Trap[®] of DRR1 wt and mutants fused to EGFP overexpressed in HEK-293 cells. The control was performed with untagged EGFP instead of the DRR1-EGFP fusions. Lysate and eluate samples were analyzed by SDS-PAGE and Western Blot. A representative Western Blot is shown. (B) Quantification of Co-immunoprecipitation (n = 8, dN and M n = 7, N n = 4). Background corrected actin binding was normalized to mean actin binding for each experiment. Bars represent means + SEM. *** p < 0.001 in comparison to control. Statistical analysis was performed with one-way ANOVA and Bonferroni *post hoc*.

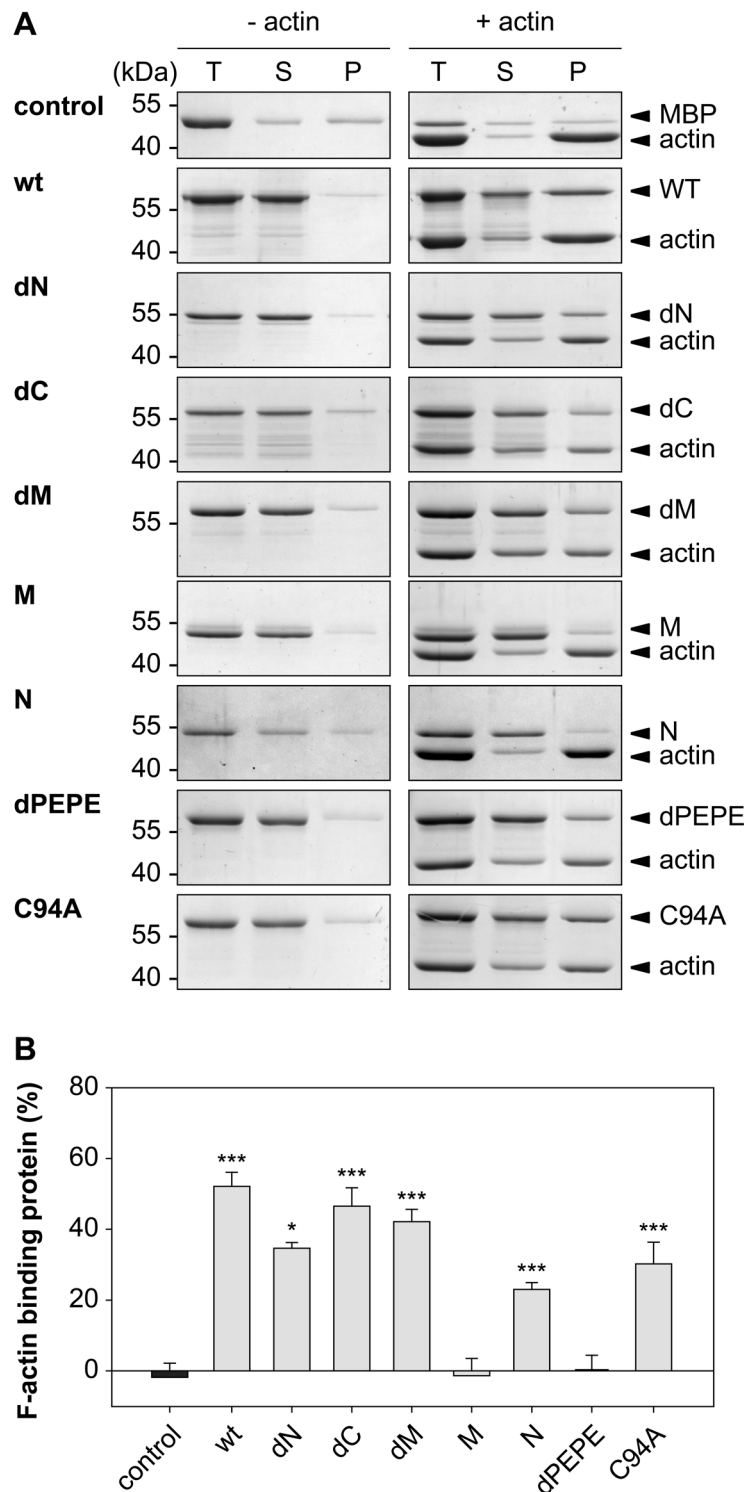


Figure 18. Both actin binding regions bind F-actin *in vitro*. (A) Co-sedimentation of DRR1 wt and mutants recombinant protein with preformed F-actin (1 μ M) by ultracentrifugation (R = 0.5). Coomassie-stained SDS-PAGE with total (T), supernatant (S) and pellet (P) fractions for mutants are shown. (B) Quantification of co-sedimented protein was calculated by subtracting background sedimentation (“- actin“ samples) and is shown as the fraction of total protein normalized to the respective amount of F-actin (n = 3). „R“ refers to the molar ratio of DRR1:actin. Bars represent means + SEM. * p < 0.05, *** p < 0.001 in comparison to control. Statistical analysis was performed with one-way ANOVA and Bonferroni *post hoc*.

The co-sedimentation experiment as an indicator of F-actin binding *in vitro* appeared to be more reliable and reproducible than the Co-IP. According to the results from the Co-IP, there was highly significant binding to F-actin for DRR1 wt and the mutants dN, dM, and C94A. The mutants dC and N showed some binding, but the level of significance was not reached (Figure 18). The control (with untagged MBP), M and dPEPE did not co-sediment with F-actin. Two findings diverged from the Co-IP. First, dPEPE did not bind F-actin, suggesting that the binding found with the Co-IP might be derived from interaction with G-actin. Second, dC showed stronger binding to F-actin than dN, although in the Co-IP dN co-precipitated more actin than dC. Presumably, the two-actin binding sites diverge in their affinities towards G- and F-actin.

Slowdown of actin polymerization in the pyrene-assay by the mutants dM and C94A

The DRR1 mutants were also assessed in the pyrene-assay. Only two mutants slowed down polymerization to a similar extent as DRR1 wt: dM and C94A. While dN and M showed virtually no difference to the control, dC and dPEPE appeared to alter the shape of the polymerization curve slightly ending up with less F-actin (Figure 19). As outlined above (see chapter 4.2.1.), this might be influenced by scattering of the light caused by the actin network structure or to slight variations in the amount of G-actin in the sample (derived from pipetting inaccuracy).

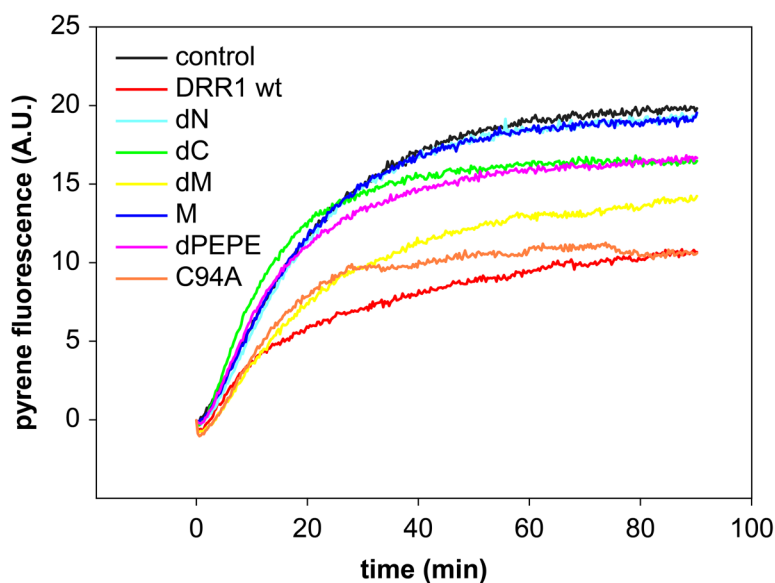


Figure 19. *In vitro* polymerization of pyrene-labeled actin is inhibited by DRR1 wt, dM and C94A. Actin filaments (5 μ M, 20% labeled with pyrene) were polymerized in the presence of DRR1 proteins ($R = 0.5$). Increase in fluorescence of pyrene-actin during polymerization of G-actin to F-actin was monitored in 5 s intervals for 90 min. Purified MBP instead of the MBP-DRR1 fusion proteins served as control. Representative curves are shown.

Effects of DRR1 mutants on single filament elongation and nucleation

In order to analyze the effects of the mutants on single filament elongation and nucleation, polymerization was visualized by confocal microscopy as before (for DRR1 wt, see Figure 15). The prevailing reduction of filament elongation rate concomitant with enhanced nucleation found for DRR1 wt was also observed for the mutants dM and C94A. Therefore, the reduction of polymerization in the pyrene-assay can clearly be attributed to reduced single filament elongation, i.e. capping. This capping effect is only effective with both actin binding regions of DRR1, as only the mutants featuring both regions, i.e. dM and C94A, displayed this effect.

Intriguingly, the mutant dPEPE showed a slight, albeit not significant reduction of the polymerization rate, but enhanced nucleation comparable to the wt. Again, this might suggest a certain activity of dPEPE in binding to G-actin or even in stabilizing actin nuclei, but the capping effect at the filament is lacking as the mutant is unable to bind to F-actin. Moreover, this result suggests nucleation as an independent effect of capping.

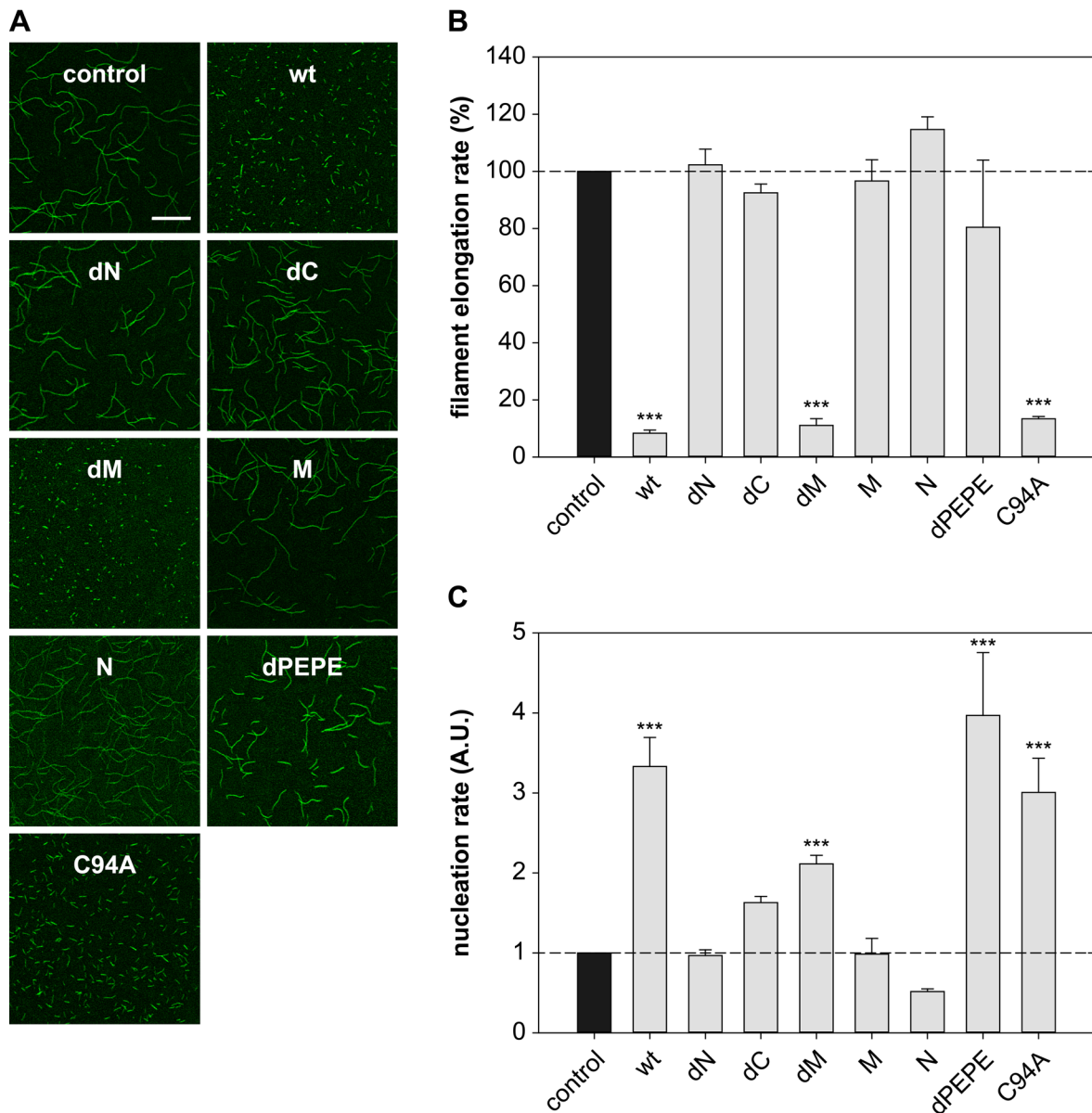


Figure 20. Single filament polymerization is inhibited by DRR1 wt, dM and C94A, while nucleation is enhanced by DRR1 wt, dM, dPEPE and C94A. (A) Confocal time-lapse images of *in vitro* actin polymerization (1 μ M actin) in the presence of DRR1 mutants (R = 0.5) indicates inhibition of single filament elongation only for wt, dM and C94A. Images at 5 min after induction of polymerization are shown. Filaments were visualized by phalloidin-488. Scale bar denotes 10 μ m. (B) Quantification of filament elongation rate normalized to the control (MBP instead of the DRR1-MBP fusion proteins, n = 3). (C) Nucleation rate defined as the slope of number of filaments per frame quantified in 3-5 frames (with 30 s intervals) normalized to the control (dN, N, dPEPE and C94A n = 3, wt and N n = 4, control, dC and dM n = 5). „R“ refers to the molar ratio of DRR1:actin. Bars represent means + SEM. *** p < 0.001 in comparison to control. Statistical analysis was performed with one-way ANOVA and Bonferroni *post hoc*.

Effects of DRR1 mutants on actin bundling

There are several ways in which a protein can crosslink or bundle actin filaments: either the protein exerts (at least) two actin binding sites mediating direct crosslinking, or it exerts one binding site and is able to dimerize, generating crosslinks as a dimer (or multimer). In order to dissect this aspect of DRR1's molecular mechanism, actin networks polymerized in presence of each mutant were visualized in the confocal microscope as described above (chapter 4.2.1).

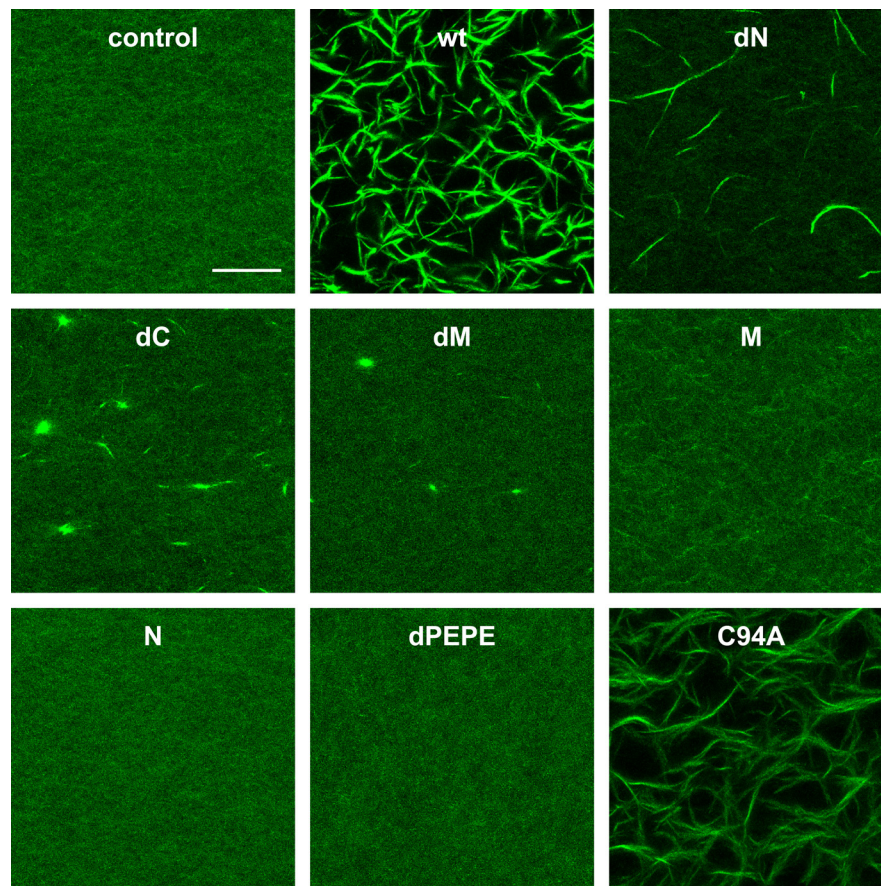


Figure 21. All DRR1 mutants show deficits in actin bundling. Actin networks ($4 \mu\text{M}$ actin) were polymerized in the presence of DRR1 wt or mutants at RT for > 2 h and visualized with phalloidin-488 ($R = 0.5$ each protein, „R“ refers to the molar ratio of DRR1:actin). Images were taken in a confocal microscope (63x/1.4 NA objective, 3x zoom, $10 \mu\text{m}$ z-stacks). Scale bar denotes $20 \mu\text{m}$.

In spite of exerting two actin binding sites, the mutant dM did only show amorphous bundle “aggregates”, but no proper actin bundling activity, suggesting that the central region is necessary as a spacer for accurate positioning of the two actin binding regions. Surprisingly, the mutants dN and dC both had an impact on actin networks, although exerting only one actin binding region each. While dC showed bundle-like aggregates, dN generated nicely bundled actin similar to the wt in a lower concentration (see Figure 14, wt $R = 0.1$). The presence of these bundles and aggregates with these two mutants is likely alleageable to homodimerization of DRR1. The mutants M, N and dPEPE had no

effect on the actin networks and appeared similar to the control. This was expected in all three cases: for M and dPEPE due to the missing F-actin binding ability, and in the case of N due to exerting only one actin binding site. C94A showed a strong bundling activity as expected. However, the bundles appeared to be less stiff and narrow than the ones of the wt as their visual appearance was longer, less straight and more diffuse (Figure 21).

Analysis of homo-dimerization of DRR1

To evaluate dimerization of DRR1 more directly, HEK-293 cells ectopically expressing DRR1 were treated with chemical crosslinkers. Two crosslinkers were selected: DSS (Disuccinimidyl suberate), a lysine-lysine crosslinker and BMB (1,4-Bismaleimido-butan), a cysteine-cysteine crosslinker. While DRR1 features many lysine residues, it only has one cysteine at position 94. In addition, with a spacer arm length of 11.4 Å, DSS is slightly longer than BMB with 10.9 Å. Both crosslinkers are membrane-permeable allowing for intracellular crosslinking.

Cells were detached from the surface, intracellular crosslinking was performed in suspension and the cells were lysed after quenching the reaction. The lysates were analyzed with SDS-PAGE and Western Blot. With DSS, about half of DRR1 wt was crosslinked into a dimer. Both mutants dN and dC still were crosslinked to a dimer, but significantly less than the wt. The mutant dM, having both actin binding regions but lacking the central spacer, still showed some dimerization, roughly about 1/4 of the protein. Finally, there is also evidence for dimerization of the mutant M, but much less than all other mutants (Figure 22B). These results suggest that dimerization is brought about by the central region presumably containing the coiled coil although it might depend on F-actin binding. In addition, binding to F-actin likely increases and stabilizes dimerization. Furthermore, the possibility cannot be excluded that the dimer-sized band after crosslinking is not only derived from a dimerized DRR1, but is also due to its dense packing within the bundle.

With the cysteine-cysteine crosslinker BMB similar results were obtained (Figure 22C). Neither the mutant dM nor C94A were dimerized as they are lacking the cysteine residue. dN and dC showed stronger dimer bands than with DSS and dPEPE was strongly dimerized as well. Only the potential dimer bands below 15 kDa of the mutant M appeared to be much weaker, if present. Nevertheless, the crosslinking of dN, dC and M mediated by cysteine at position 94 further suggest dimerization of DRR1 via the central coiled coil motif. As also dPEPE, which lacks F-actin binding ability, is crosslinked into a dimer, it is likely that DRR1 is dimerized independently of the position at the actin filament.

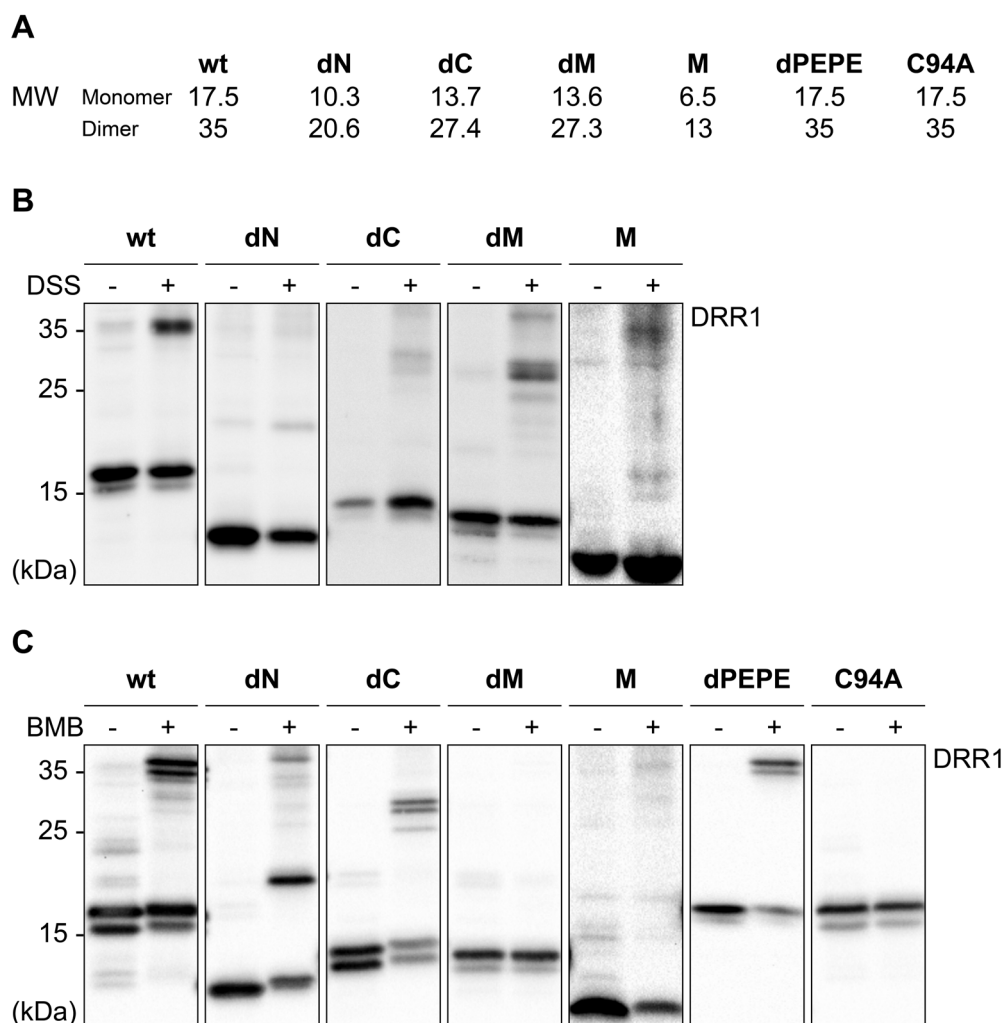


Figure 22. DRR1 is crosslinked by the chemical crosslinkers DSS and BMB in HEK-293 cells. (A) Expected molecular weight (MW) for DRR1 monomers and dimers in kDa. HEK-293 cells transfected with DRR1 wt or mutants were incubated with the lysine-lysine crosslinker DSS (B) or the cysteine-cysteine crosslinker BMB (C). Lysates were analyzed by SDS-PAGE and Western Blot. Representative Western Blots are shown.

The model of DRR1 homodimerization via the central helix in the M domain and presumably via the coiled coil was further tested with actin networks polymerized in the presence of a mixture of DRR1 wt and the mutant M in a 1:1 molar ratio and visualized in the confocal microscope with phalloidin as indicated above. Indeed, M interfered with the wt-induced bundling, as the actin network appeared less bundled and showed F-actin clusters when M was added to DRR1 wt (Figure 23, compare the second and the fourth panel). This is consistent with the mutant M being able to dimerize with DRR1 wt and since it misses F-actin binding regions it reduces bundling.

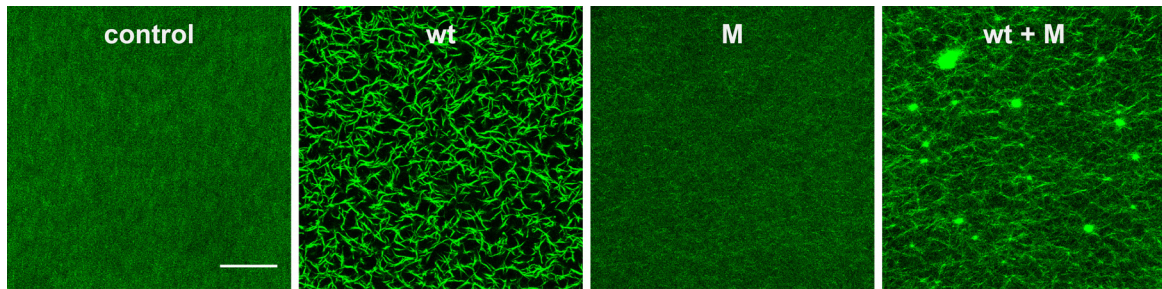


Figure 23. The middle domain interferes with actin bundling of full length DRR1 (wt). Actin networks (4 μ M actin) were polymerized at RT for > 2 h and visualized with phalloidin-488 (R = 0.5 each protein, „R“ refers to the molar ratio of DRR1:actin). Images were taken in a confocal microscope (63x/1.4 NA objective, 10 μ m z-stacks). Scale bar denotes 50 μ m.

4.2.3. DRR1 localizes to both the cytosol and the nucleus

Wang et al. described a nuclear localization for ectopic DRR1 in the cell line HTB-46 derived from renal cell cancer using MYC-based detection of tagged DRR1 and propidium iodide counterstaining of nuclei. Moreover, a nuclear localization signal (NLS) was predicted for the central region from amino acids 90 to 106 in the human DRR1 sequence (Wang et al., 2000). However, using the freely available secondary structure prediction tool “Predict protein server” (<https://www.predictprotein.org/>) for the mouse DRR1 sequence no NLS was predicted. A nuclear localization was also confirmed in the lung cancer cell line A549, as about 76% of cells ectopically expressing a DRR1-EGFP fusion showed a signal in the nucleus (Zhao et al., 2007).

In order to verify these findings as well as to analyze the subcellular localization of all DRR1 mutants used in this work, a biochemical fractionation of the cytosol and nucleus was performed. For this, the outer membrane of HEK-293 cells ectopically expressing DRR1 wt or mutants was lysed with a hypotonic lysis buffer without disrupting the nuclear membrane. Cytosolic fractions were separated by centrifugation and nuclei were lysed after repeated washing with an SDS-containing lysis buffer. Equivalent protein amounts from cytosolic and nuclear fractions were loaded on SDS-PAGE gels and analyzed with Western Blot. To ensure correct cellular fractionation in the Western Blot, the kinase AKT was used as a cytosolic and the acetyl-histone-H4 as a nuclear control. These showed a slight contamination of the nuclear samples with cytosolic protein, but cytosolic samples appeared very clean of nuclear proteins.

For DRR1 wt more than half of the protein signal was detected in the nuclear sample. The mutants dPEPE and C94A showed a similar distribution pattern between cytosol and nucleus. In contrast, dN, dM and M mutants showed a lower signal in the nucleus and a stronger signal in the cytosol. The biggest divergence in comparison to the wt was found for the mutant dC: the nuclear signal was strongly reduced and about 90% of the protein appeared to be localized in the cytosol (Figure 24). All mutants include the putative

nuclear localization signal from human DRR1, except for the dM mutant which lacks the region from amino acid 64 to 94 and therefore would miss the first five amino acids of the NLS. However, this putative NLS does not seem to be decisive for nuclear localization of ectopic DRR1 in HEK-293 cells.

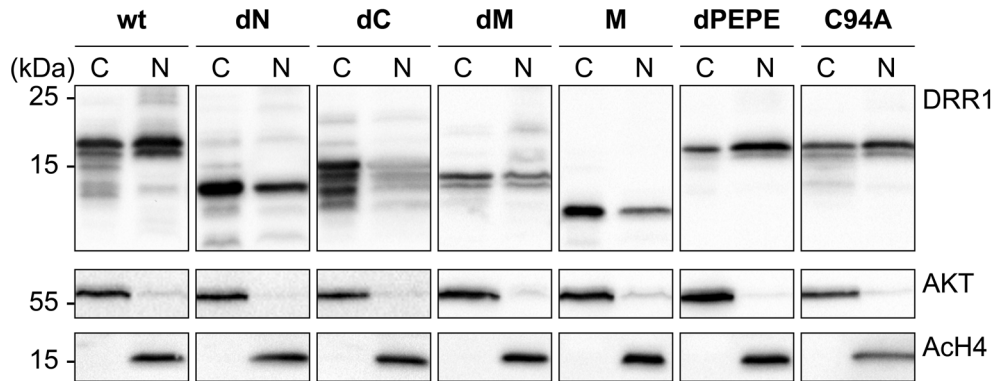


Figure 24. DRR1 wt and all mutants localize to the nucleus in HEK-293 cells. Cytosolic and nuclear fractions of cells expressing ectopic DRR1 wt or mutants were analyzed by SDS-PAGE and Western Blot. Clean fractionation of cytosol (C) and nucleus (N) was confirmed with antibodies against the cytosolic kinase AKT and the nuclear acetyl-histone H4. Representative Western Blots are shown.

4.2.4. DRR1 binds and increases F-actin in cells

Colocalization of DRR1 and F-actin in HeLa cells

Functionally interacting proteins are often organized in cellular clusters. For DRR1, localization along stress fibers, membrane ruffles and other actin-rich structures had been shown previously (Le et al., 2010; Schmidt et al., 2011). The colocalization of DRR1 with actin in cultured HeLa cells was therefore analyzed and quantified for each mutant.

HeLa cells ectopically expressing DRR1 for 24 h were fixed and nuclei stained with DAPI, F-actin was stained with phalloidin and DRR1 with specific antibody. Quantification of colocalization was performed using whole cells as regions of interest (ROI) and Pearson's correlation coefficient (PCC) was calculated in *ImageJ* with the plugin "Coloc2". The PCC is a standard and well-established procedure for measuring the degree of overlap (Adler and Parmryd, 2010; Manders et al., 1992). The test of significance of the PCC was performed by randomization of the image (Costes et al., 2004). In contrast to other colocalization measures, the PCC is independent of the gain and offset of the image and measures correlation. Thereby, it reflects direct or indirect dependency of the two intensities.

Representative HeLa cells are shown in Figure 25. The PCC with the number of cells used for quantification (n, from two independent experiments), the standard error of the mean (SEM) and the squared PCC (PCC^2) are shown in Table 1. In this table, the mutants

were ordered by descending PCCs for easier estimation of the relative colocalization. Although the interpretation of the PCC is not straight forward, as a rule of thumb, a $PCC > 0.4$ can be regarded as a strong positive correlation. DRR1 wt, dN, dC, dM, dPEPE and C94A had PCCs above 0.4. This colocalization was mainly derived from stress fibers and filopodia as visually assessed. The non-actin binding mutant M was the only one to show a weak correlation with a $PCC < 0.3$.

The coefficient is the ratio between the covariance of the channels and the product of their standard deviations. Hence, the squared value of the PCC is the percentage variance in the actin channel that can be explained by alterations in the DRR1 channel, and *vice versa* (Dunn et al., 2011). For DRR1 wt, the PCC^2 indicates about 30% of covariance between F-actin and DRR1.

DRR1	PCC	N	SEM	$PCC^2 \pm SEM$ (%)
wt	0.543	14	0.0432	29.5 ± 4.32
C94A	0.561	7	0.0904	31.5 ± 9.04
dM	0.52	10	0.0376	28.3 ± 3.76
dN	0.500	14	0.0335	25.0 ± 3.35
dC	0.453	15	0.0462	20.6 ± 4.62
dPEPE	0.446	12	0.0856	19.9 ± 8.56
M	0.268	7	0.0813	7.2 ± 8.13

Table 16. Colocalization parameters of DRR1 and actin.

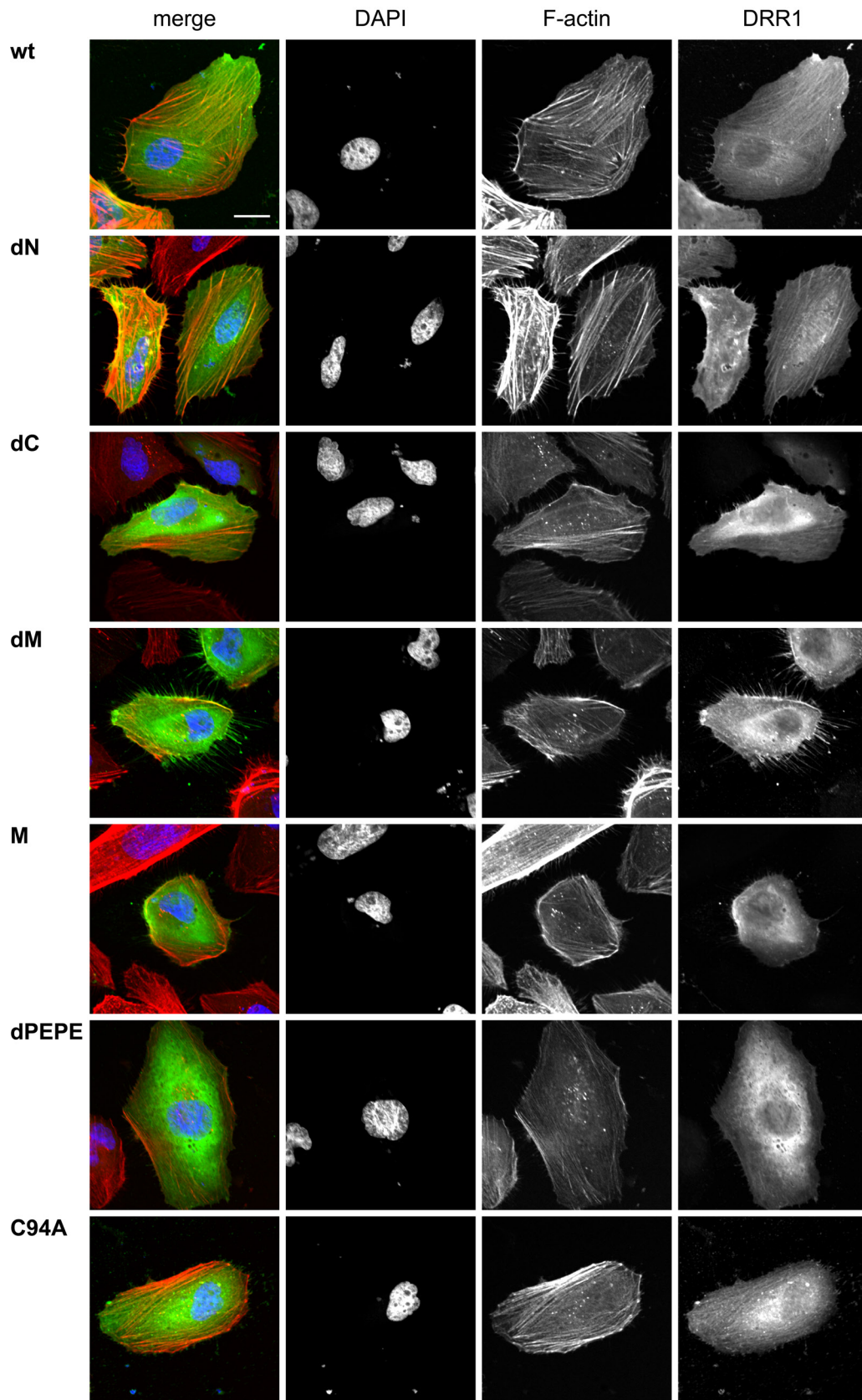
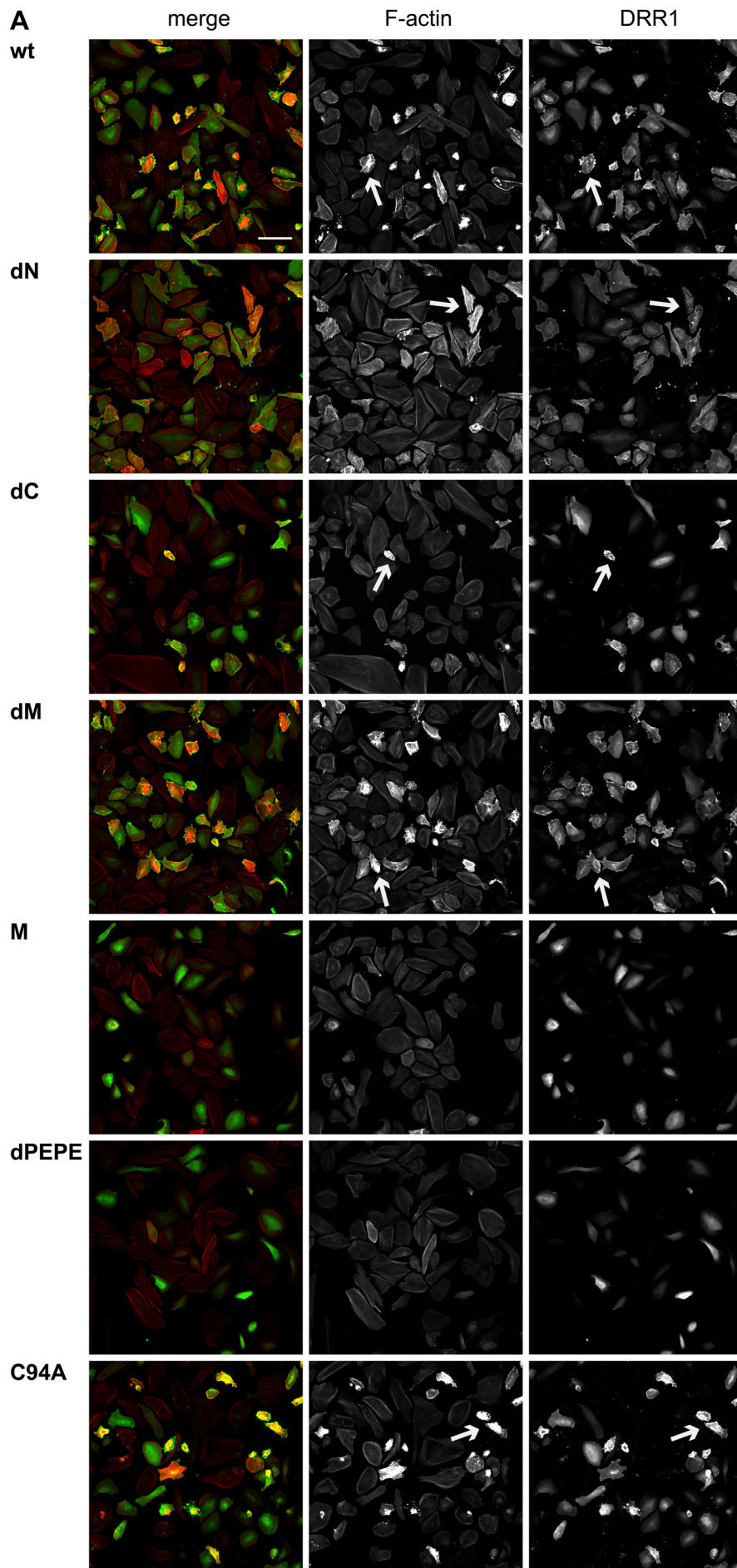


Figure 25. DRR1 wt and dN localize along actin stress fibers in HeLa cells (continued from previous page). HeLa cells were transfected with DRR1 plasmids or empty vector as a control and fixed 24 h after transfection. Nuclei were stained with DAPI (blue), F-actin with phalloidin (red) and DRR1 with specific antibody (green). Images were taken with a confocal microscope (40x/1.15 NA objective, 3x zoom). Representative cells are shown. Scale bar denotes 20 μm .

Increase of mean cellular F-actin in DRR1-expressing cells

HeLa cells ectopically expressing DRR1 could in fact be identified within the actin fluorescence channel, as they often showed a stronger phalloidin staining indicating a higher amount of cellular F-actin. This observation led to the quantification of the mean F-actin per cell. HeLa cells were transfected with DRR1 plasmids (or empty vector control) and fixed after 24 h. F-actin was stained with fluorophore-labeled phalloidin and DRR1 with a specific antibody. Images were taken with a confocal microscope (Figure 26A). Quantification was performed in *ImageJ* by measuring the mean gray value of each cell in both channels, actin and DRR1. Transfected cells were defined with a gray value of > 500 (in a 16-bit image), and the mean gray value in the actin channel of transfected cells was normalized to the mean gray actin value in control cells. For each condition, 30-200 cells from 5-10 images were analyzed.

The amount of F-actin per cell in DRR1 wt-transfected cells was more than three times higher than in the control. The mutants dM and C94A increased the amount of F-actin about three times, while dN increased F-actin about two times in comparison to the control. The other mutants, dC, M and dPEPE showed no significant increase of F-actin (Figure 26B). Together with the data from *in vitro* experiments this leads to the suggestion that all three molecular effects of DRR1 contribute to the higher amount of F-actin in cells with DRR1 overexpression: bundling, capping and nucleation. The mutant dM shows the second highest increase in F-actin after the wt, in spite of lacking bundling activity. Thus, the increase is likely mediated by enhanced nucleation and capping. The C94A mutant exerts the same tripartite effect as the wt although less pronounced, and consequently the F-actin in the cell is increased to a slightly lower extent than in the case of DRR1 wt overexpression. Finally, the mutant dN still increased F-actin two-fold, although it does neither cap nor nucleate, indicating that the bundling activity of dN is stabilizing F-actin, and results in an increase of cellular F-actin. The mutants M and dPEPE had no effect on actin network structure and didn't alter F-actin as expected, while the mutant dC only generated amorphous bundles that didn't result in stabilization of F-actin within the cell.



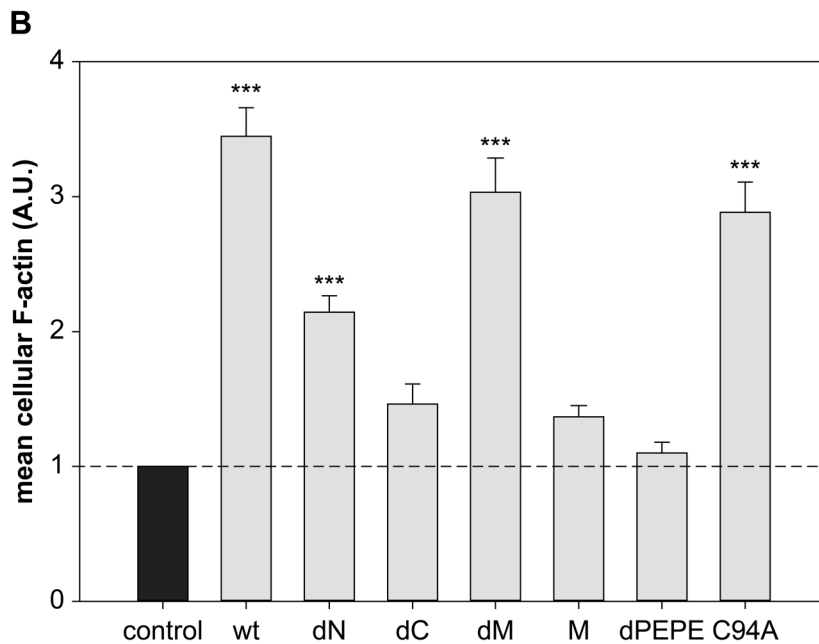


Figure 26. Mean F-actin per cell is increased with DRR1 wt, dN, dM and C94A overexpression. (continued from previous page). HeLa cells were transfected with DRR1 plasmids or empty vector as a control and fixed 24 h after transfection. (A) F-actin was stained with phalloidin (red) and DRR1 with a specific antibody (green). Images were taken with a confocal microscope (20x/0.4 NA objective). Scale bar denotes 100 μ m. White arrows indicate exemplary cells with increased F-actin correlating with high DRR1 wt or mutant expression. (B) Quantification of mean cellular F-actin was performed in *ImageJ* and values of transfected cells were normalized to untransfected cells in the same image (n = number of cells in one experiment, control n = 200, wt n = 102, dN n = 93, dC n = 38, dM n = 54, M n = 52, dPEPE n = 35, C94A n = 85). Bars represent means + SEM. *** p < 0.001 in comparison to control. Statistical analysis was performed with one-way ANOVA and Bonferroni *post hoc*.

Activation of the serum-response factor upon DRR1 overexpression

To explore the consequences of DRR1's effect on actin dynamics further, we made use of the fact that the transcription factor serum response factor (SRF) is activated or inactivated via its cofactor MAL in response to alterations of the G-/F-actin equilibrium (Posern and Treisman, 2006). Bound to G-actin, MAL-translocation to the nucleus is inhibited and SRF consequently not activated. With increasing amounts of F-actin, however, MAL detaches from G-actin and activates SRF after translocation. In order to verify the increased amount of F-actin in DRR1 overexpressing cells, we chose SRF as a reliable and functionally relevant read-out.

Dual-luciferase reporter gene assays were performed with the SRF reporter plasmid 3DA.luc and gaussia luciferase for normalization of transfection efficiency. HEK-293 cells were transfected with the two reporter plasmids and the plasmids expressing DRR1, mutants or empty vector. The nucleator mDia lacking its autoinhibitory "DAD"-region was used as a positive control for SRF activation. Stimulation of SRF was performed with 20% serum for 16-18 h.

The results of the SRF reporter gene assays reflect the increase in F-actin quantified from cellular stainings (Figure 27). In serum-stimulated cells, DRR1 wt increased SRF activity about 10fold in comparison to control cells and similarly to the effect of mDia. In the absence of serum the stimulation was still about 8fold above the serum-stimulated control sample and similar to the unstimulated mDia sample, indicating strong SRF activation by DRR1 independently of serum. The mutant dN also strongly increased SRF activity in a similar way as the wt, indicating that bundling does indeed have a strong effect on F-actin stabilization. And finally, the mutants dM and C94A showed an increase in SRF activity, although not as pronounced. Nevertheless, the analogous results from cellular stainings and SRF reporter gene assays strongly support the stabilization of F-actin in the cell by the tripartite effect of DRR1 by capping, nucleating and bundling.

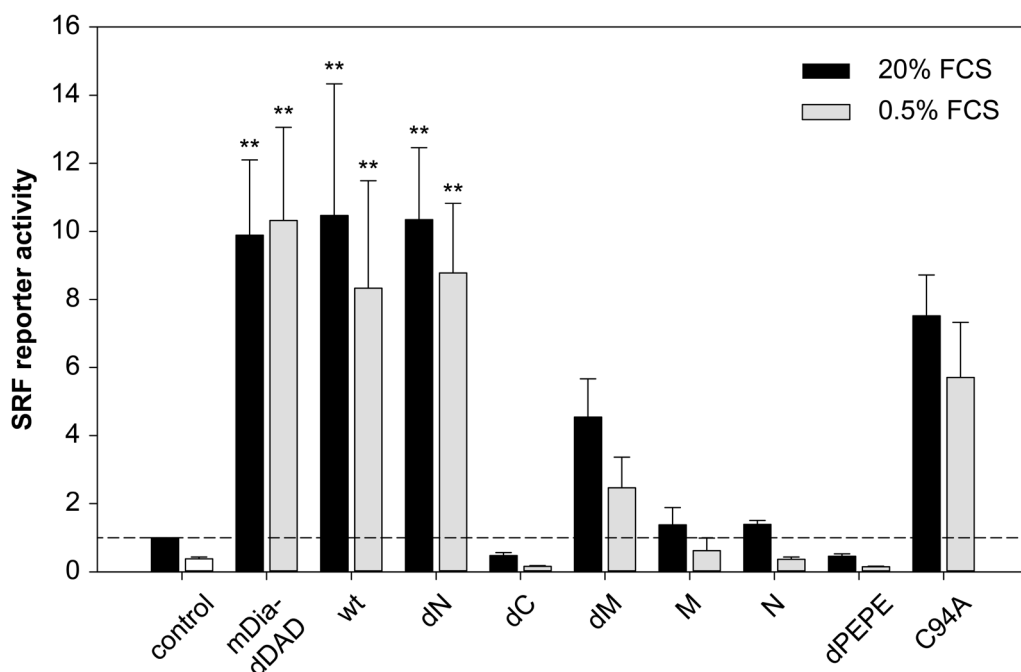


Figure 27. DRR1-dependent increase in cellular F-actin leads to a strong activation of the serum response factor (SRF). SRF reporter gene assays in HEK-293 cells show 8-10fold enhanced SRF activity after overexpression of DRR1 wt, dN or C94A with and without serum ($n = 5$). Cells were transfected with the SRF reporter 3DA.luc, the gaussia luciferase vector for normalization of the luciferase signal and the indicated plasmids or empty vector as a control. Serum stimulation or withdrawal was performed for 16-20 h. Luciferase activity is shown as the fold-increase of serum-stimulated control samples. Bars represent means + SEM. *** $p < 0.001$ in comparison to control. Statistical analysis was performed with one-way ANOVA and Bonferroni *post hoc*.

Effects of Cytochalasin D on DRR1-overexpressing cells

Several compounds can alter the actin structure in the cell, including depolymerizing agents like cytochalasins. As explained in chapter 4.1.3., cytochalasins are a class of organic molecules originally isolated from *fungi*, with Cyto D being the most potent one. Cyto D triggers depolymerization of F-actin by capping, cleaving barbed ends and acceleration of the actin assembly kinetics (Sampath and Pollard, 1991; Urbanik and Ware, 1989). In the model of DRR1's molecular mechanism DRR1 is assumed to bind to the side of the filaments for bundling, but also to the barbed ends thereby inhibiting the addition of new monomers. Thus, Cyto D and DRR1 could have competing or partially overlapping binding sites on the filament's barbed ends.

To test this scenario, HeLa cells were transfected with DRR1-expressing plasmids for 24 h and treated with 2 μ M Cyto D for 2 h prior to fixation. After staining with DAPI, phalloidin and DRR1 antibody, the cells were analyzed with the same two approaches as used above: the PCC to quantify colocalization of F-actin and DRR1, and the mean F-actin content in transfected cells (normalized to untransfected cells) via the mean gray values in the respective channel.

Prior to Cyto D treatment, the colocalization of DRR1 was reflected by a PCC of 0.543 (see Table 16). After Cyto D treatment, the F-actin structure in HeLa cells was dramatically altered: no actin stress fibers were left, the cells started to round up and the phalloidin-staining showed a punctuate pattern. The distribution of DRR1 within the cell was changed in a similar way resulting in a punctuate pattern throughout the cytosol (Figure 28A). Interestingly, the PCC for DRR1 wt and F-actin in Cyto D-treated cells was significantly increased in comparison to untreated cells overexpressing DRR1 (Figure 28B). Although no conclusion can be drawn about G-actin binding of DRR1, the concurrent alteration of the cellular distribution pattern of DRR1 and actin upon depolymerization of F-actin corroborates a preferential binding of DRR1 to F-actin within the cell.

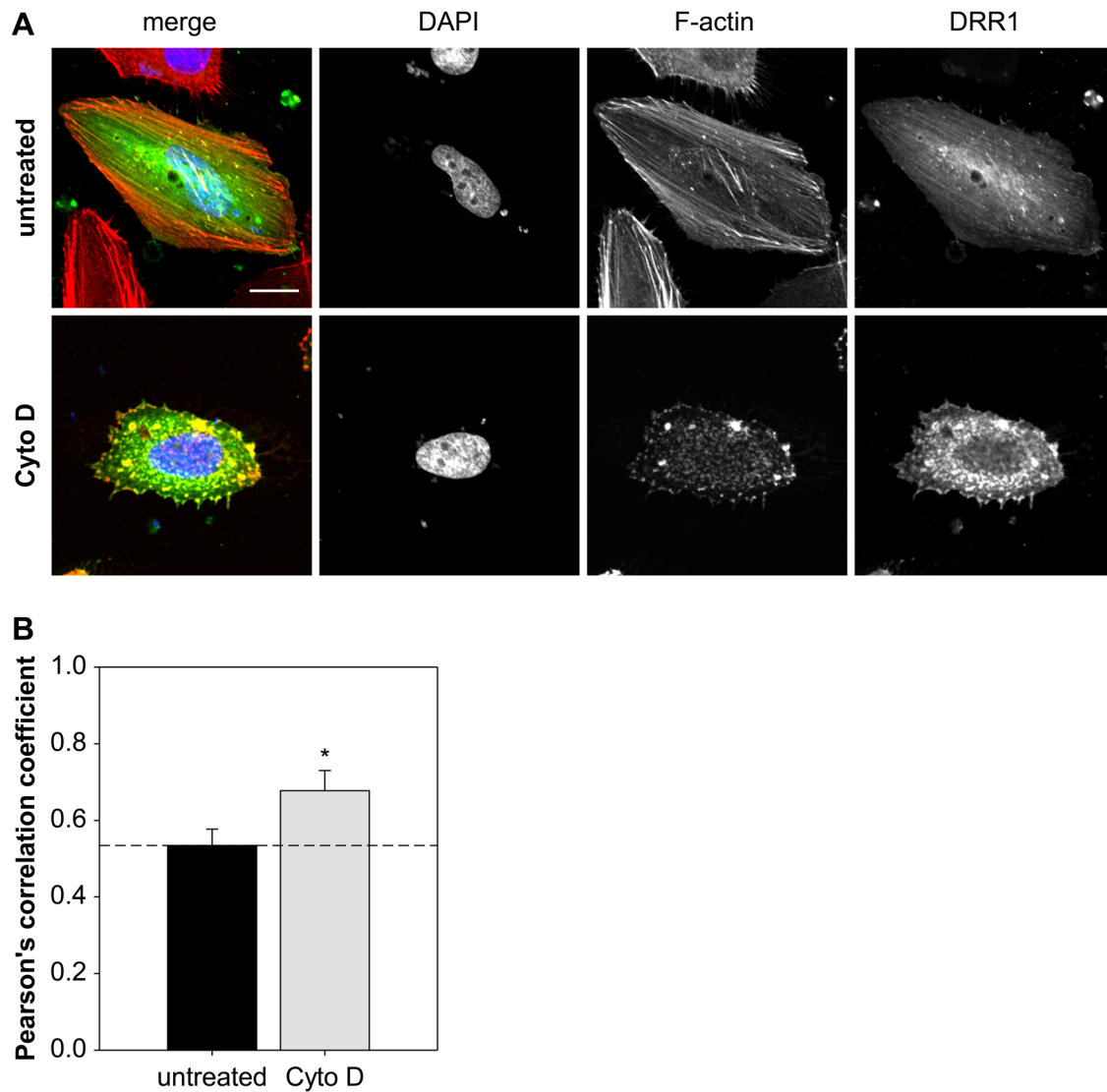


Figure 28. DRR1 colocalization with F-actin is increased in HeLa cells treated with Cytochalasin D. HeLa transfected with DRR1 for 24 h were treated with 2 μ M Cyto D for 1 h before fixation. The cells were stained with DAPI (blue), phalloidin (red) and DRR1-antibody (green). (A) Images were taken with a confocal microscope (40x/1.15 NA objective, 3x zoom). After treatment with Cyto D, DRR1's cellular distribution appears similar to the punctate pattern of F-actin. Representative cells are shown. Scale bar denotes 20 μ m. (B) Quantification of colocalization with Pearson's correlation coefficient. Pearson's correlation coefficient (no threshold) was calculated in *ImageJ* using a PSF of 4.25 and running 100 Costes randomizations (untreated $n = 14$ cells, Cyto D $n = 9$ cells). Bars represent means + SEM. * $p < 0.05$ in comparison to untreated control. Statistical analysis was performed with a two-tailed t-test.

As a next step we measured the mean cellular F-actin in cells treated with Cyto D in the same way as described above. Indeed, the amount of F-actin in cells ectopically expressing DRR1 was still higher than in control cells after Cyto D treatment. Moreover, there was about three times more F-actin in ectopic DRR1 expressing cells than in untransfected cells within the same sample (used as control), according to the results from untreated HeLa cells (Figure 29, compare with Figure 27). A very strong positive correlation was found between the amount of F-actin and the amount of overexpressed DRR1 with a

correlation factor of $r > 0.8$ (Figure 29C). Altogether, these data support the model of DRR1 binding to barbed ends and thereby protecting the filaments against Cyto D-induced depolymerization. Presumably, DRR1 might compete with Cyto D at the barbed end.

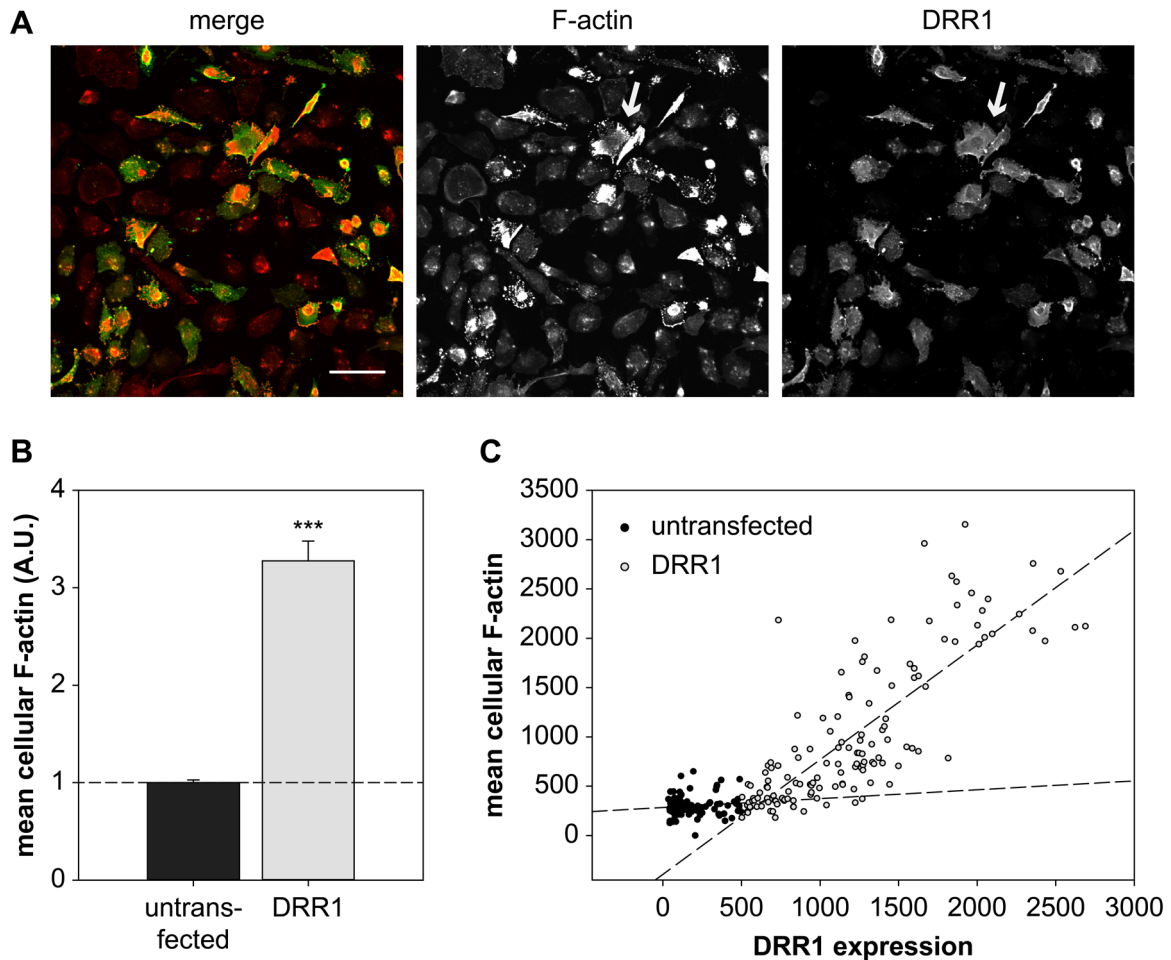


Figure 29. DRR1 stabilizes F-actin in HeLa cells treated with Cytochalasin D. HeLa transfected with DRR1 wt for 24 h were treated with 2 μ M Cyto D for 1 h before fixation. (A) The cells were stained with DAPI (blue), phalloidin (red) and DRR1-antibody (green). Images were taken with a confocal microscope (20x/0.4 NA objective). Scale bar denotes 100 μ m. White arrows indicate exemplary cells with increased F-actin correlating with high DRR1 expression. (B) Mean F-actin content in DRR1 expressing cells vs. untransfected cells is increased, suggesting a protection of F-actin against Cyto D-induced depolymerization by DRR1. Quantification of mean cellular F-actin was performed in *ImageJ* and values of transfected cells were normalized to untransfected cells in the same image (n = number of cells in one experiment, untransfected n = 118, DRR1 n = 138). Bars represent means + SEM. *** $p < 0.001$ in comparison to untransfected control. Statistical analysis was performed with a two-tailed t-test. (C) The amount of F-actin per cell correlates with DRR1-expression. Values for mean cellular F-actin (phalloidin fluorescence) and DRR1 expression (antibody fluorescence) correspond to the gray scale of a 16-bit image. For DRR1-transfected cells, Pearson's correlation indicates a strong positive correlation with cellular F-actin ($r = 0.813$, $p = 9.862E-34$).

4.2.5. DRR1 modulates actin-dependent processes in cells

DRR1 reduces HeLa cell spreading

The results obtained from fixed cells clearly indicated a functional impact of DRR1 on actin dynamics. In order to deepen these findings, experiments with living HeLa cells were performed to analyze actin-dependent processes.

As a first approach, cell spreading on fibronectin-coated surface was chosen as a simple read-out for changes in actin dynamics. Cell spreading is a relevant aspect in many cellular functions, such as migration or wound healing. During the initial phase of cell adhesion to the substrate, the cell shows a round morphology analogous to a drop of oil falling onto a surface. During this phase, the stiffness or viscosity of the cell has a major impact on the speed of spreading, meaning that for example a heavily bundled actin network will slow down spreading in contrast to a more filamentous network. After attachment of the cell to the surface, the second and longer phase of spreading is characterized by the extension of protrusions and eventually cell polarization. Thereby, filament elongation is the predominant effect together with integrin-mediated adhesion (Berrier and LaFlamme, 2005; Chamaraux et al., 2005; Yauch et al., 1997).

Spreading of HeLa cells on fibronectin was analyzed by transfecting them with DRR1 fused to EGFP for 24 h, replating on a fibronectin-coated surface and fixation after 30 min of spreading. In order to analyze the actin structure and quantify the cell area, F-actin was stained with phalloidin. Representative cells of the spreading assay are shown in Figure 30A. The experiment was reproduced with untagged DRR1 leading to the same results. Quantification was performed in *ImageJ* measuring 50-200 cells from four independent experiments (including the one with untagged DRR1). The control was performed with untransfected and EGFP-transfected cells. EGFP transfection did not alter spreading in comparison to untransfected cells.

DRR1 wt strongly reduced spreading of HeLa cells: while control cells showed a mean size of about $700 \mu\text{m}^2$, DRR1 wt expressing cells had a mean cell size below $500 \mu\text{m}^2$. In addition, control cells expressing EGFP showed extension of filopodial protrusions after 30 min of spreading, while DRR1 wt expressing cells were still rounded up lacking any protrusions. Together with the observed colocalization of DRR1 wt and F-actin at the edge of the cells, where the filaments barbed ends are orientated, the conclusion can be drawn that DRR1 indeed caps filaments thereby inhibiting extension of protrusions during spreading. All mutants except M also inhibited cell spreading, indicating that both, bundling and capping by DRR1, reduce spreading. Interestingly, the mutant dC had a pronounced effect in this assay similar to the wild type. Taken the results of the *in vitro* assays into consideration, the inhibition of cell spreading by the mutants dN and dC can likely be attributed to bundling, while for dM it is the capping effect. As both mutants

reduced spreading in a very similar way, it is likely that both effects contribute about equally to the spreading process.

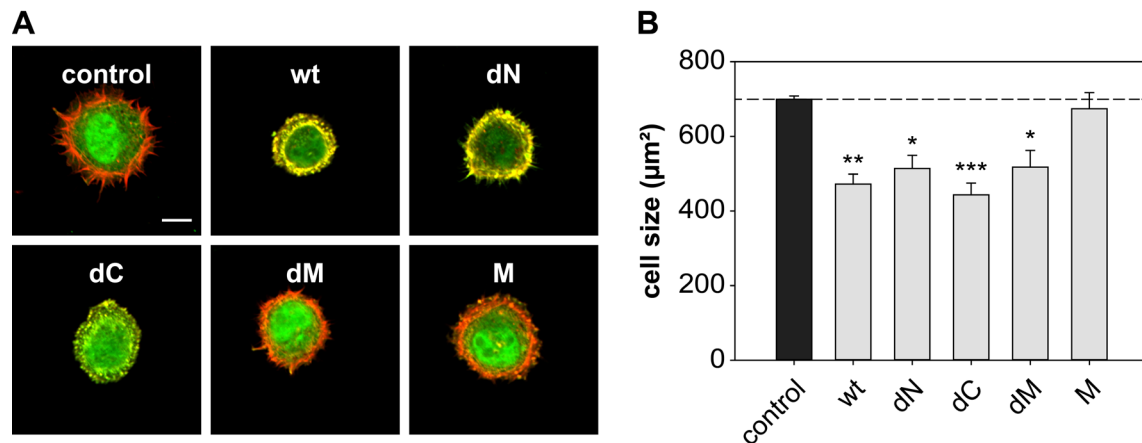


Figure 30. DRR1 wt and all mutants except M reduce spreading of HeLa cells on fibronectin. Cells were transfected with constructs expressing DRR1 wt or mutants fused to EGFP and replated on fibronectin. After 30 min of spreading, cells were fixed and F-actin was stained with phalloidin. (A) Representative cells are shown (DRR1: green, F-actin: red). (B) Quantification of cells size was performed in *ImageJ* (n = 4, 50-200 cells in each experiment). Scale bar denotes 20 µm. Bars represent means + SEM. * p < 0.05, ** p < 0.01, *** p < 0.001 in comparison to control. Statistical analysis was performed with one-way ANOVA and Bonferroni *post hoc*.

Fluorescence recovery after photobleaching of GFP-actin is reduced in DRR1-overexpressing cells

DRR1 slowed down actin polymerization *in vitro* and stabilized F-actin, suggesting these functions to have an effect on actin treadmilling in cells. In order to prove this hypothesis, fluorescence recovery after photobleaching (FRAP) of GFP-labeled actin was measured in HeLa cells co-expressing DRR1 (or empty vector as a control) for 24 h. Time-lapse images were acquired with a confocal microscope during 5 min (5 frames were recorded pre-bleach). Recovery was quantified in *ImageJ*.

After 5 min, the recovery in control cells (co-expressing empty vector) reached about 80% of the pre-bleach fluorescence. In DRR1 wt overexpressing cells, however, the recovery reached less than 60%. None of the mutants analyzed had an effect on FRAP, except dN, which had an only slightly higher recovery than the wt. These findings indicated that DRR1 slows down actin treadmilling in cells mainly by bundling actin filaments.

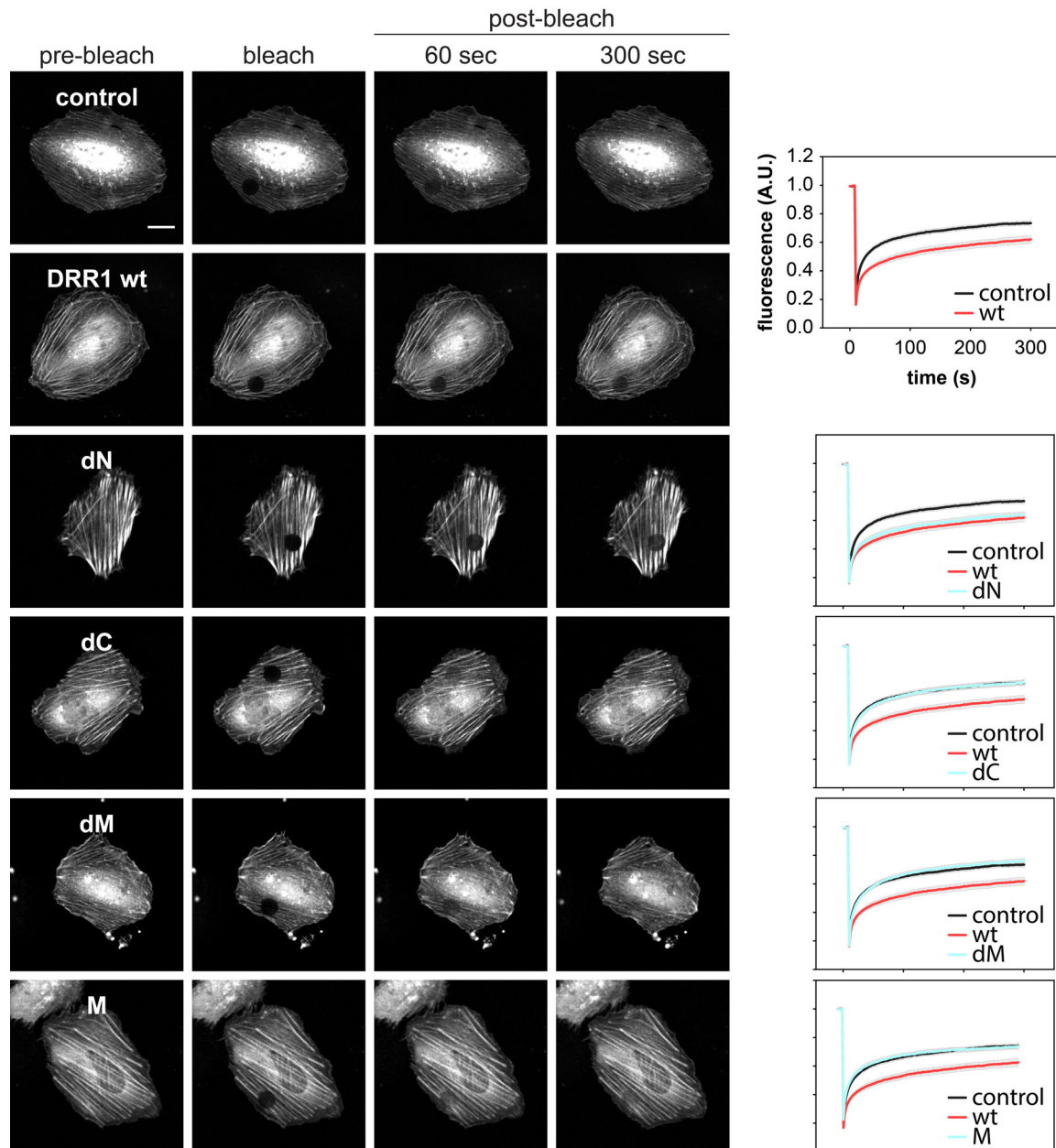


Figure 31. DRR1 wt and the mutant dN slow down actin treadmilling in HeLa cells. Fluorescence recovery after photobleaching (FRAP) in HeLa cells co-transfected with GFP-actin and DRR1 wt, dN, dC, dM and M was analyzed. Representative cells are shown. Quantification was performed in ImageJ ($n = 25-30$ cells from 2-3 independent experiments). Scale bar denotes $20 \mu\text{m}$. Scales of the graphs are all similar to the upper one (Y axis: fluorescence [A.U.], X axis: time [s]).

4.2.6. DRR1 is located at post-synaptic spines

As a first step to characterize the function of DRR1 in neurons, the localization of ectopic DRR1 in mature primary hippocampal neurons from mice was analyzed. Transfection of neurons was performed on DIV10, and on DIV21 neurons were fixed and immunostained with antibodies directed against DRR1. Images were acquired on a confocal microscope.

DRR1 showed a pronounced location in axons and dendrites of mature neurons, with a particular accumulation at spine heads. Moreover, many enlarged dendritic spines showed a very strong DRR1 signal within the head, while the necks appeared to lack DRR1 (Figure 32). These findings suggest a role of DRR1 in regulating the actin structure and related processes in mature dendritic spines, although an additional role in presynaptic mechanisms cannot be excluded.

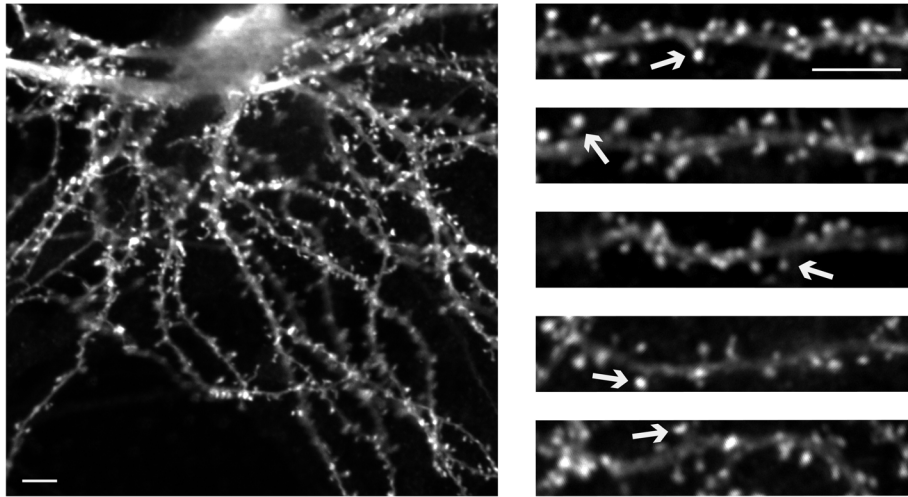


Figure 32. DRR1 localizes to dendrites and dendritic spine heads. Mouse hippocampal neurons show a strong localization of DRR1 along dendritic shafts and spines, with a remarkable accumulation at the spine heads (marked with white arrows). Neurons were cotransfected with EGFP and DRR1 on DIV10, fixed on DIV21 and immunostained with DRR1. Images were taken with a confocal microscope (60x/1.2 NA objective). Scale bars denote 5 μ m.

5. Discussion

It has become evident, that actin dynamics are a major player in synaptic transmission and plasticity. The stress-inducible gene DRR1 has emerged as a novel molecular candidate translating the stress response to changes on the actin cytoskeleton and behavior. On the other side, antidepressants have been shown to impact on the cytoskeleton and a “disturbed cytoskeletal theory” of mood disorders has been proposed. In this study, a two-pronged approach was taken to analyze the modulation of actin dynamics during stress and upon treatment with antidepressants. Three antidepressants – clomipramine, doxepin, and citalopram – were assessed in various *in vitro* assays of actin dynamics, showing that only clomipramine had a slight effect in slowing down polymerization. On the other hand, the molecular mechanism of DRR1 was revealed to be tripartite, hence raising interesting further questions about its specific effect at the synapse.

5.1. Antidepressants effect on actin dynamics

Of the three antidepressants tested in this study – clomipramine, doxepin, and citalopram – only clomipramine was shown to impact on actin dynamics. It moderately slowed down actin polymerization, presumably by reducing nucleation, but without affecting single filament elongation. The slowdown of polymerization was found for α - and β -actin in the pyrene-assay, and reproduced for α -actin in a label-free approach with macrorheology. Thus, an unspecific interaction with pyrene or quenching of its fluorescence can be excluded. For this effect, at least a two-fold excess of clomipramine over actin was required *in vitro* and became pronounced at a ten- or twenty-fold excess. While neither single filament elongation nor nucleation were reduced at a two-fold excess of clomipramine over actin, at a fifty-fold excess nucleation appeared to be reduced to roughly 60% of the control. Further indication for an effect of clomipramine on nucleation was derived from the observed prolongation of the initial lag-phase of the polymerization monitored in the macrorheology.

The amphiphilic clomipramine and other tricyclic antidepressants have been previously shown to interact with human serum albumin in the blood albeit with high interindividual differences (Braithwaite, 1980; Taboada et al., 2004). Moreover, physiologic concentrations of small cations, polycations or basic polypeptides have been shown to promote actin filament bundling based on the negative charge of G- and F-actin at physiological pH and thus without the need for specific binding sites (Tang and Janmey, 1996). These findings suggest that clomipramine could be electrostatically bound to G-actin or to short filaments, thereby interfering with either the nucleation or the addition of new monomers to the barbed end. However, this hypothesis remains to be tested further.

Clomipramine did not appear to have an effect on the structure or elastic properties of reconstituted actin networks. Neither the rheological measurements of the elastic modulus G' over a frequency range nor the confocal images of actin networks showed significant differences upon addition of clomipramine even at high concentrations. A slight increase of G_0 (G' of 0.01 Hz) was observed, although it seems to be negligible in comparison to known effects of ABPs. For example, for a filamin/actin network, the increase of G_0 from $R = 0$ to 0.1 raises over almost one order of magnitude (Schmoller et al., 2009). For fascin, the increase in G_0 is even higher (Lieleg et al., 2009).

Whether the concentrations at which clomipramine exerts an *in vitro* effect on actin assembly are relevant for cellular processes, is yet to be analyzed. Concentrations of above 20 μM and even up to 40 μM have been estimated in the brain after 5 weeks of treatment with the antidepressant fluoxetine, and the tricyclic antidepressant amitriptyline was found in the brain of mice in a concentration range of 10-20 μM (Bolo et al., 2004; Henry et al., 2005; Uhr et al., 2007). Clomipramine did not show any effects on actin-dependent cellular processes at the commonly used 10 μM concentration or even at up to 20 μM . The overall F-actin structure of astrocytes and two-dimensional migration of HeLa cells were unaffected by clomipramine at 15 μM . It strongly reduced HeLa cell spreading at 50 μM similar to the actin depolymerizing agent Cyto D. However, this effect was exerted only at this very high concentration and must therefore be interpreted with caution, as unspecific toxic effects – as observed in cellular F-actin stainings at high concentrations – might be involved.

5.2. Molecular effect of DRR1 on actin dynamics

Domain mapping is a frequently followed approach to better understand the mechanism of action of proteins. Here, several *in vitro* experiments with full-length and truncated mutants helped to elucidate the molecular mechanism of DRR1. Two actin binding regions were identified separated by a central non-binding region. Given the known conservation of DRR1 among species, these binding regions can consequently be narrowed down within

the “conserved domain of unknown function”. Thus, the N-terminal binding region is contained in amino acids 16 to 60, while the C-terminal one lies within amino acids 113 to 133. The identified actin binding regions in DRR1 lack any homology with known actin binding motifs.

	BINDING	CAPPING	NUCLEATION	BUNDLING
DRR1 wt	+++	+++	+++	+++
dN	+++	0	0	+
dC	+	0	0	+
dM	++	+++	++	+
M	0	0	0	0
N	+	0	0	0
dPEPE	+	0	+++	0
C94A	++	+++	++	++

+ *enhancement*, - *decrease*, 0 *no effect*

Table 17. Schematic overview of DRR1’s molecular effects on actin dynamics.

The central region (amino acids 61 to 112) contains a predicted coiled coil (amino acids 66-93) and presumably mediates homodimerization of DRR1 at the actin filament. Interactions with other proteins could possibly also be mediated by this region. An overview of the results of *in vitro* actin dynamics with the mutants of DRR1 is shown in Table 17.

It was demonstrated that actin bundling by DRR1 is mediated via the two actin binding regions both as a monomer and potentially as a dimer with four actin binding regions. Dimerization of DRR1 through the middle domain (M) is essentially supported by the observation that the N-terminally truncated DRR1 with only one actin binding domain (dN) forms proper bundles in actin networks. Conversely, addition of the non-actin binding middle domain interferes with proper bundling by full-length DRR1. The actin bundles formed in the presence of DRR1 appear to be similar to bundles formed by α -actinin with respect to bundle thickness and length, and mesh size of the bundled network (Falzone et al., 2012). Comparing the data on assembly kinetics of bundled networks reveals that at ratios of α -actinin:actin around 1:1 the bundle structure appears highly similar to the bundles by DRR1 at a ratio of 1:2 (Falzone et al., 2012 and this work). This comparison suggests DRR1’s bundling activity to be at least as strong as the respective effect of α -actinin, presumably even more efficient. Meanwhile, actin bundling proteins have been demonstrated to inhibit depolymerization of actin *in vitro* at similar concentrations as used in this study (Schmoller et al., 2011). Accordingly, DRR1 has also been shown to inhibit dilution-induced actin depolymerization at a DRR1:actin ratio of 0.7, very likely through actin bundling (Schmidt et al., 2011).

Both actin binding sites of DRR1 are necessary for capping actin filaments, as only mutants retaining both actin binding regions (wt, dM and C94A) were able to inhibit single filament elongation. Most capping proteins seem to cap at a nanomolar range, and both the binding regions and capping mechanisms are not conserved (Hertzog et al., 2010). For example, gelsolin caps actin filament at gelsolin:actin ratios of 1:20 to 1:80 (Gremm and Wegner, 2000). Capping protein, which is the dominant capping protein *in vivo*, caps with very high affinity and is effective at ratios of 1:1,000 (Schirenbeck et al., 2005). While the precise K_D of actin capping by DRR1 remains to be analyzed, it seems to have a similar potency as other capping proteins, as estimated by the notable capping effect of DRR1 at a ratio with actin of 1:10. However, it is by far not as effective as capping protein.

Further experiments are required to determine whether the three effects of DRR1 – bundling, capping, and nucleation – are independent of each other. All evidence suggests bundling and capping to be independent. The comparison of actin networks at a DRR1:actin ratio of 1:10 with the respective capping effect shows that there are only few bundles visible, but filament elongation rate is strongly reduced to about 30% of the control. In addition, the mutant dM shows strong capping ability similar to the wt, while it hardly generates any bundles or even clusters of F-actin in the networks. Moreover, due to the experimental setting of actin filaments bound to the surface via heavy mero-myosin when visualizing polymerization by confocal microscopy, bundling is supposed to be strongly reduced. An interesting experiment to further support barbed end capping as a novel, independent effect would be to analyze the impact of DRR1 wt (capping and bundling) and the mutant dM (only capping) in the pyrene-assay with actin and profilin. Profilin sequesters G-actin and inhibits pointed end elongation, i.e. an inhibitory effect of DRR1 on profilin-actin polymerization could only be derived from barbed end capping.

In contrast, nucleation could be a concentration-dependent effect of capping. For capping protein, a concentration-dependent nucleation activity has been demonstrated: it inhibits elongation of actin at low concentration by blocking the barbed end, while at higher concentration it promotes nucleation by mimicking a nondissociable actin dimer (Cooper and Pollard, 1985). All DRR1 mutants showing the capping effect also enhanced nucleation, with the exception of dPEPE, which enhanced nucleation but had no significant impact on filament elongation. This result suggests nucleation as an effect dependent on F-actin binding of DRR1. To further address this aspect, nucleation activity of all mutants should be further analyzed dependent on their concentration in both the pyrene-assay and the confocal polymerization.

Taken together, the exact mechanism of actin nucleation by DRR1 is unclear so far, but due to its two actin binding sites, it is conceivable that DRR1 stabilizes actin dimers (or even trimers and tetramers when dimerized) and thereby directly enhances nucleation in a

similar way to capping protein. All actin nucleators except formins exhibit the actin-binding motif WASP-homology 2 domain often organized in tandem repeats. Formins nucleate and promote barbed end elongation through their formin-homology domains (Dominguez, 2010). However, DRR1 lacks homology with these domains, suggesting a different mechanism of nucleation. In comparison to the formin mDia1, the nucleation capacity of DRR1 appears much weaker (Harris and Higgs, 2006). However, they both lead to a similar activation of SRF, indicating that the bundling and capping effects of DRR1 lead to a strong stabilization of F-actin in the cells.

The tripartite effect of DRR1 on actin dynamics is schematically depicted in Figure 33.

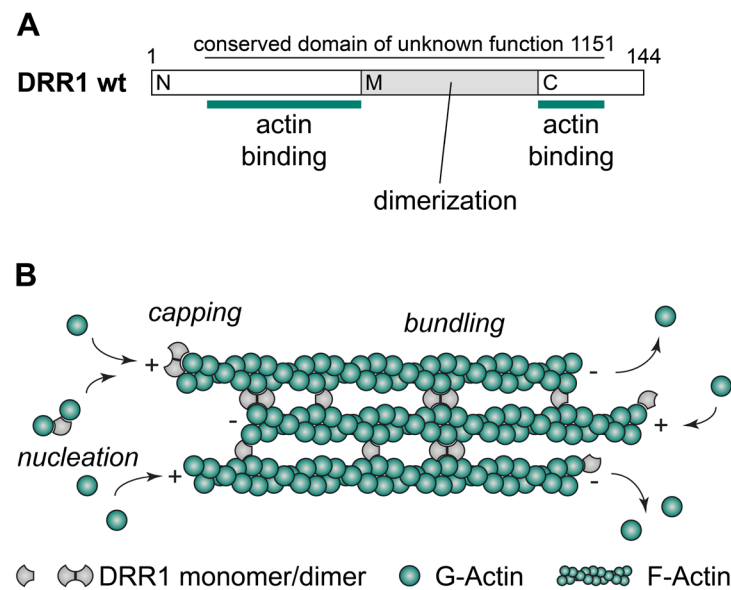


Figure 33. Model of DRR1's effects on actin dynamics. (A) Scheme of DRR1 protein (144 amino acids) containing the highly conserved domain of unknown function 1151 and domains analyzed in this work. N: N-terminal actin binding region, M: middle region containing a predicted coiled coil and potentially mediating homo-dimerization, C: C-terminal actin binding region. (B) Scheme of the molecular mechanism of DRR1 as a monomer and dimer on actin dynamics (capping, nucleation, and bundling).

Meanwhile, there are additional features worth to mention among the effects of the DRR1 mutants. First, the cysteine residue in the center of the coiled coil does not appear to have a crucial impact on any of the molecular effects. Due to the known interaction of DRR1 with Prdx1, it is tempting to speculate that this cysteine residue might be important for regulation of DRR1's functions under certain redox conditions (Schmidt et al., 2011).

For the mutant dPEPE, some results seem contradictory: it showed actin binding in the Co-IP experiment (Figure 17), but no binding in the co-sedimentation assay (Figure 18). The latter result excludes specific binding to F-actin, which is in agreement with the original publication, in which the mutant dPEPE lacked colocalization with phalloidin in cells (Le et al., 2010). In the Co-IP, however, one cannot differentiate between F- and G-actin binding, therefore suggesting the ability of this mutant to bind to G-actin. This

interpretation is further supported by the finding that the mutant dPEPE enhances nucleation potentially through interaction with G-actin, while it obviously does not inhibit filament elongation due to the lacking F-actin binding.

In a similar way, the apparent actin binding capacities of the mutants dN and dC differ somewhat between the Co-IP and the Cosedimentation experiments, although the differences are not significant (compare Figure 17 and 18). While dN shows higher actin binding than dC in the Co-IP, dC exerts higher F-actin binding in the co-sedimentation. Yet, in the presence of dN proper actin bundles are generated, while dC (same as dM) only leads to the formation of aggregate-like crosslinks. Moreover, the mutant dC shows a trend to enhance nucleation and slightly reducing elongation. These results indicate that the two actin binding regions differ in F-actin binding affinity and likely also in their G-actin binding ability. Nevertheless, additional data are required to address the specific function of each binding region.

Taken together, DRR1 shifts the equilibrium of actin polymers towards more, thicker and shorter actin bundles. The importance of these alterations for cellular mechanisms is discussed in the following chapter.

5.3. Cellular effects of DRR1

Increasing evidence supports the view that many ABPs are multifunctional, rather than exhibiting one exclusive effect on actin dynamics. For example, the protein Epidermal growth factor receptor pathway substrate 8 (Eps8), is the founding and so far unique member of a family of capping proteins, capable of filament side-binding and bundling (Croce et al., 2004; Hertzog et al., 2010). DRR1 adds to this class of multifunctional ABPs by exhibiting a tripartite effect *in vitro*: bundling, capping, and nucleation. These three effects are likely to be regulated further for example by the relative abundance of other ABPs that might compete with DRR1 for access to actin structures.

Moreover, DRR1's cytosolic and nuclear localization suggests an additional impact on nuclear actin dynamics. While the role of nuclear actin is just beginning to be understood, it has been shown to be involved in chromatin remodeling, gene transcription and cytosolic-nuclear shuttling (Castano et al., 2010). The question whether DRR1's effect on actin in the nucleus is similar or divergent from the one in the cytosol as well as its functional consequences will be a quite interesting issue for future research.

Table 18 shows an overview of DRR1 effects on actin-dependent cellular processes.

	F-ACTIN COLOCALIZATION	CELLULAR F-ACTIN	SRF ACTIVATION	CELL SPREADING	ACTIN TURNOVER
DRR1 wt	+++	+++	+++	--	---
dN	++	+	+++	-	---
dC	+	0	0	---	0
dM	++	++	+	-	0
M	0	0	0	0	0
N			0		
dPEPE	+	0	0		
C94A	+++	++	+		

+ *enhancement*, - *decrease*, 0 *no effect*

Table 18. Schematic overview of DRR1 effects on actin-dependent cellular processes.

The correlation coefficients of F-actin and the DRR1 mutants reflect the respective F-actin binding abilities. There is no colocalization of the central region M with F-actin, in line with the lack of actin binding. In contrast, the mutants dN, dC, dM, dPEPE, and C94A all exhibit colocalization with F-actin, owing to the existence of two actin binding regions separated by the central, presumably dimerizing region. Although the mutant dC showed slightly more cosedimentation with F-actin than dN *in vitro*, this is not reflected by increased F-actin colocalization in cells.

Transfection of DRR1 produced a remarkably stronger F-actin staining than the untransfected control cells, which was quantified to be about three times more. Intriguingly, for the mutants dM and C94A this effect was almost as pronounced as for the wt, while dN showed an approximately two-fold increase of cellular F-actin. These findings, together with the respective molecular effects of each mutant, suggest all three effects of DRR1 – bundling, capping, and nucleation – to contribute to the increased amount of cellular F-actin.

The experiments of HeLa cells treated with Cyto D indicated a preferred binding of DRR1 to F-actin versus G-actin, as the colocalization analysis revealed that the DRR1 staining essentially followed the remaining and reorganized F-actin structures upon Cyto D-induced depolymerization of actin. On the other hand, cells expressing DRR1 still featured more F-actin after Cyto D treatment than untransfected cells. These findings indicate that bundled F-actin is less sensitive towards Cyto D-induced depolymerization, and that actin binding sites of DRR1 might overlap with Cyto D, thereby protecting the filaments against Cyto D-induced depolymerization by DRR1-binding.

The increase in cellular F-actin caused by ectopic DRR1 was paralleled by increased activation of the serum response factor SRF, comparable to the activation of the formin mDia1. Virus-mediated overexpression of DRR1 in the hippocampus reduced spine density and LTP, while SRF was described to promote spine morphogenesis and axonal outgrowth

(Kalita et al., 2012; Schmidt et al., 2011). This seeming contradiction might be explicable by a compensatory effect of SRF in reaction to the upregulation of DRR1. In addition, SRF-dependent effects on gene-transcription might be slower than the direct and immediate impact of DRR1 on synaptic actin dynamics and thus balance DRR1's action.

HeLa cells expressing ectopic DRR1 wt reduced cell spreading to about 70% of the controls. All mutants capable of actin binding, i.e. dN, dC, and dM, showed a comparable effect. Cell spreading is a complex process affected by different parameters: substrate stiffness and density, diffusion of integrin-receptors to the adhesion patch, and actin polymerization (Chamaraux et al., 2005; Li et al., 2014; Yauch et al., 1997). Furthermore, early spreading was proposed to follow a universal law depending on the mechanical properties of the cell and predominantly the actin cortex (Cuvelier et al., 2007). The results of the mutants indicate that both, inhibition of filament elongation (by wt and dM), as well as bundling (by wt, dN, and dC, see Table 17 and 18) contribute to inhibition of cell spreading. While bundling presumably inhibits the early phase of spreading during cell-substrate contact initiation by increasing cell stiffness, capping of F-actin is likely to interfere with extension of the lamella during the later phase.

Experiments of fluorescence recovery after photobleaching with HeLa cells revealed a reduced recovery of GFP-actin in the presence of ectopic DRR1 wt or dN. It is reasonable to assume that the recovery rate of GFP-fluorescence upon photobleaching reflects the actin turnover or treadmilling rate, as the free diffusion of monomeric G-actin is by far quicker (Frost et al., 2010; Honkura et al., 2008; Star et al., 2002). In accordance with previous studies, these findings indicate a significant slowdown of actin turnover by DRR1's bundling activity (Falzone et al., 2012; Okamoto et al., 2007). Although the relevance of this effect for the stress response remains to be elucidated, it strongly implicates a considerable increase in ATP supply for the cell. Actin treadmilling was shown to be a major energy drain in the brain and estimated to consume about 50% of a neurons' ATP (Bernstein and Bamberg, 2003). Such an increase in available ATP through slowdown of actin turnover could be necessary for other vital processes of the cell like protein synthesis.

Up to date, most studies are using fibroblasts for FRAP experiments. Nevertheless, there is increasing interest in FRAP experiments analyzing dendritic spines, as these highly dynamic structures play a central role in learning and memory (Koskinen and Hotulainen, 2014; Yuste and Bonhoeffer, 2001). For DRR1, such an approach dissecting its function in dendritic spine shape and synaptic transmission would be highly interesting.

5.4. Effects of DRR1 on synaptic plasticity

Previous results from electrophysiology indicated a pre-synaptic effect of DRR1, by increasing paired-pulse facilitation likely through preventing the recruitment of synaptic vesicles to the ready-releasable pool. Moreover, while LTP was inhibited by DRR1, its F-actin stabilizing activity appeared to be important for memory retrieval and consolidation (Schmidt et al., 2011). On the other hand, DRR1 also appears to have an impact on dendritic processes and post-synaptic function, as indicated by its localization along dendrites and its strong accumulation in enlarged spine heads.

A knockdown of capping proteins in fibroblasts caused a massive increase of filopodia, while DRR1 overexpression reduced neurite outgrowth and spine density (Mejillano et al., 2004; Schmidt et al., 2011). Therefore, it is likely that DRR1's capping activity rather than actin bundling would result in the observed reduction of protrusions. Further support for this hypothesis comes from the bifunctional actin capping and bundling protein Eps8, which was shown to control dendritic spine density through its capping activity (Menna et al., 2013). However, capping activity has also been shown to be essential for enlargement of dendritic spine heads during maturation: Eps8 is recruited to the spine head during LTP to mediate spine enlargement (Menna et al., 2013). While the major driver of spine enlargement is assumed to be the branching activity of Arp2/3, a coordinated capping activity appears to be essential as well (Fan et al., 2011; Korobova and Svitkina, 2010; Wegner et al., 2008). Actin filaments in mature dendritic spines have been shown to be quite short (< 200 nm), highly crosslinked and bundled, in line with DRR1's capping and bundling effects (Frost et al., 2010; Ivanov et al., 2009; Okamoto et al., 2007; Terry-Lorenzo et al., 2005).

Altogether, a model is proposed in which DRR1 on the one hand inhibits the outgrowth of new spines, but on the other hand contributes to the stabilization and maturation of existing spines (Figure 34). It might therefore enhance structural stability concomitant with a loss in plasticity. According to the current knowledge on synaptic actin dynamics, all three molecular effects of DRR1 are in agreement with such a model (Cingolani and Goda, 2008; Hotulainen and Hoogenraad, 2010).

Moreover, hippocampal LTP is accompanied by elevated F-actin content in dendritic spines, and ongoing actin polymerization was shown to be essential for LTP induction and maintenance (Fukazawa et al., 2003). The previously described inhibition of LTP by DRR1 (Schmidt et al., 2011) could thus be explained by reduced actin turnover, as found here in the FRAP experiments of this study. Interestingly, Ca^{2+} -calmodulin-dependent protein kinase II (CaMKII) is another multifaceted effector of spine structure which was shown to bundle F-actin and to slow down actin turnover in resting spines, while synaptic activity induced detaching of CaMKII from actin and functioning as a signaling molecule

upon Ca^{2+} influx. In this way, it was proposed to mediate spine stability and enable remodeling necessary for LTP in response to activity (Okamoto et al., 2007). Taken together, this study provides further support for the model of DRR1's function in mediating stability of spines, but rendering them less dynamic for LTP at the same time.

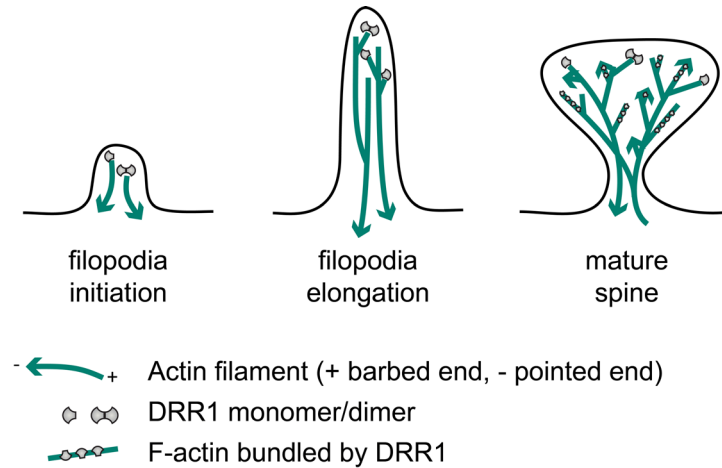


Figure 34. Hypothetical effect of DRR1 on dendritic spine maturation. During initiation of dendritic spines and extension of filopodial structures prior to maturation, elongation of actin filaments from the tip of the spines is necessary. This process would presumably be inhibited by DRR1. However, increased content of short actin filaments is necessary for spine head enlargement, mainly mediated by Arp2/3 branching activity in coordination with actin cappers. In mature mushroom spines, short filaments are highly bundled to provide stability. It is therefore likely that DRR1 could support the both spine head enlargement and the actin structure in mature mushroom spines by nucleating, capping and bundling filaments.

Another interesting notion is that DRR1 could link actin fibers with microtubules in dendritic spines. Microtubules have been proposed to enter dendritic spines and DRR1 was shown to also bind to the microtubule associated protein MAP1A (Jaworski et al., 2009; Le et al., 2010).

While molecular data acquired from this work, together with the current knowledge on spine actin dynamics, allow developing a model of DRR1's impact on dendritic spine maturation, it is essential to further test this model with additional experiments. Ideally, the tripartite effect of DRR1 should be analyzed in regard to the function of each effect for synaptic plasticity and the respective functional consequences. The implication of spine malformations in many psychiatric and neurological disorders calls for broadening the current knowledge on molecular players linking actin dynamics with synaptic transmission and behavior (Spronsen and Hoogenraad, 2010).

5.5. The function of DRR1 during stress response

DRR1 has been proposed to counteract adverse stress effects and promote coping behavior. In the adult mouse, its virus-mediated overexpression in the hippocampus improved cognitive function, while in the septum it specifically enhanced social behavior (Masana et al., 2014; Schmidt et al., 2011). This study provides further molecular indications that are in agreement with a function in promoting stress resilience.

Glucocorticoids have been shown to stabilize and bundle actin filaments through upregulation of the actin binding protein caldesmon. This in turn prevented the release of ACTH in the pituitary tumor cell line AtT-20, thus presenting a negative feedback loop of glucocorticoids on HPA axis activity (Castellino et al., 1992). The bundling effect of DRR1 on actin dynamics appears similar and it appears to be expressed in the pituitary gland (www.genecards.org), therefore suggesting a possible influence on hormone release.

The serum response factor, which was found to be activated by DRR1 in this study, was previously described as a significant mediator of activity-dependent gene expression and synaptic plasticity, and consequently to promote learning and memory (Etkin et al., 2006; Ramanan et al., 2005). The brain-derived neurotrophic factor BDNF has lately received increased attention in psychiatric research, given its positive impact on neurogenesis, synapse formation and maturation, and memory formation, together with its downregulation upon stress exposure and in many mood disorders, including schizophrenia and depression (Brunoni et al., 2008; Vicario-Abejón et al., 2002; Xiu et al., 2009). Moreover, BDNF stimulation led to the activation of the serum-response factor SRF facilitating synaptic activity (Kalita et al., 2006). This convergence of mechanisms between DRR1 and BDNF support DRR1's function in promoting stress coping.

Interestingly, a shift of the G-/F-actin equilibrium in depression and bipolar disorder towards depolymerization and fragmentation of F-actin was suggested, as a result of cap1 downregulation, upregulation of cofilin and profilin, and downregulation of the cofilin-inactivating kinase LIMK1 in animal models and postmortem patient brains (Nakatani et al., 2004, 2007). The observed effects of DRR1 in this study generate a counteracting shift: increased F-actin and reduced turnover. Assuming a function of DRR1 in mediating coping and adaptation to stress by stabilization of F-actin is in accordance with the view of the opposite effects (depolymerization and F-actin fragmentation) promoting the development of mood disorders. Furthermore, the major susceptibility gene in schizophrenia, DISC1, was shown to interact with microtubule-associated proteins (including MAP1A) and actin-related proteins among others, further suggesting a role of cytoskeletal disturbance in this disease (Ishizuka et al., 2006; Millar et al., 2000).

Altogether, increasing evidence suggests a crucial involvement of the cytoskeleton in the etiology of stress-related mood disorders. However, conventional tricyclic antidepressants

appear not to target expression of actin-related genes (Nakatani et al., 2007). Although extensive studies are required in the future to dissect in more detail the function of actin during stress response and adaptation, these pathways might open up novel therapeutic approaches in the future.

5.6. Outlook

While this study provides important evidence in elucidating the molecular and cellular function of DRR1, it also raised interesting questions to be addressed in future research.

The known interaction of DRR1 and Prdx1 together with the finding that the unique cysteine residue of DRR1 is not significant for any particular function in the tests so far, could point to its potential role as a regulatory site for Prdx1. Prdx1 has been shown to regulate the activity of cytosolic proteins by reducing their intramolecular disulfide bond, raising the question whether covalent dimerization of DRR1 could be mediated through enzymatic activity of Prdx1 (Yan et al., 2009). Furthermore, DRR1's interaction partner MAP1A has been described as a stabilizer of microtubules, implying a role of DRR1 not only in F-actin stabilization, but also an involvement in microtubule stability (Halpain and Dehmelt, 2006; Le et al., 2010). Both interactions and their relevance for cellular processes would be interesting targets for future research.

With actin being the major driver of cell locomotion and given the effect of DRR1 on cell spreading together with its proposed function as tumor suppressor, an impact of DRR1 on cell migration is expected. Accordingly, progression through the cell cycle could be altered by DRR1. Analysis of both of these effects will further enlighten its intriguing role in tumor development and progression.

Finally, a detailed analysis of its function at the synapse would be highly interesting, to further support the novel link from stress through alterations of actin dynamics to synaptic transmission and behavior. Eventually, the aim would be to correlate each molecular effect of DRR1 – bundling, nucleation, and capping – with the respective functional alterations on pre- or postsynaptic transmission.

References

- Abraham, V.C., Krishnamurthi, V., Taylor, D.L., and Lanni, F. (1999). The actin-based nanomachine at the leading edge of migrating cells. *Biophys. J.* *77*, 1721–1732.
- Adler, J., and Parmryd, I. (2010). Quantifying colocalization by correlation: The Pearson correlation coefficient is superior to the Mander's overlap coefficient. *Cytometry A* *77A*, 733–742.
- Allison, D.W., Gelfand, V.I., Spector, I., and Craig, A.M. (1998). Role of Actin in Anchoring Postsynaptic Receptors in Cultured Hippocampal Neurons: Differential Attachment of NMDA Versus AMPA Receptors. *J. Neurosci.* *18*, 2423–2436.
- Aoki, K., Nakamura, T., and Matsuda, M. (2004). Spatio-temporal Regulation of Rac1 and Cdc42 Activity during Nerve Growth Factor-induced Neurite Outgrowth in PC12 Cells. *J. Biol. Chem.* *279*, 713–719.
- Asano, Y., Kishida, S., Mu, P., Sakamoto, K., Murohara, T., and Kadomatsu, K. (2010). DRR1 is expressed in the developing nervous system and downregulated during neuroblastoma carcinogenesis. *Biochem. Biophys. Res. Commun.* *394*, 829–835.
- Awakura, Y., Nakamura, E., Ito, N., Kamoto, T., and Ogawa, O. (2008). Methylation-associated silencing of TU3A in human cancers. *Int. J. Oncol.* *33*, 893–899.
- Baarlink, C., Wang, H., and Grosse, R. (2013). Nuclear Actin Network Assembly by Formins Regulates the SRF Coactivator MAL. *Science*.
- Bernstein, B.W., and Bamberg, J.R. (2003). Actin-ATP Hydrolysis Is a Major Energy Drain for Neurons. *J. Neurosci.* *23*, 1–6.
- Bernstein, B.W., and Bamberg, J.R. (2010). ADF/Cofilin: a functional node in cell biology. *Trends Cell Biol.* *20*, 187–195.
- Berrier, A.L., and LaFlamme, S.E. (2005). Cell-Spreading Assays. In *Cell Migration*, J.-L. Guan, ed. (Humana Press), pp. 55–68.
- Binder, E.B., Salyakina, D., Lichtner, P., Wochnik, G.M., Ising, M., Pütz, B., Papiol, S., Seaman, S., Lucae, S., Kohli, M.A., et al. (2004). Polymorphisms in FKBP5 are associated with increased recurrence of depressive episodes and rapid response to antidepressant treatment. *Nat. Genet.* *36*, 1319–1325.

- Boffa, L.C., Karn, J., Vidali, G., and Allfrey, V.G. (1977). Distribution of NG, NG-dimethylarginine in nuclear protein fractions. *Biochem. Biophys. Res. Commun.* *74*, 969–976.
- Bolo, N.R., Hodé, Y., and Macher, J.-P. (2004). Long-term sequestration of fluorinated compounds in tissues after fluvoxamine or fluoxetine treatment: a fluorine magnetic resonance spectroscopy study in vivo. *Magn. Reson. Mater. Phys. Biol. Med.* *16*, 268–276.
- Van den Boom, J., Wolter, M., Blaschke, B., Knobbe, C.B., and Reifenberger, G. (2006). Identification of novel genes associated with astrocytoma progression using suppression subtractive hybridization and real-time reverse transcription-polymerase chain reaction. *Int. J. Cancer* *119*, 2330–2338.
- Bourne, J.N., and Harris, K.M. (2008). Balancing structure and function at hippocampal dendritic spines. *Annu. Rev. Neurosci.* *31*, 47–67.
- Braithwaite, R.A. (1980). Plasma-protein binding of tricyclic antidepressants. *Postgrad. Med. J.* *56 Suppl 1*, 107–111.
- Brunoni, A.R., Lopes, M., and Fregni, F. (2008). A systematic review and meta-analysis of clinical studies on major depression and BDNF levels: implications for the role of neuroplasticity in depression. *Int. J. Neuropsychopharmacol.* *11*, 1169–1180.
- BurrIDGE, K., and Wennerberg, K. (2004). Rho and Rac take center stage. *Cell* *116*, 167–179.
- Butler, P.W., and Besser, G.M. (1968). Pituitary-adrenal function in depression. *Lancet* *2*, 51.
- Calabrese, B., Wilson, M.S., and Halpain, S. (2006). Development and Regulation of Dendritic Spine Synapses. *Physiology* *21*, 38–47.
- Carlier, M.-F., Laurent, V., Santolini, J., Melki, R., Didry, D., Xia, G.-X., Hong, Y., Chua, N.-H., and Pantaloni, D. (1997). Actin Depolymerizing Factor (ADF/Cofilin) Enhances the Rate of Filament Turnover: Implication in Actin-based Motility. *J. Cell Biol.* *136*, 1307–1322.
- Castano, E., Philimonenko, V.V., Kahle, M., Fukalová, J., Kalendová, A., Yildirim, S., Dzijak, R., Dingová-Krásna, H., and Hozák, P. (2010). Actin complexes in the cell nucleus: new stones in an old field. *Histochem. Cell Biol.* *133*, 607–626.
- Castellino, F., Heuser, J., Marchetti, S., Bruno, B., and Luini, A. (1992). Glucocorticoid stabilization of actin filaments: a possible mechanism for inhibition of corticotropin release. *Proc. Natl. Acad. Sci.* *89*, 3775–3779.
- Chamaroux, F., Fache, S., Bruckert, F., and Fourcade, B. (2005). Kinetics of cell spreading. *Phys. Rev. Lett.* *94*, 158102.
- Chang, T., and Fava, M. (2010). The future of psychopharmacology of depression. *J. Clin. Psychiatry* *71*, 971–975.

- Chen, Y., Dubé, C.M., Rice, C.J., and Baram, T.Z. (2008). Rapid Loss of Dendritic Spines after Stress Involves Derangement of Spine Dynamics by Corticotropin-Releasing Hormone. *J. Neurosci.* *28*, 2903–2911.
- Chu, G., Hayakawa, H., and Berg, P. (1987). Electroporation for the efficient transfection of mammalian cells with DNA. *Nucleic Acids Res.* *15*, 1311–1326.
- Cingolani, L.A., and Goda, Y. (2008). Actin in action: the interplay between the actin cytoskeleton and synaptic efficacy. *Nat. Rev. Neurosci.* *9*, 344–356.
- Clarke, L.E., and Barres, B.A. (2013). Emerging roles of astrocytes in neural circuit development. *Nat. Rev. Neurosci.* *14*, 311–321.
- Cooper, J.A., and Pollard, T.D. (1985). Effect of capping protein on the kinetics of actin polymerization. *Biochemistry (Mosc.)* *24*, 793–799.
- Cooper, J.A., Walker, S.B., and Pollard, T.D. (1983). Pyrene actin: documentation of the validity of a sensitive assay for actin polymerization. *J. Muscle Res. Cell Motil.* *4*, 253–262.
- Costes, S.V., Daelemans, D., Cho, E.H., Dobbin, Z., Pavlakis, G., and Lockett, S. (2004). Automatic and Quantitative Measurement of Protein-Protein Colocalization in Live Cells. *Biophys. J.* *86*, 3993–4003.
- Cramer, L.P., Siebert, M., and Mitchison, T.J. (1997). Identification of Novel Graded Polarity Actin Filament Bundles in Locomoting Heart Fibroblasts: Implications for the Generation of Motile Force. *J. Cell Biol.* *136*, 1287–1305.
- Croce, A., Cassata, G., Disanza, A., Gagliani, M.C., Tacchetti, C., Malabarba, M.G., Carlier, M.-F., Scita, G., Baumeister, R., and Fiore, P.P.D. (2004). A novel actin barbed-end-capping activity in EPS-8 regulates apical morphogenesis in intestinal cells of *Caenorhabditis elegans*. *Nat. Cell Biol.* *6*, 1173–1179.
- Cuvelier, D., Théry, M., Chu, Y.-S., Dufour, S., Thiéry, J.-P., Bornens, M., Nassoy, P., and Mahadevan, L. (2007). The Universal Dynamics of Cell Spreading. *Curr. Biol.* *17*, 694–699.
- Czéh, B., and Lucassen, P.J. (2007). What causes the hippocampal volume decrease in depression? Are neurogenesis, glial changes and apoptosis implicated? *Eur. Arch. Psychiatry Clin. Neurosci.* *257*, 250–260.
- Datson, N.A., van der Perk, J., de Kloet, E.R., and Vreugdenhil, E. (2001). Expression profile of 30,000 genes in rat hippocampus using SAGE. *Hippocampus* *11*, 430–444.
- Dillon, C., and Goda, Y. (2005). The actin cytoskeleton: integrating form and function at the synapse. *Annu. Rev. Neurosci.* *28*, 25–55.
- Dominguez, R. (2010). Structural insights into de novo actin polymerization. *Curr. Opin. Struct. Biol.* *20*, 217–225.
- Domnina, L.V., Gelfand, V.I., Ivanova, O.Y., Leonova, E.V., Pletjushkina, O.Y., Vasiliev, J.M., and Gelfand, I.M. (1982). Effects of small doses of cytochalasins on fibroblasts:

- preferential changes of active edges and focal contacts. *Proc. Natl. Acad. Sci.* *79*, 7754–7757.
- Dotti, C.G., Sullivan, C.A., and Banker, G.A. (1988). The establishment of polarity by hippocampal neurons in culture. *J. Neurosci. Off. J. Soc. Neurosci.* *8*, 1454–1468.
- Dudley, A., Sater, M., Le, P.U., Trinh, G., Sadr, M.S., Bergeron, J., Deleavey, G.F., Bedell, B., Damha, M.J., and Petrecca, K. (2013). DRR regulates AKT activation to drive brain cancer invasion. *Oncogene*.
- Dunn, K.W., Kamocka, M.M., and McDonald, J.H. (2011). A practical guide to evaluating colocalization in biological microscopy. *Am. J. Physiol. - Cell Physiol.* *300*, C723–C742.
- Edwards, M., Zwolak, A., Schafer, D.A., Sept, D., Dominguez, R., and Cooper, J.A. (2014). Capping protein regulators fine-tune actin assembly dynamics. *Nat. Rev. Mol. Cell Biol.* *15*, 677–689.
- Engelmann, M., Landgraf, R., and Wotjak, C.T. (2004). The hypothalamic-neurohypophysial system regulates the hypothalamic-pituitary-adrenal axis under stress: an old concept revisited. *Front. Neuroendocrinol.* *25*, 132–149.
- Esnault, C., Stewart, A., Gualdrini, F., East, P., Horswell, S., Matthews, N., and Treisman, R. (2014). Rho-actin signaling to the MRTF coactivators dominates the immediate transcriptional response to serum in fibroblasts. *Genes Dev.* *28*, 943–958.
- Etkin, A., Alarcón, J.M., Weisberg, S.P., Touzani, K., Huang, Y.Y., Nordheim, A., and Kandel, E.R. (2006). A Role in Learning for SRF: Deletion in the Adult Forebrain Disrupts LTD and the Formation of an Immediate Memory of a Novel Context. *Neuron* *50*, 127–143.
- Euteneuer, U., and Schliwa, M. (1984). Persistent, directional motility of cells and cytoplasmic fragments in the absence of microtubules. *Nature* *310*, 58–61.
- Falzone, T.T., Lenz, M., Kovar, D.R., and Gardel, M.L. (2012). Assembly kinetics determine the architecture of α -actinin crosslinked F-actin networks. *Nat. Commun.* *3*, 861.
- Fan, Y., Tang, X., Vitriol, E., Chen, G., and Zheng, J.Q. (2011). Actin Capping Protein Is Required for Dendritic Spine Development and Synapse Formation. *J. Neurosci.* *31*, 10228–10233.
- Fèvre-Montange (2009). Microarray gene expression profiling in meningiomas: Differential expression according to grade or histopathological subtype. *Int. J. Oncol.* *35*.
- Fling, S.P., and Gregerson, D.S. (1986). Peptide and protein molecular weight determination by electrophoresis using a high-molarity tris buffer system without urea. *Anal. Biochem.* *155*, 83–88.
- Fox, J.D., and Waugh, D.S. (2003). Maltose-binding protein as a solubility enhancer. *Methods Mol. Biol. Clifton NJ* *205*, 99–117.
- Frijters, R., Fleuren, W., Toonen, E.J.M., Tuckermann, J.P., Reichardt, H.M., van der Maaden, H., van Elsas, A., van Lierop, M.-J., Dokter, W., de Vlieg, J., et al. (2010).

- Prednisolone-induced differential gene expression in mouse liver carrying wild type or a dimerization-defective glucocorticoid receptor. *BMC Genomics* *11*, 359.
- Frost, N.A., Shroff, H., Kong, H., Betzig, E., and Blanpied, T.A. (2010). Single-molecule discrimination of discrete perisynaptic and distributed sites of actin filament assembly within dendritic spines. *Neuron* *67*, 86–99.
- Fuchs, E., Flugge, G., and Czeh, B. (2006). Remodeling of neuronal networks by stress. *Front. Biosci. J. Virtual Libr.* *11*, 2746–2758.
- Fukazawa, Y., Saitoh, Y., Ozawa, F., Ohta, Y., Mizuno, K., and Inokuchi, K. (2003). Hippocampal LTP Is Accompanied by Enhanced F-Actin Content within the Dendritic Spine that Is Essential for Late LTP Maintenance In Vivo. *Neuron* *38*, 447–460.
- Ghashghaei, H.T., Lai, C., and Anton, E.S. (2007). Neuronal migration in the adult brain: are we there yet? *Nat. Rev. Neurosci.* *8*, 141–151.
- Golden, S.A., Christoffel, D.J., Heshmati, M., Hodes, G.E., Magida, J., Davis, K., Cahill, M.E., Dias, C., Ribeiro, E., Ables, J.L., et al. (2013). Epigenetic regulation of RAC1 induces synaptic remodeling in stress disorders and depression. *Nat. Med.* *19*, 337–344.
- Govek, E.-E., Newey, S.E., and Aelst, L.V. (2005). The role of the Rho GTPases in neuronal development. *Genes Dev.* *19*, 1–49.
- Gremm, D., and Wegner, A. (2000). Gelsolin as a calcium-regulated actin filament-capping protein. *Eur. J. Biochem.* *267*, 4339–4345.
- Hall, A. (1998). Rho GTPases and the actin cytoskeleton. *Science* *279*, 509–514.
- Halligan, S.L., Herbert, J., Goodyer, I., and Murray, L. (2007). Disturbances in morning cortisol secretion in association with maternal postnatal depression predict subsequent depressive symptomatology in adolescents. *Biol. Psychiatry* *62*, 40–46.
- Halpain, S., and Dehmelt, L. (2006). The MAP1 family of microtubule-associated proteins. *Genome Biol.* *7*, 224.
- Harris, E.S., and Higgs, H.N. (2006). Biochemical analysis of mammalian formin effects on actin dynamics. *Methods Enzymol.* *406*, 190–214.
- Henry, M.E., Schmidt, M.E., Hennen, J., Villafuerte, R.A., Butman, M.L., Tran, P., Kerner, L.T., Cohen, B., and Renshaw, P.F. (2005). A Comparison of Brain and Serum Pharmacokinetics of R-Fluoxetine and Racemic Fluoxetine: A 19-F MRS Study. *Neuropsychopharmacology* *30*, 1576–1583.
- Hertzog, M., Milanesi, F., Hazelwood, L., Disanza, A., Liu, H., Perlade, E., Malabarba, M.G., Pasqualato, S., Maiolica, A., Confalonieri, S., et al. (2010). Molecular Basis for the Dual Function of Eps8 on Actin Dynamics: Bundling and Capping. *PLoS Biol* *8*, e1000387.
- Higgs, H.N., Blanchoin, L., and Pollard, T.D. (1999). Influence of the C terminus of Wiskott-Aldrich syndrome protein (WASp) and the Arp2/3 complex on actin polymerization. *Biochemistry (Mosc.)* *38*, 15212–15222.

- Holsboer, F. (2000). The corticosteroid receptor hypothesis of depression. *Neuropsychopharmacol. Off. Publ. Am. Coll. Neuropsychopharmacol.* *23*, 477–501.
- Honkura, N., Matsuzaki, M., Noguchi, J., Ellis-Davies, G.C.R., and Kasai, H. (2008). The subspine organization of actin fibers regulates the structure and plasticity of dendritic spines. *Neuron* *57*, 719–729.
- Hotulainen, P., and Hoogenraad, C.C. (2010). Actin in dendritic spines: connecting dynamics to function. *J. Cell Biol.* *189*, 619–629.
- Ishizuka, K., Paek, M., Kamiya, A., and Sawa, A. (2006). A review of Disrupted-In-Schizophrenia-1 (DISC1): neurodevelopment, cognition, and mental conditions. *Biol. Psychiatry* *59*, 1189–1197.
- Ising, M., and Holsboer, F. (2006). Genetics of stress response and stress-related disorders. *Dialogues Clin. Neurosci.* *8*, 433–444.
- Ivanov, A., Esclapez, M., Pellegrino, C., Shirao, T., and Ferhat, L. (2009). Drebrin A regulates dendritic spine plasticity and synaptic function in mature cultured hippocampal neurons. *J. Cell Sci.* *122*, 524–534.
- Jaworski, J., Kapitein, L.C., Gouveia, S.M., Dortland, B.R., Wulf, P.S., Grigoriev, I., Camera, P., Spangler, S.A., Di Stefano, P., Demmers, J., et al. (2009). Dynamic Microtubules Regulate Dendritic Spine Morphology and Synaptic Plasticity. *Neuron* *61*, 85–100.
- Jayo, A., and Parsons, M. (2010). Fascin: a key regulator of cytoskeletal dynamics. *Int. J. Biochem. Cell Biol.* *42*, 1614–1617.
- Jeon, C., Moon, M., Kim, J., Kim, H., Kim, J., Li, Y., Jin, J., Kim, P., Kim, H., Meier, K.E., et al. (2011). Control of neurite outgrowth by RhoA inactivation. *J. Neurochem.*
- Jiang, M., and Chen, G. (2006). High Ca²⁺-phosphate transfection efficiency in low-density neuronal cultures. *Nat. Protoc.* *1*, 695–700.
- Jordan, R., Lemke, E.A., and Klingauf, J. (2005). Visualization of Synaptic Vesicle Movement in Intact Synaptic Boutons Using Fluorescence Fluctuation Spectroscopy. *Biophys. J.* *89*, 2091–2102.
- Kalita, K., Kharebava, G., Zheng, J.-J., and Hetman, M. (2006). Role of Megakaryoblastic Acute Leukemia-1 in ERK1/2-Dependent Stimulation of Serum Response Factor-Driven Transcription by BDNF or Increased Synaptic Activity. *J. Neurosci.* *26*, 10020–10032.
- Kalita, K., Kuzniewska, B., and Kaczmarek, L. (2012). MKLs: Co-factors of serum response factor (SRF) in neuronal responses. *Int. J. Biochem. Cell Biol.* *44*, 1444–1447.
- Kasai, H., Fukuda, M., Watanabe, S., Hayashi-Takagi, A., and Noguchi, J. (2010). Structural dynamics of dendritic spines in memory and cognition. *Trends Neurosci.* *33*, 121–129.
- Khatau, S.B., Hale, C.M., Stewart-Hutchinson, P.J., Patel, M.S., Stewart, C.L., Searson, P.C., Hodzic, D., and Wirtz, D. (2009). A perinuclear actin cap regulates nuclear shape. *Proc. Natl. Acad. Sci.* *106*, 19017–19022.

- Kholodnyuk, I.D., Kozireva, S., Kost-Alimova, M., Kashuba, V., Klein, G., and Imreh, S. (2006). Down regulation of 3p genes, LTF, SLC38A3 and DRR1, upon growth of human chromosome 3-mouse fibrosarcoma hybrids in severe combined immunodeficiency mice. *Int. J. Cancer J. Int. Cancer* *119*, 99–107.
- Klengel, T., Mehta, D., Anacker, C., Rex-Haffner, M., Pruessner, J.C., Pariante, C.M., Pace, T.W.W., Mercer, K.B., Mayberg, H.S., Bradley, B., et al. (2013). Allele-specific FKBP5 DNA demethylation mediates gene–childhood trauma interactions. *Nat. Neurosci.* *16*, 33–41.
- De Kloet, E.R., and Reul, J.M. (1987). Feedback action and tonic influence of corticosteroids on brain function: a concept arising from the heterogeneity of brain receptor systems. *Psychoneuroendocrinology* *12*, 83–105.
- De Kloet, E.R., Oitzl, M.S., and Joëls, M. (1993). Functional implications of brain corticosteroid receptor diversity. *Cell. Mol. Neurobiol.* *13*, 433–455.
- De Kloet, E.R., Joëls, M., and Holsboer, F. (2005). Stress and the brain: from adaptation to disease. *Nat. Rev. Neurosci.* *6*, 463–475.
- Knöll, B., Kretz, O., Fiedler, C., Alberti, S., Schütz, G., Frotscher, M., and Nordheim, A. (2006). Serum response factor controls neuronal circuit assembly in the hippocampus. *Nat. Neurosci.* *9*, 195–204.
- Korobova, F., and Svitkina, T. (2010). Molecular Architecture of Synaptic Actin Cytoskeleton in Hippocampal Neurons Reveals a Mechanism of Dendritic Spine Morphogenesis. *Mol. Biol. Cell* *21*, 165–176.
- Koskinen, M., and Hotulainen, P. (2014). Measuring F-actin properties in dendritic spines. *Front. Neuroanat.* *8*, 74.
- Kouyama, T., and Mihashi, K. (1981). Fluorimetry study of N-(1-pyrenyl)iodoacetamide-labelled F-actin. Local structural change of actin protomer both on polymerization and on binding of heavy meromyosin. *Eur. J. Biochem. FEBS* *114*, 33–38.
- Kretzschmar, A. (2010). Domain Mapping of the Novel Stress-Inducible Protein DRR1. Masters Thesis Tech. Univ. Münch.
- Kuhn, T.B., Meberg, P.J., Brown, M.D., Bernstein, B.W., Minamide, L.S., Jensen, J.R., Okada, K., Soda, E.A., and Bamberg, J.R. (2000). Regulating actin dynamics in neuronal growth cones by ADF/cofilin and rho family GTPases. *J. Neurobiol.* *44*, 126–144.
- Kukalev, A., Nord, Y., Palmberg, C., Bergman, T., and Percipalle, P. (2005). Actin and hnRNP U cooperate for productive transcription by RNA polymerase II. *Nat. Struct. Mol. Biol.* *12*, 238–244.
- Landfield, P.W., Baskin, R.K., and Pitler, T.A. (1981). Brain aging correlates: retardation by hormonal-pharmacological treatments. *Science* *214*, 581–584.
- Lanni, C., Govoni, S., Lucchelli, A., and Boselli, C. (2009). Depression and antidepressants: molecular and cellular aspects. *Cell. Mol. Life Sci. CMLS* *66*, 2985–3008.

- Lappalainen, P., and Drubin, D.G. (1997). Cofilin promotes rapid actin filament turnover in vivo. *Nature* *388*, 78–82.
- Le, P.U., Angers-Loustau, A., de Oliveira, R.M.W., Ajlan, A., Brassard, C.L., Dudley, A., Brent, H., Siu, V., Trinh, G., Molenkamp, G., et al. (2010). DRR drives brain cancer invasion by regulating cytoskeletal-focal adhesion dynamics. *Oncogene* *29*, 4636–4647.
- Lee, Y.-H., and Stallcup, M.R. (2009). Minireview: Protein Arginine Methylation of Nonhistone Proteins in Transcriptional Regulation. *Mol. Endocrinol.* *23*, 425–433.
- Lee, Y.-J., and Keng, P.C. (2005). Studying the effects of actin cytoskeletal destabilization on cell cycle by cofilin overexpression. *Mol. Biotechnol.* *31*, 1–10.
- Lee, I.-J., Coffman, V.C., and Wu, J.-Q. (2012). Contractile-ring assembly in fission yeast cytokinesis: Recent advances and new perspectives. *Cytoskelet. Hoboken NJ* *69*, 751–763.
- Lee, J.S., Ho, W.-K., Neher, E., and Lee, S.-H. (2013). Superpriming of synaptic vesicles after their recruitment to the readily releasable pool. *Proc. Natl. Acad. Sci.* *110*, 15079–15084.
- Levine, S. (2001). Primary social relationships influence the development of the hypothalamic–pituitary–adrenal axis in the rat. *Physiol. Behav.* *73*, 255–260.
- Li, J., Han, D., and Zhao, Y.-P. (2014). Kinetic behaviour of the cells touching substrate: the interfacial stiffness guides cell spreading. *Sci. Rep.* *4*.
- Liebl, C., Panhuysen, M., Pütz, B., Trümbach, D., Wurst, W., Deussing, J.M., Müller, M.B., and Schmidt, M.V. (2009). Gene expression profiling following maternal deprivation: involvement of the brain Renin-Angiotensin system. *Front. Mol. Neurosci.* *2*, 1.
- Lieleg, O., Claessens, M.M.A.E., and Bausch, A.R. (2009). Structure and dynamics of cross-linked actin networks. *Soft Matter* *6*, 218–225.
- Lin, L.-J., Zhang, Y., Lin, Y., Jin, Y., and Zheng, C.-Q. (2014). Identifying candidate genes for discrimination of ulcerative colitis and Crohn’s disease. *Mol. Biol. Rep.* *41*, 6349–6355.
- Liu, Q., Zhao, X.-Y., Bai, R.-Z., Liang, S.-F., Nie, C.-L., Yuan, Z., Wang, C.-T., Wu, Y., Chen, L.-J., and Wei, Y.-Q. (2009). Induction of tumor inhibition and apoptosis by a candidate tumor suppressor gene DRR1 on 3p21.1. *Oncol. Rep.* *22*, 1069–1075.
- Lupien, S.J., McEwen, B.S., Gunnar, M.R., and Heim, C. (2009). Effects of stress throughout the lifespan on the brain, behaviour and cognition. *Nat. Rev. Neurosci.* *10*, 434–445.
- Mabuchi, I. (1994). Cleavage furrow: timing of emergence of contractile ring actin filaments and establishment of the contractile ring by filament bundling in sea urchin eggs. *J. Cell Sci.* *107 (Pt 7)*, 1853–1862.
- Manders, E.M., Stap, J., Brakenhoff, G.J., Driel, R. van, and Aten, J.A. (1992). Dynamics of three-dimensional replication patterns during the S-phase, analysed by double labelling of DNA and confocal microscopy. *J. Cell Sci.* *103*, 857–862.

- Masana, M., Su, Y.-A., Liebl, C., Wang, X.-D., Jansen, L., Westerholz, S., Wagner, K.V., Labermaier, C., Scharf, S.H., Santarelli, S., et al. (2014). The stress-inducible actin-interacting protein DRR1 shapes social behavior. *Psychoneuroendocrinology* *48*, 98–110.
- Masana, M., Jukic, M.M., Kretzschmar, A., Wagner, K.V., Westerholz, S., Schmidt, M.V., Rein, T., Brodski, C., and Müller, M.B. (2015). Deciphering the spatio-temporal expression and stress regulation of Fam107B, the paralog of the resilience-promoting protein DRR1 in the mouse brain. *Neuroscience* *290*, 147–158.
- McDonald, D., Carrero, G., Andrin, C., de Vries, G., and Hendzel, M.J. (2006). Nucleoplasmic β -actin exists in a dynamic equilibrium between low-mobility polymeric species and rapidly diffusing populations. *J. Cell Biol.* *172*, 541–552.
- McLaughlin, K.A., Conron, K.J., Koenen, K.C., and Gilman, S.E. (2010). Childhood adversity, adult stressful life events, and risk of past-year psychiatric disorder: a test of the stress sensitization hypothesis in a population-based sample of adults. *Psychol. Med.* *40*, 1647–1658.
- Mejillano, M.R., Kojima, S., Applewhite, D.A., Gertler, F.B., Svitkina, T.M., and Borisy, G.G. (2004). Lamellipodial Versus Filopodial Mode of the Actin Nanomachinery: Pivotal Role of the Filament Barbed End. *Cell* *118*, 363–373.
- Menna, E., Zambetti, S., Morini, R., Donzelli, A., Disanza, A., Calvigioni, D., Braida, D., Nicolini, C., Orlando, M., Fossati, G., et al. (2013). Eps8 controls dendritic spine density and synaptic plasticity through its actin-capping activity. *EMBO J.*
- Millar, J.K., Wilson-Annan, J.C., Anderson, S., Christie, S., Taylor, M.S., Semple, C.A., Devon, R.S., St Clair, D.M., Muir, W.J., Blackwood, D.H., et al. (2000). Disruption of two novel genes by a translocation co-segregating with schizophrenia. *Hum. Mol. Genet.* *9*, 1415–1423.
- Mitchison, T.J., and Cramer, L.P. (1996). Actin-Based Cell Motility and Cell Locomotion. *Cell* *84*, 371–379.
- Montgomery, S.A. (1989). The efficacy of fluoxetine as an antidepressant in the short and long term. *Int. Clin. Psychopharmacol.* *4 Suppl 1*, 113–119.
- Morales, M., Colicos, M.A., and Goda, Y. (2000). Actin-dependent regulation of neurotransmitter release at central synapses. *Neuron* *27*, 539–550.
- Morris, J.A., Kandpal, G., Ma, L., and Austin, C.P. (2003). DISC1 (Disrupted-In-Schizophrenia 1) is a centrosome-associated protein that interacts with MAP1A, MIPT3, ATF4/5 and NUDEL: regulation and loss of interaction with mutation. *Hum. Mol. Genet.* *12*, 1591–1608.
- Moulding, D.A., Blundell, M.P., Spiller, D.G., White, M.R.H., Cory, G.O., Calle, Y., Kempinski, H., Sinclair, J., Ancliff, P.J., Kinnon, C., et al. (2007). Unregulated actin polymerization by WASp causes defects of mitosis and cytokinesis in X-linked neutropenia. *J. Exp. Med.* *204*, 2213–2224.
- Mullins, R.D., Heuser, J.A., and Pollard, T.D. (1998). The interaction of Arp2/3 complex with actin: Nucleation, high affinity pointed end capping, and formation of branching networks of filaments. *Proc. Natl. Acad. Sci. U. S. A.* *95*, 6181–6186.

- Nakajima, H., and Koizumi, K. (2014). Family with sequence similarity 107: A family of stress responsive small proteins with diverse functions in cancer and the nervous system (Review). *Biomed. Rep.* *2*, 321–325.
- Nakajima, H., Ishigaki, Y., Xia, Q.-S., Ikeda, T., Yoshitake, Y., Yonekura, H., Nojima, T., Tanaka, T., Umehara, H., Tomosugi, N., et al. (2010). Induction of HITS, a newly identified family with sequence similarity 107 protein (FAM107B), in cancer cells by heat shock stimulation. *Int. J. Oncol.* *37*, 583–593.
- Nakajima, H., Koizumi, K., Tanaka, T., Ishigaki, Y., Yoshitake, Y., Yonekura, H., Sakuma, T., Fukushima, T., Umehara, H., Ueno, S., et al. (2012). Loss of HITS (FAM107B) expression in cancers of multiple organs: tissue microarray analysis. *Int. J. Oncol.*
- Nakamura, F., Stossel, T.P., and Hartwig, J.H. (2011). The filamins. *Cell Adhes. Migr.* *5*, 160–169.
- Nakatani, N., Aburatani, H., Nishimura, K., Semba, J., and Yoshikawa, T. (2004). Comprehensive expression analysis of a rat depression model. *Pharmacogenomics J.* *4*, 114–126.
- Nakatani, N., Ohnishi, T., Iwamoto, K., Watanabe, A., Iwayama, Y., Yamashita, S., Ishitsuka, Y., Moriyama, K., Nakajima, M., Tatebayashi, Y., et al. (2007). Expression analysis of actin-related genes as an underlying mechanism for mood disorders. *Biochem. Biophys. Res. Commun.* *352*, 780–786.
- Nakayama, A.Y., Harms, M.B., and Luo, L. (2000). Small GTPases Rac and Rho in the Maintenance of Dendritic Spines and Branches in Hippocampal Pyramidal Neurons. *J. Neurosci.* *20*, 5329–5338.
- Narumiya, S., Tanji, M., and Ishizaki, T. (2009). Rho signaling, ROCK and mDia1, in transformation, metastasis and invasion. *Cancer Metastasis Rev.* *28*, 65–76.
- Nedergaard, M., Ransom, B., and Goldman, S.A. (2003). New roles for astrocytes: Redefining the functional architecture of the brain. *Trends Neurosci.* *26*, 523–530.
- Neves, G., Cooke, S.F., and Bliss, T.V.P. (2008). Synaptic plasticity, memory and the hippocampus: a neural network approach to causality. *Nat. Rev. Neurosci.* *9*, 65–75.
- Newey, S.E., Velamoor, V., Govek, E.-E., and Van Aelst, L. (2005). Rho GTPases, dendritic structure, and mental retardation. *J. Neurobiol.* *64*, 58–74.
- Okamoto, K.-I., Nagai, T., Miyawaki, A., and Hayashi, Y. (2004). Rapid and persistent modulation of actin dynamics regulates postsynaptic reorganization underlying bidirectional plasticity. *Nat. Neurosci.* *7*, 1104–1112.
- Okamoto, K.-I., Narayanan, R., Lee, S.H., Murata, K., and Hayashi, Y. (2007). The role of CaMKII as an F-actin-bundling protein crucial for maintenance of dendritic spine structure. *Proc. Natl. Acad. Sci.* *104*, 6418–6423.
- Osterweil, E., Wells, D.G., and Mooseker, M.S. (2005). A role for myosin VI in postsynaptic structure and glutamate receptor endocytosis. *J. Cell Biol.* *168*, 329–338.

- Pacák, K., and Palkovits, M. (2001). Stressor specificity of central neuroendocrine responses: implications for stress-related disorders. *Endocr. Rev.* *22*, 502–548.
- Parker, K.J., Schatzberg, A.F., and Lyons, D.M. (2003). Neuroendocrine aspects of hypercortisolism in major depression. *Horm. Behav.* *43*, 60–66.
- Patla, I., Volberg, T., Elad, N., Hirschfeld-Warneken, V., Grashoff, C., Fässler, R., Spatz, J.P., Geiger, B., and Medalia, O. (2010). Dissecting the molecular architecture of integrin adhesion sites by cryo-electron tomography. *Nat. Cell Biol.* *12*, 909–915.
- Pederson, T. (2008). As functional nuclear actin comes into view, is it globular, filamentous, or both? *J. Cell Biol.* *180*, 1061–1064.
- Percipalle, P., Fomproix, N., Kylberg, K., Miralles, F., Björkroth, B., Daneholt, B., and Visa, N. (2003). An actin–ribonucleoprotein interaction is involved in transcription by RNA polymerase II. *Proc. Natl. Acad. Sci.* *100*, 6475–6480.
- Piubelli, C., Gruber, S., El Khoury, A., Mathé, A.A., Domenici, E., and Carboni, L. (2011a). Nortriptyline influences protein pathways involved in carbohydrate metabolism and actin-related processes in a rat gene–environment model of depression. *Eur. Neuropsychopharmacol.* *21*, 545–562.
- Piubelli, C., Vighini, M., Mathé, A.A., Domenici, E., and Carboni, L. (2011b). Escitalopram Affects Cytoskeleton and Synaptic Plasticity Pathways in a Rat Gene–environment Interaction Model of Depression as Revealed by Proteomics. Part II: Environmental Challenge. *Int. J. Neuropsychopharmacol.* *14*, 834–855.
- Pletjushkina, O.J., Ivanova, O.J., Kaverina, I.N., and Vasiliev, J.M. (1994). Taxol-treated fibroblasts acquire an epithelioid shape and a circular pattern of actin bundles. *Exp. Cell Res.* *212*, 201–208.
- Pollard, T.D. (1986). Rate constants for the reactions of ATP- and ADP-actin with the ends of actin filaments. *J. Cell Biol.* *103*, 2747–2754.
- Pollard, T.D., and Borisy, G.G. (2003). Cellular Motility Driven by Assembly and Disassembly of Actin Filaments. *Cell* *112*, 453–465.
- Pollard, T.D., and Cooper, J.A. (1984). Quantitative analysis of the effect of *Acanthamoeba* profilin on actin filament nucleation and elongation. *Biochemistry (Mosc.)* *23*, 6631–6641.
- Pollard, T.D., and Cooper, J.A. (2009). Actin, a Central Player in Cell Shape and Movement. *Science* *326*, 1208–1212.
- Posern, G., and Treisman, R. (2006). Actin’ together: serum response factor, its cofactors and the link to signal transduction. *Trends Cell Biol.* *16*, 588–596.
- Pruyne, D., Evangelista, M., Yang, C., Bi, E., Zigmund, S., Bretscher, A., and Boone, C. (2002). Role of formins in actin assembly: nucleation and barbed-end association. *Science* *297*, 612–615.

- Ramanan, N., Shen, Y., Sarsfield, S., Lemberger, T., Schütz, G., Linden, D.J., and Ginty, D.D. (2005). SRF mediates activity-induced gene expression and synaptic plasticity but not neuronal viability. *Nat. Neurosci.* *8*, 759–767.
- Reagan, L.P., Grillo, C.A., and Piroli, G.G. (2008). The As and Ds of stress: metabolic, morphological and behavioral consequences. *Eur. J. Pharmacol.* *585*, 64–75.
- Reul, J.M., and de Kloet, E.R. (1985). Two receptor systems for corticosterone in rat brain: microdistribution and differential occupation. *Endocrinology* *117*, 2505–2511.
- Rivière, J.-B., van Bon, B.W.M., Hoischen, A., Kholmanskikh, S.S., O’Roak, B.J., Gilissen, C., Gijsen, S., Sullivan, C.T., Christian, S.L., Abdul-Rahman, O.A., et al. (2012). De novo mutations in the actin genes ACTB and ACTG1 cause Baraitser-Winter syndrome. *Nat. Genet.* *44*, 440–444, S1–S2.
- Rohatgi, R., Ma, L., Miki, H., Lopez, M., Kirchhausen, T., Takenawa, T., and Kirschner, M.W. (1999). The Interaction between N-WASP and the Arp2/3 Complex Links Cdc42-Dependent Signals to Actin Assembly. *Cell* *97*, 221–231.
- Roosendaal, B., McEwen, B.S., and Chattarji, S. (2009). Stress, memory and the amygdala. *Nat. Rev. Neurosci.* *10*, 423–433.
- Ruchhoeft, M.L., Ohnuma, S., McNeill, L., Holt, C.E., and Harris, W.A. (1999). The neuronal architecture of *Xenopus* retinal ganglion cells is sculpted by rho-family GTPases in vivo. *J. Neurosci. Off. J. Soc. Neurosci.* *19*, 8454–8463.
- Rüegg, J., Holsboer, F., Turck, C., and Rein, T. (2004). Cofilin 1 Is Revealed as an Inhibitor of Glucocorticoid Receptor by Analysis of Hormone-Resistant Cells. *Mol. Cell. Biol.* *24*, 9371–9382.
- Sampath, P., and Pollard, T.D. (1991). Effects of cytochalasin, phalloidin, and pH on the elongation of actin filaments. *Biochemistry (Mosc.)* *30*, 1973–1980.
- Sarner, S., Kozma, R., Ahmed, S., and Lim, L. (2000). Phosphatidylinositol 3-Kinase, Cdc42, and Rac1 Act Downstream of Ras in Integrin-Dependent Neurite Outgrowth in N1E-115 Neuroblastoma Cells. *Mol. Cell. Biol.* *20*, 158–172.
- Schirenbeck, A., Bretschneider, T., Arasada, R., Schleicher, M., and Faix, J. (2005). The Diaphanous-related formin dDia2 is required for the formation and maintenance of filopodia. *Nat. Cell Biol.* *7*, 619–625.
- Schmidt, M.V., Schülke, J.-P., Liebl, C., Stuess, M., Avrabos, C., Bock, J., Wochnik, G.M., Davies, H.A., Zimmermann, N., Scharf, S.H., et al. (2011). Tumor suppressor down-regulated in renal cell carcinoma 1 (DRR1) is a stress-induced actin bundling factor that modulates synaptic efficacy and cognition. *Proc. Natl. Acad. Sci. U. S. A.*
- Schmoller, K.M., Lieleg, O., and Bausch, A.R. (2009). Structural and Viscoelastic Properties of Actin/Filamin Networks: Cross-Linked versus Bundled Networks. *Biophys. J.* *97*, 83–89.
- Schmoller, K.M., Semmrich, C., and Bausch, A.R. (2011). Slow down of actin depolymerization by cross-linking molecules. *J. Struct. Biol.* *173*, 350–357.

- Schoenfeld, T.A., McKerracher, L., Obar, R., and Vallee, R.B. (1989). MAP 1A and MAP 1B are structurally related microtubule associated proteins with distinct developmental patterns in the CNS. *J. Neurosci.* *9*, 1712–1730.
- Selye, H. (1936). A syndrome produced by diverse nocuous agents. *J. Neuropsychiatry Clin. Neurosci.* *10*, 230–231.
- Selye, H. (1950). Stress and the general adaptation syndrome. *Br. Med. J.* *1*, 1383–1392.
- Shao, L., and Vawter, M.P. (2008). Shared gene expression alterations in schizophrenia and bipolar disorder. *Biol. Psychiatry* *64*, 89–97.
- Shiota, J., Ishikawa, M., Sakagami, H., Tsuda, M., Baraban, J.M., and Tabuchi, A. (2006). Developmental expression of the SRF co-activator MAL in brain: role in regulating dendritic morphology. *J. Neurochem.* *98*, 1778–1788.
- Shtrahman, M., Yeung, C., Nauen, D.W., Bi, G., and Wu, X. (2005). Probing Vesicle Dynamics in Single Hippocampal Synapses. *Biophys. J.* *89*, 3615–3627.
- Sies, H. (2014). Role of metabolic H₂O₂ generation: redox signaling and oxidative stress. *J. Biol. Chem.* *289*, 8735–8741.
- Sjöblom, B., Salmazo, A., and Djinović-Carugo, K. (2008). Alpha-actinin structure and regulation. *Cell. Mol. Life Sci. CMLS* *65*, 2688–2701.
- Soetanto, A., Wilson, R.S., Talbot, K., Un, A., Schneider, J.A., Sobiesk, M., Kelly, J., Leurgans, S., Bennett, D.A., and Arnold, S.E. (2010). Association of Anxiety and Depression With Microtubule-Associated Protein 2- and Synaptopodin-Immunolabeled Dendrite and Spine Densities in Hippocampal CA3 of Older Humans. *Arch. Gen. Psychiatry* *67*, 448–457.
- Spronsen, M. van, and Hoogenraad, C.C. (2010). Synapse Pathology in Psychiatric and Neurologic Disease. *Curr. Neurol. Neurosci. Rep.* *10*, 207–214.
- Stankiewicz, A.M., Goscik, J., Swiergiel, A.H., Majewska, A., Wieczorek, M., Juszcak, G.R., and Lisowski, P. (2014). Social stress increases expression of hemoglobin genes in mouse prefrontal cortex. *BMC Neurosci.* *15*, 130.
- Star, E.N., Kwiatkowski, D.J., and Murthy, V.N. (2002). Rapid turnover of actin in dendritic spines and its regulation by activity. *Nat. Neurosci.* *5*, 239–246.
- Steckler, T., Holsboer, F., and Reul, J.M. (1999). Glucocorticoids and depression. *Baillières Best Pract. Res. Clin. Endocrinol. Metab.* *13*, 597–614.
- Stevenson, R.P., Veltman, D., and Machesky, L.M. (2012). Actin-bundling proteins in cancer progression at a glance. *J. Cell Sci.* *125*, 1073–1079.
- Stritt, C., and Knöll, B. (2010). Serum Response Factor Regulates Hippocampal Lamination and Dendrite Development and Is Connected with Reelin Signaling. *Mol. Cell. Biol.* *30*, 1828–1837.

- Su, A.I., Wiltshire, T., Batalov, S., Lapp, H., Ching, K.A., Block, D., Zhang, J., Soden, R., Hayakawa, M., Kreiman, G., et al. (2004). A gene atlas of the mouse and human protein-encoding transcriptomes. *Proc. Natl. Acad. Sci. U. S. A.* *101*, 6062–6067.
- Swaminathan, V., Mythreye, K., O'Brien, E.T., Berchuck, A., Blobe, G.C., and Superfine, R. (2011). Mechanical Stiffness Grades Metastatic Potential in Patient Tumor Cells and in Cancer Cell Lines. *Cancer Res.* *71*, 5075–5080.
- Taboada, P., Gutiérrez-Pichel, M., Barbosa, S., and Mosquera, V. (2004). Determination of the interactions between an antidepressant amphiphilic drug and human serum albumin. *Phys. Chem. Chem. Phys.* *6*, 5203–5212.
- Tang, J.X., and Janmey, P.A. (1996). The polyelectrolyte nature of F-actin and the mechanism of actin bundle formation. *J. Biol. Chem.* *271*, 8556–8563.
- Terry-Lorenzo, R.T., Roadcap, D.W., Otsuka, T., Blanpied, T.A., Zamorano, P.L., Garner, C.C., Shenolikar, S., and Ehlers, M.D. (2005). Neurabin/Protein Phosphatase-1 Complex Regulates Dendritic Spine Morphogenesis and Maturation. *Mol. Biol. Cell* *16*, 2349–2362.
- Ting, H.-J., Yeh, S., Nishimura, K., and Chang, C. (2002). Supervillin associates with androgen receptor and modulates its transcriptional activity. *Proc. Natl. Acad. Sci.* *99*, 661–666.
- Uhr, M., Grauer, M.T., Yassouridis, A., and Ebinger, M. (2007). Blood–brain barrier penetration and pharmacokinetics of amitriptyline and its metabolites in p-glycoprotein (abcb1ab) knock-out mice and controls. *J. Psychiatr. Res.* *41*, 179–188.
- Ulrich-Lai, Y.M., and Herman, J.P. (2009). Neural regulation of endocrine and autonomic stress responses. *Nat. Rev. Neurosci.* *10*, 397–409.
- Urbanik, E., and Ware, B.R. (1989). Actin filament capping and cleaving activity of cytochalasins B, D, E, and H. *Arch. Biochem. Biophys.* *269*, 181–187.
- Uzbekov, R., Kireyev, I., and Prigent, C. (2002). Centrosome separation: respective role of microtubules and actin filaments. *Biol. Cell Auspices Eur. Cell Biol. Organ.* *94*, 275–288.
- Vanaja, D.K., Ballman, K.V., Morlan, B.W., Cheville, J.C., Neumann, R.M., Lieber, M.M., Tindall, D.J., and Young, C.Y.F. (2006). PDLIM4 repression by hypermethylation as a potential biomarker for prostate cancer. *Clin. Cancer Res.* *12*, 1128–1136.
- Vartiainen, M.K., Guettler, S., Larijani, B., and Treisman, R. (2007). Nuclear Actin Regulates Dynamic Subcellular Localization and Activity of the SRF Cofactor MAL. *Science* *316*, 1749–1752.
- Vicario-Abejón, C., Owens, D., McKay, R., and Segal, M. (2002). Role of neurotrophins in central synapse formation and stabilization. *Nat. Rev. Neurosci.* *3*, 965–974.
- Vyas, A., Mitra, R., Shankaranarayana Rao, B.S., and Chattarji, S. (2002). Chronic stress induces contrasting patterns of dendritic remodeling in hippocampal and amygdaloid neurons. *J. Neurosci. Off. J. Soc. Neurosci.* *22*, 6810–6818.

- Wang, L., Darling, J., Zhang, J.S., Liu, W., Qian, J., Bostwick, D., Hartmann, L., Jenkins, R., Bardenhauer, W., Schutte, J., et al. (2000). Loss of expression of the DRR 1 gene at chromosomal segment 3p21.1 in renal cell carcinoma. *Genes. Chromosomes Cancer* *27*, 1–10.
- Weaver, I.C.G., Cervoni, N., Champagne, F.A., D'Alessio, A.C., Sharma, S., Seckl, J.R., Dymov, S., Szyf, M., and Meaney, M.J. (2004). Epigenetic programming by maternal behavior. *Nat. Neurosci.* *7*, 847–854.
- Wegner, A.M., Nebhan, C.A., Hu, L., Majumdar, D., Meier, K.M., Weaver, A.M., and Webb, D.J. (2008). N-WASP and the Arp2/3 Complex Are Critical Regulators of Actin in the Development of Dendritic Spines and Synapses. *J. Biol. Chem.* *283*, 15912–15920.
- Wong, K.L., Bruch, R.C., and Farbman, A.I. (1991). Amitriptyline-mediated inhibition of neurite outgrowth from chick embryonic cerebral explants involves a reduction in adenylate cyclase activity. *J. Neurochem.* *57*, 1223–1230.
- Wood, Z.A., Schröder, E., Robin Harris, J., and Poole, L.B. (2003). Structure, mechanism and regulation of peroxiredoxins. *Trends Biochem. Sci.* *28*, 32–40.
- Xiu, M.H., Hui, L., Dang, Y.F., De Hou, T., Zhang, C.X., Zheng, Y.L., Chen, D.C., Kosten, T.R., and Zhang, X.Y. (2009). Decreased serum BDNF levels in chronic institutionalized schizophrenia on long-term treatment with typical and atypical antipsychotics. *Prog. Neuropsychopharmacol. Biol. Psychiatry* *33*, 1508–1512.
- Yamato, T., Orikasa, K., Fukushige, S., Orikasa, S., and Horii, A. (1999). Isolation and characterization of the novel gene, TU3A, in a commonly deleted region on 3p14.3-->p14.2 in renal cell carcinoma. *Cytogenet. Cell Genet.* *87*, 291–295.
- Yan, Y., Sabharwal, P., Rao, M., and Sockanathan, S. (2009). The antioxidant enzyme Prdx1 controls neuronal differentiation by thiol-redox-dependent activation of GDE2. *Cell* *138*, 1209–1221.
- Yang, H.-J., Li, Y.-F., Zhang, H.-T., Zhang, F.-Q., Zhao, N., Gong, Z.-H., and Luo, Z.-P. (2003). Up-regulation of microtubule-associated protein 4 and drebrin A mRNA expression by antidepressants in rat hippocampus following chronic stress. *Neurosci. Lett.* *351*, 206–208.
- Yauch, R.L., Felsenfeld, D.P., Kraeft, S.-K., Chen, L.B., Sheetz, M.P., and Hemler, M.E. (1997). Mutational Evidence for Control of Cell Adhesion Through Integrin Diffusion/Clustering, Independent of Ligand Binding. *J. Exp. Med.* *186*, 1347–1355.
- Yehuda, R. (2002). Post-traumatic stress disorder. *N. Engl. J. Med.* *346*, 108–114.
- Yoo, Y., Wu, X., and Guan, J.-L. (2007). A Novel Role of the Actin-nucleating Arp2/3 Complex in the Regulation of RNA Polymerase II-dependent Transcription. *J. Biol. Chem.* *282*, 7616–7623.
- Yuste, R., and Bonhoeffer, T. (2001). Morphological changes in dendritic spines associated with long-term synaptic plasticity. *Annu. Rev. Neurosci.* *24*, 1071–1089.

Zhao, X.-Y., Liang, S.-F., Yao, S.-H., Ma, F.-X., Hu, Z.-G., Yan, F., Yuan, Z., Ruan, X.-Z., Yang, H.-S., Zhou, Q., et al. (2007). Identification and preliminary function study of *Xenopus laevis* DRR1 gene. *Biochem. Biophys. Res. Commun.* *361*, 74–78.

Zhou, N.E., Kay, C.M., and Hodges, R.S. (1994). The net energetic contribution of interhelical electrostatic attractions to coiled-coil stability. *Protein Eng.* *7*, 1365–1372.

Zigmond, S.H. (1993). Recent quantitative studies of actin filament turnover during cell locomotion. *Cell Motil. Cytoskeleton* *25*, 309–316.

Appendix

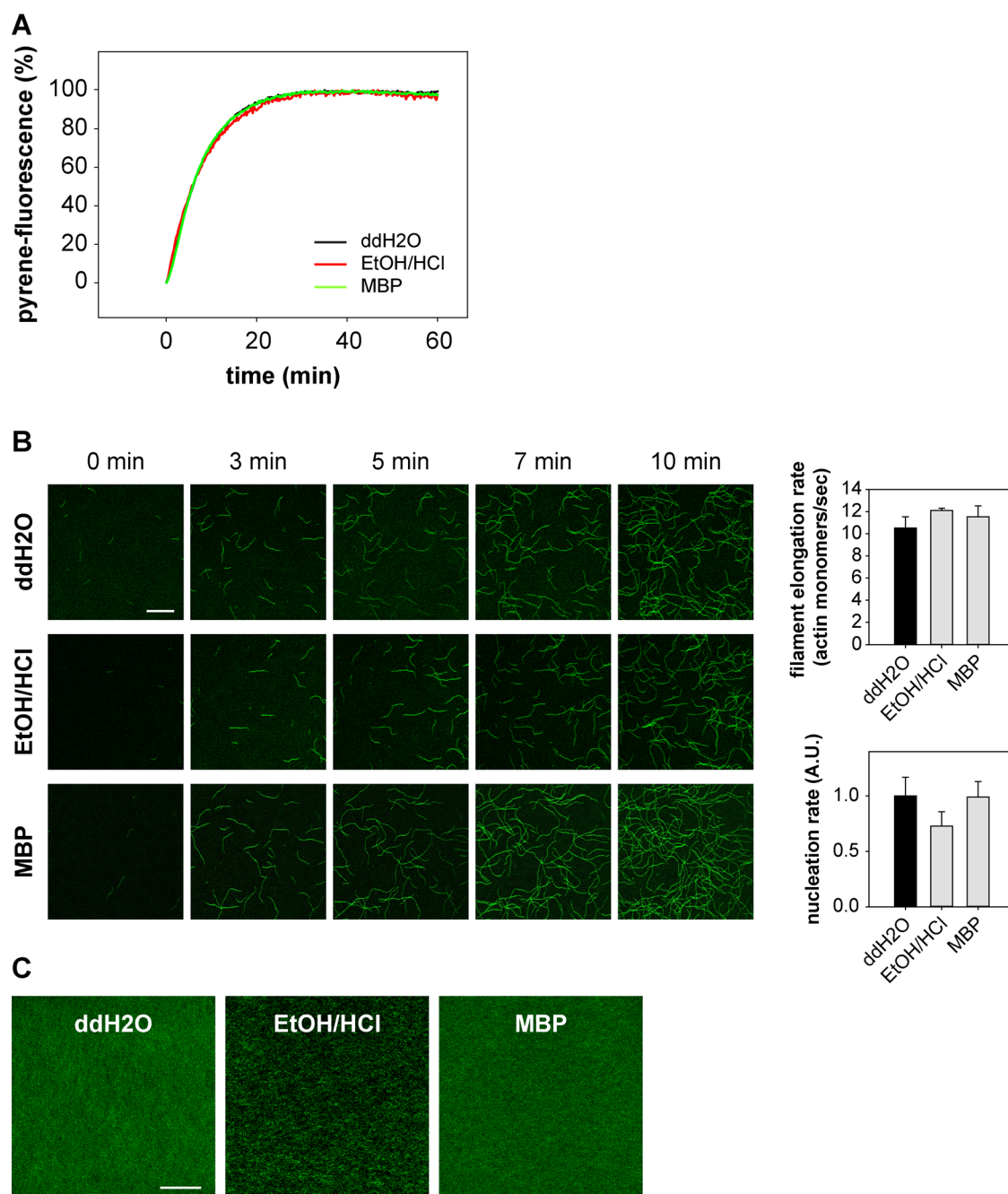
Supplementary Movies

The time-lapse images acquired from confocal polymerization of phalloidin-labeled actin shown in Figure 7, Figure 15, and Figure 19 are provided on the enclosed CD as “.avi” movie files.

FILENAME	SAMPLE	R
01 control ddH2O.avi	ddH2O	-
02 control EtOH-HCl.avi	50% EtOH/5 mM HCl	-
03 control MBP R05.avi	MBP	0.5
04 clomi R5.avi	Clomipramine	5
05 clomi R50.avi	Clomipramine	50
06 DRR1 wt R01.avi	DRR1 wt	0.1
07 DRR1 wt R025.avi	DRR1 wt	0.25
08 DRR1 wt R05.avi	DRR1 wt	0.5
09 DRR1 dN R05.avi	DRR1 dN	0.5
10 DRR1 dC R05.avi	DRR1 dC	0.5
11 DRR1 dM R05.avi	DRR1 dM	0.5
12 DRR1 M R05.avi	DRR1 M	0.5
13 DRR1 N R05.avi	DRR1 N	0.5
14 DRR1 dPEPE R05.avi	DRR1 dPEPE	0.5
15 DRR1 dC94A R05.avi	DRR1 C94A	0.5

Table 19. List of supplementary movies (on CD).

Supplementary Figure



Supplementary Figure 1. Overview of the controls used in all *in vitro* actin assays: ddH₂O, the solvent of the antidepressants 50% EtOH/5 mM HCl, and purified MBP protein. The controls ddH₂O and EtOH/HCl were added in a constant volume, MBP was added in R = 0.5. (A) Pyrene-polymerization assay. Actin filaments (5 μM, 20% pyrene-labeled) were polymerized and increase in fluorescence of pyrene-actin during polymerization was monitored for 60 min. Representative curves are shown. (B) Confocal time-lapse images of *in vitro* actin polymerization (1 μM actin). Filaments were visualized by phalloidin. Scale bar denotes 10 μm. Quantification of filament elongation and nucleation rate. Bars represent means + SEM. No significant differences were found. Statistical analysis was performed with one-way ANOVA and Bonferroni *post hoc*. (C) Actin networks (4 μM) were polymerized at RT for > 2 h and visualized with phalloidin-488. Images were taken in a confocal microscope (63x/1.4 NA objective, 10 μm z-stacks). Scale bar denotes 50 μm.

Abbreviations

ABPs	Actin binding proteins
ADF/cofilin	Actin depolymerizing factor/cofilin
Amp	Ampicillin
AMPA receptor	α -amino-3-hydroxy-5-methyl-4-isoxazolepropionic acid r.
ANOVA	Analysis of variance
APS	Ammonium persulfate
ATP	Adenosine triphosphate
BCA	Bicinchoninic acid
BMB	1,4-Bismaleimidobutane
BSA	Bovine serum albumin
Cdc42	Cell division control protein 42
Cital	Citalopram
Clomi	Clomipramine
CoIP	Coimmunoprecipitation
DAD	Diaphanous autoregulatory domain
DAPI	4',6-diamidino-2-phenylindole
DID	Diaphanous inhibitory domain
ddH ₂ O	Double distilled water
DMEM	Dulbecco's modified eagle medium
DMSO	Dimethyl sulfoxide
DNA	Deoxyribonucleic acid
Dox	Doxepin
dNTPs	Deoxyribonucleotide triphosphates
DRR1	Down-regulated in renal cell carcinoma 1
DSG	Disuccinimidyl glutarate
DSS	Disuccinimidyl suberate
DTT	Dithiothreitol
<i>E. coli</i>	<i>Escherichia coli</i>
EDTA	Ethylenediamine tetraacetic acid
EGTA	Ethyleneglycol tetraacetic acid
Eps8	Epidermal growth factor receptor pathway substrate 8
EtOH	Ethanol
F	Flag-tag
F-actin	Filamentous actin
FAM107A	family with sequence similarity 107, member A
FBS / FCS	Fetal bovine/calf serum
G-actin	Globular actin
GR	Glucocorticoid receptor
GS	Goat serum
h	hours
HBSS	Hank's balanced salt solution
HEK-293 cells	Human embryonic kidney-293 cells
HeLa cells	Henrietta Lacks cells
HPA axis	Hypothalamic-pituitary-adrenal axis
HPC	Hippocampus
HRP	Horseradish peroxidase

IB	Immunoblot
IPTG	Isopropyl β -D-1-thiogalactopyranoside
Kan	Kanamycin
LTP / LTD	Long term potentiation / depression
MBP	Maltose binding protein
min	minute
MR	Mineralocorticoid receptor
mRNA	Messenger RNA
MWCO	Molecular weight cut off
NBA	Neurobasal A
NEM-HMM	N-ethylmaleimide-modified heavy meromyosin
NLS	Nuclear localization signal
NMDA receptor	N-Methyl-D-aspartic acid receptor
(N-)WASP	(neuronal) Wiskott-Aldrich syndrome protein
OD	Optical density
PAA	Polyacrylamide
PAGE	Polyacrylamide gel electrophoresis
PBS	Phosphate buffered saline
PCC	Pearson's correlation coefficient
PCR	Polymerase chain reaction
PI	Protease inhibitor
PFA	Paraformaldehyde
PMSF	Phenylmethanesulfonyl fluoride
Rac1	Ras-related C3 botulinum toxin substrate 1
RhoA	Ras homolog gene family, member A
R	Ratio of antidepressant of DRR1 protein : actin
RNA	Ribonucleic acid
ROCK	Rho-associated protein kinase
ROI	Region of interest
rpm	Rounds per minute
RT	RT
s	Second
SEM	Standard error of the mean
SDS	Sodium dodecyl sulfate
SSRI	Selective serotonin reuptake inhibitor
TBS-T	Tris-buffered saline tween 20
TEMED	Tetramethylethylenediamine
TRIS	Tris-(hydroxymethyl)-aminomethan
TU3A	Tohoku University cDNA clone A on chromosome 3
wt	wild type

List of Figures

Figure 1.	Overview of actin dynamics and actin binding proteins.	6
Figure 2.	The pathway of the serum response factor (SRF).	10
Figure 3.	Chemical structures of antidepressants used in this study.	55
Figure 4.	Clomipramine inhibits <i>in vitro</i> polymerization of pyrene-labeled actin, while doxepin and citalopram have no effect.	56
Figure 5.	Clomipramine inhibits <i>in vitro</i> polymerization of pyrene-labeled β -actin to a similar extent as α -actin.	57
Figure 6.	Inhibition of polymerization by clomipramine was confirmed with rheology using label-free actin.	58
Figure 7.	Clomipramine has no effect on single filament elongation while it slightly reduces nucleation. .	60
Figure 8.	Antidepressants have no effect on actin network structure.	61
Figure 9.	The overall structure of actin filaments in astrocytes is largely unaffected by antidepressants. .	63
Figure 10.	Clomipramine does not affect migration of HeLa cells in a 2D migration assay.	64
Figure 11.	Clomipramine reduces spreading of HeLa cells at high concentrations.	65
Figure 12.	DRR1 binds actin in HEK-293 and F-actin <i>in vitro</i> in a concentration-dependent manner.	68
Figure 13.	DRR1 inhibits <i>in vitro</i> polymerization of pyrene-labeled actin.	69
Figure 14.	DRR1 strongly bundles actin filaments in a polymerized network.	70
Figure 15.	DRR1 strongly reduces single filament elongation and increases nucleation rate.	72
Figure 16.	Domain structure and mutants of DRR1.	74
Figure 17.	DRR1 shows two actin binding regions separated by a central non-binding region.	75
Figure 18.	Both actin binding regions bind F-actin <i>in vitro</i>	76
Figure 19.	<i>In vitro</i> polymerization of pyrene-labeled actin is inhibited by DRR1 wt, dM and C94A.	77
Figure 20.	Single filament polymerization is inhibited by DRR1 wt, dM and C94A, while nucleation is enhanced by DRR1 wt, dM, dPEPE and C94A.	79
Figure 21.	All DRR1 mutants show deficits in actin bundling.	80
Figure 22.	DRR1 is crosslinked by the chemical crosslinkers DSS and BMB in HEK-293 cells.	82
Figure 23.	The middle domain interferes with actin bundling of full length DRR1 (wt).	83
Figure 24.	DRR1 wt and all mutants localize to the nucleus in HEK-293 cells.	84
Figure 25.	DRR1 wt and dN localize along actin stress fibers in HeLa cells.	87
Figure 26.	Mean F-actin per cell is increased with DRR1 wt, dN, dM and C94A overexpression.	89
Figure 27.	DRR1-dependent increase in cellular F-actin leads to a strong activation of the serum response factor (SRF).	90
Figure 28.	DRR1 colocalization with F-actin is increased in HeLa cells treated with Cytochalasin D.	92
Figure 29.	DRR1 stabilizes F-actin in HeLa cells treated with Cytochalasin D.	93
Figure 30.	DRR1 wt and all mutants except M reduce spreading of HeLa cells on fibronectin.	95
Figure 31.	DRR1 wt and the mutant dN slow down actin treadmilling in HeLa cells.	96
Figure 32.	DRR1 localizes to dendrites and dendritic spine heads.	97
Figure 33.	Model of DRR1's effects on actin dynamics.	102
Figure 34.	Hypothetical effect of DRR1 on dendritic spine maturation.	107
Supplementary Figure 1.	Overview of the controls used in all <i>in vitro</i> actin assays: ddH ₂ O, the solvent of the antidepressants 50% EtOH/5 mM HCl, and purified MBP protein.	127

List of Tables

Table 1.	List of consumable supplies.	18
Table 2.	List of chemicals.	20
Table 3.	List of solutions and media.	21
Table 4.	List of kits and ready-to-use materials.	22
Table 5.	List of primary antibodies.	23
Table 6.	List of secondary antibodies.	23
Table 7.	List of bacterial clades.	23
Table 8.	List of cell lines.	23
Table 9.	List of oligonucleotides.	25
Table 10.	List of plasmids.	27
Table 11.	List of instruments.	28
Table 12.	List of software.	29
Table 13.	Cloned mutants and respective primers used.	33
Table 14.	Standard program for PCR.	33
Table 15.	PCR program for site-directed mutagenesis.	34
Table 16.	Colocalization parameters of DRR1 and actin.	85
Table 17.	Schematic overview of DRR1's molecular effects on actin dynamics.	100
Table 18.	Schematic overview of DRR1 effects on actin-dependent cellular processes.	104
Table 19.	List of supplementary movies (on CD).	126

Biographical Sketch

Personal Information

Name: Anja Kretzschmar
Date of Birth: 04.03.1986
Place of Birth: Heidenheim an der Brenz, Germany

Education

03/2012 – present PhD student at the Max Planck Institute of Psychiatry, Munich, project group Dr. Theo Rein, Department of Translational Research in Psychiatry
10/2008 – 12/2010 Molecular Biotechnology, M. Sc., Technische Universität München, Master's thesis at the Max Planck Institute of Psychiatry, „Domain Mapping of the Novel Stress-Inducible Protein DRR1”
08/2009 – 02/2010 Study Abroad, McGill University, Montréal, Canada, final grade 3.67
10/2005 – 07/2008 Biochemistry, B. Sc., Technische Universität München, Bachelor's thesis at the Chair of Biotechnology “Analysis of Hsp90 cochaperones from *C. elegans* *in vivo* and *in vitro*”
06/2005 Abitur (diploma from German secondary school)

Awards

10/2014 Congress scholarship of the German Academic Exchange Service (DAAD) to visit the EMBO Workshop “Systems-Level View of Cytoskeletal Function”.
02/2014 Poster award at the <interact>, a conference for young life scientists in Munich.
07/2013 Poster award at the summer symposium of the Max Planck Institute of Psychiatry.

Publications

Kretzschmar, A., Schülke, J.-P., Masana, M., Müller, M.B., Bausch, A.R., Rein, T. The novel stress-inducible protein DRR1 exerts manifold effects on actin dynamics. (in preparation)

Masana, M., Dine, J., Filsen, S., Blazquez-Llorca, L., **Kretzschmar, A.**, Schmidt, M.V., Bock, J., Herms, J., Eder, M., Rein, T., Müller, M.B. Cognitive performance and synaptic function are dependent on the resilience-promoting protein DRR1. (in preparation)

Masana, M., Westerholz, S., **Kretzschmar, A.**, Treccani, G., Liebl, C., Santarelli, S., Dournes, C., Popoli, M., Schmidt, M.V., Müller, M.B. Neuroanatomical and cellular expression patterns of DRR1 in the adult mouse brain. (in preparation)

Gassen, N.C., Hartmann, J., Zannas, A.S., **Kretzschmar, A.**, Zschocke, J., Maccarrone, G., Hafner, K., Zellner, A., Kollmannsberger, L.K., Wagner, K.V., Mehta, D., Kloiber, S., Turck, C.W., Lucae, S., Chrousos, G.P., Holsboer, F., Binder, E.B., Ising, M., Schmidt, M.V., Rein, T. FKBP51 inhibits GSK3 β and augments the effects of distinct psychotropic medications. *Mol Psychiatry*. Accepted 2015 Feb.

Masana, M., Jukic, M.M., **Kretzschmar, A.**, Wagner, K.V., Westerholz, S., Schmidt, M.V., Rein, T., Brodski, C., Müller, M.B. Deciphering the spatio-temporal expression and stress regulation of Fam107B, the paralog of the resilience-promoting protein DRR1 in the mouse brain. *Neuroscience*. 2015 Jan 28. pii: S0306-4522(15)00081-0.

Knapp, R.T., Wong, M.J., Kollmannsberger, L.K., Gassen, N.C., **Kretzschmar, A.**, Zschocke, J., Hafner, K., Young, J.C., Rein, T. Hsp70 Cochaperones HspBP1 and BAG-1M Differentially Regulate Steroid Hormone Receptor Function. *PLoS One*. 2014 Jan 14;9(1):e85415.

Gaiser, A.M., **Kretzschmar, A.**, Richter, K. Cdc37-Hsp90 Complexes Are Responsive to Nucleotide-induced Conformational Changes and Binding of Further Cofactors. *J Biol Chem*. 2010 Dec 24;285(52):40921-32.

Acknowledgements

An dieser Stelle würde ich mich gerne zuerst bei Theo bedanken, der während der gesamten Zeit immer ein offenes Ohr hatte. Vielen Dank Theo für deine ausgezeichnete Betreuung und deine Unterstützung, besonders in der Endphase der Doktorarbeit und während der vielen experimentellen/vertraglichen Verunsicherungen, die immer wieder auftraten. Desweiteren möchte ich mich bei Prof. Florian Holsboer und Dr. Elisabeth Binder für die Möglichkeit bedanken, meine Doktorarbeit am MPI für Psychiatrie durchzuführen.

Auch Prof. Haralabos Zorbas möchte ich herzlich danken für die Fachvertretung meiner Doktorarbeit and der Fakultät für Chemie und Pharmazie der LMU, sowie den weiteren Mitgliedern meiner Prüfungskommission Prof. Florian Holsboer, PD Dr. Theo Rein, Prof. Chris Turck, Prof. Stefan Zahler und Prof. Klaus Förstemann. Und Dr. Matthias Eder für die Teilnahme an meinem Thesis Advisory Committee.

Der gesamten Arbeitsgruppe Rein möchte ich sehr herzlich danken, für die angenehme Arbeitsatmosphäre und die vielen netten Gespräche: Kathi, Kirmi, Lorenz, Marie, Nils und Svenja, und natürlich auch allen Ehemaligen Anna, Barbara, Jürgen, Nicki, Regina, Tatjana und Vanessa. Vor allem möchte ich mich dabei bei Jan bedanken, für die gute Betreuung zu Beginn des Projekts und darüber hinaus bei der (noch andauernden) Publikationsvorbereitung. Moltes gràcies també a Mercè por motivarme tanto y orientarme en muchas ocasiones. Y muchas gracias a Sebastián por la grán ayuda con las neuronas.

Ganz besonderer Dank geht an Prof. Andreas Bausch, für die Möglichkeit die vielen Experimente an seinem Lehrstuhl zu machen. Allen, die mir dort geholfen haben, möchte ich danken, insbesondere Carina Pelzl, Christine Wurm, Katharina Henneberg, Kurt Schmoller und Simone Köhler.

Y bueno, al final los más importantes... Gracias Mamá, Papa, Sorellina y tío Victor por apoyarme siempre en todo. Gracias abuelo por ser un ejemplo a seguir para todos nosotros. Y Christopher, gracias por estar siempre junto a mí con amor, paciencia y besitos :)